UCLA
UCLA Electronic Theses and Dissertations

Title
Biological Considerations in Beam Selection for Particle Therapy Optimization

Permalink
https://escholarship.org/uc/item/02n1x0dt

Author
Ramesh, Pavitra

Publication Date
2024

Peer reviewed|Thesis/dissertation

eScholarship.org Powered by the California Digital Library
University of California

UNIVERSITY OF CALIFORNIA

Los Angeles

Biological Considerations in Beam Selection for Particle Therapy Optimization

A dissertation submitted in partial satisfaction of the

requirements for the degree Doctor of Philosophy

in Physics and Biology in Medicine

by

Pavitra Ramesh

2024

© Copyright by

Pavitra Ramesh

2024

ABSTRACT OF THE DISSERTATION

Biological Considerations in Beam Selection for Particle Therapy Optimization

by

Pavitra Ramesh

Doctor of Philosophy in Physics and Biology in Medicine

University of California, Los Angeles, 2024

Professor Ke Sheng, Co-Chair

Professor Dan Ruan, Co-Chair

Purpose

Beam orientation and biological dose optimization are interdependent features of Intensity-Modulated Proton Therapy (IMPT). Current automated beam orientation optimization (BOO) methods are robust and able to provide beam convergence but have not accounted for accurate biological modeling that narrows the therapeutic window. Biological models such as relative biological effectiveness (RBE) and oxygen enhancement ratio (OER) and machine parameters such as dose-averaged dose rate (DADR) are highly

complex and lead to computationally challenging frameworks that may be solved by novel optimization methods.

Methods

The robust BOO framework for IMPT was formulated with physical dose fidelity to provide accurate dose to the tumor and limit dose to organs at risk (OARs), a heterogeneity-weighted L2,1/2-norm group sparsity term to reduce the number of active beams to 2-4, and a sensitivity regularization term. The dose fidelity term was updated to consider variable RBE values, lower oxygenation status in tumor regions, and the normal tissue sparing effects caused by high dose rate. These biologically-informed BOO frameworks were solved with RBE and dose rate linearization along with splitting schemes. The plans were generally tested on challenging head-and-neck (H&N) cases and compared against previous plans in terms of dosimetry and robustness.

Results

Compared to IMPT BOO plans solved with constant RBE=1.1, McNamara RBE-based dose was able to improve OAR [Dmean, Dmax, worst Dmean, worst Dmax] by an average of [36.1%, 26.4%, 25.0%, 19.2%] with modest CTV coverage and robustness improvement. Additionally, hypoxia-based RBE dose fidelity was able to increase tumor [HI, Dmax, worst HI, worst Dmax] by [31.3%, 48.6%, 12.5%, 7.3%] with only [8.0%, 13.1%] increase in OAR [Dmean, Dmax], increasing the therapeutic index. Next, compared to spread-out Bragg peak IMPT BOO plans, dose rate-optimized plans with Bragg peak and shoot-through beams combined were able to increase volume of ROIs receiving >40 Gy/s by approximately 41.1%, while improving CTV homogeneity by 5.6% and improving OAR dose in several structures.

Conclusions

Novel optimization methods were developed for biologically-guided IMPT. The objective function integrates RBE-weighted dose, hypoxia-informed dose, and dose rate optimization into a unified framework with BOO as the baseline objective. Compared with the physical dose BOO or manual selection, our method generates plans with superior tumor and normal tissue dosimetry and robustness.

The dissertation of Pavitra Ramesh is approved.

Michael McNitt-Gray

Minsong Cao

Lei Dong

Ke Sheng, Committee Co-Chair

Dan Ruan, Committee Co-Chair

University of California, Los Angeles

2024

Dedicated to my father.

Thank you for showing me the importance of hard work.

TABLE OF CONTENTS

LIST OF TABLES

LIST OF FIGURES

LIST OF EQUATIONS

List of Abbreviations

IMRT	Intensity-modulated radiation therapy
IMPT	Intensity-modulated proton therapy
IMCT	Intensity-modulated carbon-ion therapy
RBE	Relative biological effectiveness
LET(d)	Linear energy transfer (dose-averaged)
ICRU	International Commission on Radiation Units and Measurements
OER	Oxygen enhancement ratio
VMAT	Volumetric-modulated arc therapy
SHBOO	Sensitivity-regularized and homogeneity-weighted beam orientation optimization
FMO	Fluence map optimization
CTV	Clinical target volume
OAR	Organ at risk
FISTA	Fast iterative shrinkage thresholding algorithm
CP	Chambolle-Pock algorithm
HI	Homogeneity index
Phys-FISTA	Physical dose optimization with FISTA as the solver
McNam-FISTA	McNamara RBE dose optimization with FISTA as the solver
McNam-CP	McNamara RBE dose optimization with CP as the solver
LET-FISTA	LET-based optimization with FISTA as the solver
SB	Split Bregman optimization
Phys-SB	Physical dose optimization using the SB method
McNam-SB	McNamara RBE dose optimization using the SB method
FMISO	[^{18}F]-fluoromisonidazole positron emission tomography
pO_2	Partial oxygen pressure
TI	Therapeutic index
gEUD	Generalized uniform equivalent dose

cRBE	Constant/ physical dose optimization
RegRBE	Regular / normoxic McNamara RBE optimization
HypRBE	Hypoxia-informed McNamara RBE optimization
SDDRO	Simultaneous dose and dose rate optimization
BP	Bragg peak
ST	Shoot-through
DADR	Dose-averaged dose rate
BP-DR	Bragg peak beam with dose rate optimization
ST-DR	Shoot through beam with dose rate optimization
BPST-DR	Bragg peak and shoot through beam with dose rate optimization
SSBOO	Spatially separated beam orientation optimization
GCR	Optimization with gantry and couch rotation
FB	Optimization with fixed beamline
FBCR	Optimization with fixed beamline and couch rotation

ACKNOWLEDGEMENTS

My advisor, Dr. Ke Sheng, is truly the #KeToSuccess. When I first came to UCLA, I knew almost immediately that I would get the most out of my graduate study with him as my mentor. His constant guidance and encouragement have motivated me to go above and beyond the basic requirements for a degree in medical physics. Because of his wisdom and creativity, I've learned to enjoy research and seize all opportunities for growth. I don't believe I will ever find another mentor as kind and knowledgeable as him. Thank you for everything, Ke.

I would also like to thank Dr. Dan Ruan, who has added immense value to my research and my graduate journey. She is kind, patient, and incredibly knowledgeable. I would also like to thank Dr. Lei Dong and Dr. Minsong Cao for expanding my horizons to beyond our research lab.

Many thanks to previous Sheng Lab members including Drs. Daniel O'Connor, Wenbo Gu, Ryan Neph, Qihui Lyu, and Elizabeth McKenzie. You've all set the bar so high, but the foundation you've provided has undoubtedly played a role in the completion of my dissertation. Thanks to my current lab mates Jiayi, Hengjie, Holly, Alan, Qifan, Flute, Lu, and the rest of PBM for all the wonderful times. You all make me believe that the future of medical physics is in excellent hands. Special thanks to Louise and Dishane for your everlasting support. You are both considered family to me.

Thank you to Dr. Michael McNitt-Gray, for creating a graduate program atmosphere unlike any other. I hope to become half the leader you are today. Thank you to Reth and Alondra for making me feel well-supported.

I'd like to thank my parents for the unconditional love and support you've given me throughout my life, regardless of your level of understanding of medical physics—thank you for trusting me. Thank you to my Akka for showing me how to fearlessly chase my dreams. Thank you to my amazing husband Sathya for showing me what real happiness looks like (beyond the following pages, of course). I can't wait to start this new chapter with you by my side.

VITA

EDUCATION

M.S.	University of California—Los Angeles, Physics and Biology in Medicine	2021
B.S.	Carnegie Mellon University, Biological Physics	2019

AWARDS

UCLA Moses A. Greenfield Award	2023
UCLA Dissertation Year Fellowship	2023
AAPM Southern California Chapter Norm Baily Graduate Student First Place Award	2023
AAPM Best in Physics (Therapy) Award	2022
AAPM Southern California Chapter Norm Baily Graduate Student First Place Award	2022
AAPM Southern California Chapter Med Phys SLAM Competition Winner	2022

PEER-REVIEWED PUBLICATIONS

1. **Ramesh P**, Ruan D, et al. Hypoxia informed RBE-weighted beam orientation optimization for intensity modulated proton therapy. *Medical Physics*. 2024. doi: 10.1002/mp.16978
2. **Ramesh P**, Valdes G, O'Connor D, Sheng K. Beam orientation optimization for IMRT and IMPT using path seeking algorithms. *Physics in Medicine and Biology*. 2023. doi:10.1088/1361-6560/acf63f
3. Frank CH, **Ramesh P**, et al. Analytical HDR prostate brachytherapy planning with automatic catheter and isotope selection. *Medical Physics*. 2023. doi:10.1002/mp.16677
4. Jiang L, **Ramesh P**, Neph R, Sheng K. Technical Note: Multi-MATE, a high-throughput platform for automated image-guided small animal-irradiation. *Medical Physics*. 2023. doi:10.1002/mp.16563
5. **Ramesh P**, Gu W, Ruan D, Sheng K. Dose and dose rate objectives in Bragg peak and shoot-through beam orientation optimization for FLASH proton therapy. *Medical Physics*. 2022. doi:10.1002/mp.16009
6. **Ramesh P**, Lyu Q, Gu W, Ruan D, Sheng K. Reformulated McNamara RBE-weighted beam orientation optimization for intensity modulated proton therapy. *Medical Physics*. 2022. doi: 10.1002/mp.15552.
7. **Ramesh P**, Liu H, Gu W, Sheng K. Fixed beamline optimization for intensity modulated carbon-ion therapy. *IEEE Transactions on Radiation and Plasma Medical Sciences*. 2021. doi: 10.1109/TRPMS.2021.3092296.
8. **Ramesh P**, Zhang Y, Yue N, et al. Automatic measurement of air gap for proton therapy using orthogonal x-ray imaging with radiopaque wires. *Journal of Applied Clinical Medical Physics*. 2018. doi: 10.1002/acm2.12509

SELECTED CONFERENCE PRESENTATIONS

1. **Ramesh P**, Ruan D, et al. "Hypoxia informed RBE-weighted beam orientation optimization for intensity modulated proton therapy using [18F]-FMISO estimation of pO2" (2023) Presented as

a poster at the American Association of Physicists in Medicine (AAPM) 65th Annual Meeting, Houston, TX and at the American Society for Radiation Oncology (ASTRO) 65th Annual Meeting, San Diego, CA.

2. **Ramesh P**, Ruan D, Sheng K. "A split-Bregman approach can solve beam orientation optimization with nonlinear RBE dose fidelity" (2023) Presented as a poster at the 61st Conference of the Particle Therapy Co-Operative Group (PTCOG), Madrid, Spain and at the AAPM 65th Annual Meeting, Houston, TX.
3. **Ramesh P**, Gu W, Ruan D, et al. "Dose and dose rate optimization for FLASH proton therapy with automated Bragg peak and shoot-through beam selection" (2022) Presented orally at the AAPM 64th Annual Meeting, Washington D.C. and at the PTCOG 60th Annual Conference, Miami, FL.
4. **Ramesh P**, Lyu Q, Gu W, et al. "Robust alternating RBE- and LET-weighted beam orientation and fluence map optimization for intensity-modulated proton therapy" (2021) Presented orally at the PTCOG 59th Annual Conference, Online.
5. **Ramesh P**, Shen ZL, Huq S, et al. "HyperArc SRS planning reduces the dose to brain, optic nerves, and chiasm for patients with intracranial meningioma" (2018) Presented orally at the Penn Ohio AAPM Fall Symposium, Pittsburgh, PA.

1 INTRODUCTION

1.1 Intensity-Modulated Proton Therapy

Radiation therapy or radiotherapy is a common cancer treatment that uses high-energy ionizing radiation to target cancer cells. Although x-ray photon radiotherapy is widely employed, its high exit dose and mediocre tumor conformality limits its ability to reduce toxicity to normal tissue[1]. Particle radiotherapy, specifically proton radiotherapy, has been proposed for oncology clinics since 1946 due to its ability to deposit dose in the shape of Bragg peaks, characterized by a low entrance dose through the patient's body, a high amount of dose that "peaks" at the end of its range at a certain depth depending on beam energy, and a steep drop-off resulting in virtually no exit dose[2]. The characteristic Bragg peak is desirable in cases where critical normal tissue is located behind a tumor. In contrast, x-ray photons are characterized by their shallow peak and gradual drop-off, shown in Figure 1-1.

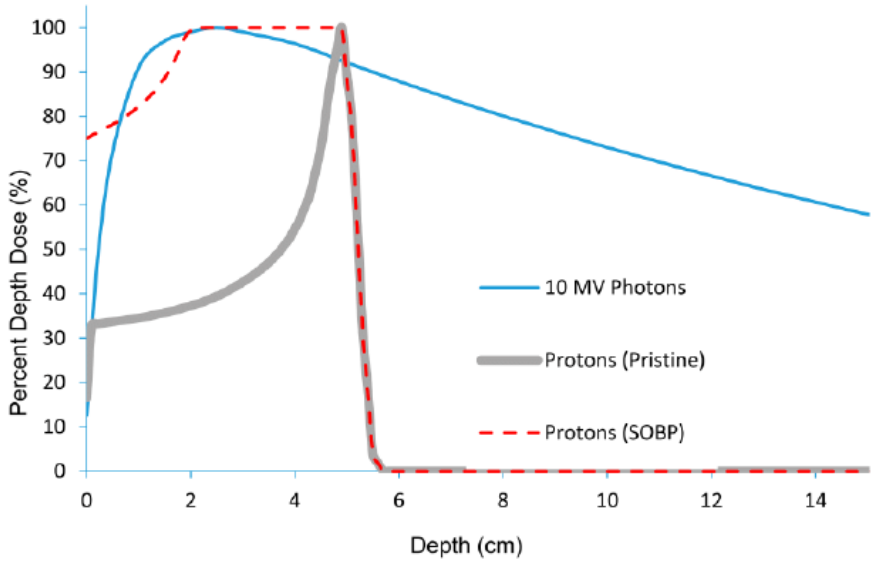

Figure 1-1. Percent depth-dose curve of photon beam, monoenergetic (pristine) proton beam, and spread-out Bragg peak (SOBP). Reprinted from "Proton Beam Therapy for Non-Small Cell Lung Cancer: Current Clinical Evidence and Future Directions" by AT Berman and SS James, Cancers (Basel), 2015,7:1178-1190. [3]

For a proton to reach the distal edge of a tumor, it must be accelerated using a cyclotron or synchrotron, and its energy may be changed using an energy selection system. Weighted pristine Bragg peaks may be superimposed to form a spread-out Bragg peak (SOBP), shown in Figure 1-1, that covers the full depth of the tumor. Additionally, there is a trend towards using dynamic pencil beam scanning rather than passive scattering. While passive scattering spreads a narrow pencil beam using foils, pencil beam scanning modulates the pencil beams or "spots" across the tumor region using magnets[4]. Similar to beamlets in Intensity-Modulated Radiation Therapy (IMRT), the spots can be weighted and positioned to any point within the 3D volume, creating a highly conformal dose distribution. This technique is called Intensity-Modulated Proton Therapy (IMPT)[5].

1.2 Radiobiological Effectiveness of Particle Therapy

Beyond physical characteristics like the shape of the dose deposition, proton radiotherapy is further distinguished from photon radiotherapy because of charged particle radiobiological effects[6,7]. Since protons slow down with penetration, they increase their ionization density (the number of ions per unit path length)[8] and subsequently increase their direct contribution to DNA damage and cell death[9]. The term relative biological effectiveness (RBE) can be used to quantify the effectiveness of proton physical dose in relation to the effectiveness of photon dose. RBE is defined as the ratio of dose required to produce a biological effect (with endpoint X) using reference photon irradiation versus proton. Since the dose required to produce endpoint X would be higher for photon irradiation than for proton, the RBE would be a value greater than 1.

$$RBE(\mathrm{X}) = \frac{Dose_{reference}(\mathrm{X})}{Dose_{proton}(\mathrm{X})}$$

Equation 1-1

The dose for proton therapy is prescribed as the product of RBE and physical dose, GyRBE, according to the International Commission on Radiation Units and Measurements (ICRU)[8]. In current clinical practice, RBE is generally accepted to be a constant value of 1.1 based on *in vitro* mice studies from the late 1970's using passive scattering[10]. However, more recent studies have shown that RBE can vary voxel-to-voxel based on several factors including physical dose per fraction, tissue type characterized by survival fraction parameters α and β, linear energy transfer (LET), biological endpoint, and beam characteristics[11]. Although the American Association of Physicists in Medicine (AAPM) task

group reports recommend a constant RBE, they also note potential exceptions for distal critical structures with low alpha-beta ratios and their subsequent RBE values of up to 1.2 or 1.3[11]. Using an under- or overestimation of RBE for tumors or organs at risk during treatment planning could undermine the efficacy of proton therapy[12], causing insufficient tumor control[13] or higher probability of normal tissue complication due to increased toxicity to tumor-adjacent critical structures.

1.3 Oxygen Enhancement and Dose Rate Impact on Radiobiological Effectiveness

Protons have a higher LET than photons, but in comparison to carbon ions, helium ions, and other heavy ions, protons are considered low LET particles[14-16]. Protons have an LET range in the beam axis between 1.1-5.1 keV/μm at depths of water from 30-151 mm, respectively[17]. In reality, there is a spectrum of LET values within a voxel because particles are constantly depositing more energy due to increased electronic interactions, so the dose-averaged LET (LETd) is commonly used in voxel-based calculations. Compared to low LET irradiation, high LET particles have a denser track structure and a higher likelihood for direct damage[18], which signifies a higher RBE[19]. However, particularly for low LET irradiation, normal tissue is more radiosensitive in well-oxygenated environments[20]. The oxygen enhancement ratio (OER) describes the increase in radioresistance in the absence of oxygen. OER is defined as the dose at a given oxygen pressure to that at normal oxygen pressure (in normoxic environments) to produce the same biological effect.

$$OER(X) = \frac{Dose_{hypoxia}(X)}{Dose_{normoxia}(X)}$$

Equation 1-2

Among other theories, the widely accepted oxygen fixation hypothesis states that ionizing radiation for low LET irradiation produces hydroxyl free radicals when reacting with water inside the patient's body. After hydroxyl radicals interact with DNA strands, the DNA can either be easily restored via chemical reduction of other molecules in the absence of oxygen, or free radicals are converted to peroxides that cannot be restored, causing DNA damage fixation in the presence of oxygen[21]. Normoxic versus hypoxic tumor cells demonstrate weaker and stronger radioresistance, respectively, in both *in vitro* and *in vivo* environments[22], making RBE alone insufficient to predict the DNA damage. Furthermore, although changes in radioresistance due to the complex hypoxia factor have been identified with heavy ions[14,23-27], the hypoxia-induced radioresistance is more prominent with protons, which have a lower and variable LET throughout their range, and warrants further investigation for relevant partial oxygen pressures between 0.5-20 mmHg[28].

Beyond chronic hypoxia, which is caused by limitations in oxygen diffusion from tumor microvessels, radiation-induced transient hypoxia also contributes to changes in radiobiological effectiveness. An emerging concept in the field of radiation therapy is the FLASH dose rate effect. FLASH radiotherapy involves an ultra-high dose rate delivery above 40 Gy/s, and compared to conventional dose rates of 5 Gy/min, can exhibit a normal tissue sparing effect while maintaining tumor control[29,30]. A recent study irradiating the whole thorax of mice with FLASH has shown evidence of tissue sparing with protons. A reduction in lung fibrosis up to 30% was found with improved overall survival[31]. A similar increase in

survival could be seen in mice undergoing whole abdomen proton FLASH irradiation[32]. Another study reported the benefit of FLASH proton pencil beam scanning on normal skin and soft tissue toxicity after the irradiation of head and neck cancers in mice[33]. Although the mechanism of the FLASH effect is not well understood, one of the hypotheses for the FLASH effect is the radiochemical depletion of oxygen leading to transient hypoxia and radioresistance[34]. Combined with the precision of proton therapy, the therapeutic potential of ultra-high dose rate delivery may revolutionize radiotherapy, if customization is achievable throughout the treatment planning process.

1.4 Beam Orientation Optimization

Because proton beams have such a strong biological component along with their physical Bragg peaks, uncertainties in range and setup are increased compared to photons. Range uncertainties could arise from changes in CT number and following conversion to stopping power ratios, as well as image artifacts. Setup uncertainties arise from shifts in patient positioning or natural changes in anatomy. These uncertainties are further compounded when using multiple treatment fields during a treatment fraction. Ideally, less treatment fields per fraction would reduce total body dose and alleviate quality assurance efforts in the treatment room. Since proton therapy is able to achieve desirable dose distributions without using greater than 5 fields, clinics have reached a consensus that 2-4 fields are sufficient for a typical IMPT treatment plan[35,36]. Limitation with fields is even more strict with carbon ion therapy due to engineering challenges with larger magnets for

beam bending and steering[37]. Carbon ion plans use only 1-2 beams in contrast to the multiple fields and arcs created by IMRT or Volumetric Modulated Arc Therapy (VMAT).

Determining the configuration of these fields, given gigabytes of information on which individual voxels are more radiosensitive than others, is not something that can be performed via trial-and-error. Beam orientation has not traditionally been included in IMRT or IMPT as an optimization variable. Instead, dosimetrists manually identified both the number of beams and their positions around the patient[35,38], which were often equiangular coplanar beams by default. Since the non-coplanar 4π space generates over a thousand candidate beams, the entirety of the inverse planning process (the quality of the optimized treatment plan) and is highly dependent on the experience and skill of a human operator.

For this reason, Gu et al. developed an automated and robust inverse IMPT beam orientation algorithm with a group sparsity term to more thoroughly search through the vast beam space and obtain better proton beam configurations[39,40]. The sensitivity-regularized and heterogeneity-weighted beam orientation optimization (SHBOO) algorithm, described in Equation 1-3, was designed for physical dose objectives to achieve superior dosimetry and robustness. It includes a dose fidelity term comprised of L2,2-norm tumor and normal tissue terms, an L1-norm spot sparsity term, an L2,1/2-norm heterogeneity weighted group sparsity term, and a sensitivity regularization term. Fluence map $\boldsymbol{x}$ is the optimization variable and the dose is $D_i = \sum_j a_{ij} x_j$. The dose calculation matrix A includes all candidate beams, with each column being the vectorized doses delivered from one intensity spot to its surrounding voxels, and is calculated in matRad, a

MATLAB-based 3D analytical dose calculation and treatment planning toolkit[41,42]. Higher tuning of α_b, which is defined in Equation 1-4, encourages less beams to be selected and lateral heterogeneity index h_b for beam b encourages the selection of beams with less sensitivity to setup uncertainties. The last term accounts for range uncertainties in the beam direction (**u**) and perpendicular to the beam (**v**) by using longitudinal and lateral sensitivity vectors with a weighting parameter λ_k. Fluence map optimization (FMO) is performed once beams are selected to optimize the intensity map of the scanning spots.

$$\underset{x}{\textbf{minimize}} \underbrace{\boldsymbol{\Gamma(Ax)}}_{\textit{Dose fidelity term}} + \underbrace{\boldsymbol{\eta\|x\|_1}}_{\textit{spot sparsity term}} + \underbrace{\textstyle\sum_{b\in\beta} \boldsymbol{\alpha_b h_b \|x_b\|_2^{\frac{1}{2}}}}_{\textit{group sparsity term}} + \underbrace{\textstyle\sum_{k\in\{u,v\}} \boldsymbol{\lambda_k s_k^T x}}_{\textit{sensitivity term}}$$
$$\boldsymbol{subject\ to\ x \geq 0}$$

Equation 1-3

$$\alpha_b = \mathrm{c}\begin{cases} \dfrac{mean(A_{CTV}^b \vec{1})}{\sqrt{n_b}}, photon \\ \left(\dfrac{\left\|A_{CTV}^b \vec{1}\right\|_2}{n_b}\right)^{1/2}, proton \end{cases}$$

Equation 1-4

1.5 Overview

The SHBOO formulation does not account for the type of particle used, the modality and speed at which dose is delivered, or patient-specific biological data such as the oxygenation of the tumor. An objective function that incorporates a well-tested RBE model into its dose fidelity term could more accurately target high RBE tumors rather than low RBE organs at risk. RBE values have been measured for cell survival under normoxic vs. hypoxic conditions, and for a given CT volume, RBE values should be adjusted for

oxygenation status before optimization. Lastly, dose rate optimization may be considered for a desired radioprotective effect.

Several studies were performed sequentially using the SHBOO-based optimization framework to investigate the roles of biology and machine characteristics in beam selection. The goals of each study were well-defined: to optimize dose in the tumor and to minimize dose to the organs at risk (OARs) while maintaining a constraint on the beams and/or spots.

Chapter 2 introduces the RBE integration problem into BOO. First, it introduces a linearization method to see whether an approximation of RBE can be used to optimize biological dose. This method emphasizes biological OAR dose sparing. The chapter is a version of the manuscript titled "Reformulated McNamara RBE-weighted beam orientation optimization for intensity modulated proton therapy", published in Medical Physics in 2022[43]. Chapter 2 also introduces a splitting method that can successfully select beams and optimize both OARs and CTVs without linearizing the RBE in each of the structures.

Chapter 3 expands on the RBE-weighted dose optimization problem to account for tumor hypoxia. The same splitting method that is introduced in Chapter 2 is tested on a new biological IMPT BOO problem that incorporates oxygen enhancement ratio into RBE. This manuscript titled "Hypoxia-informed RBE-weighted beam orientation optimization for intensity modulated proton therapy" has been published in Medical Physics in 2024[44].

Chapter 4 focuses on the treatment delivery-induced hypoxia in the critical region of interest surrounding the tumor, rather than biological dose derived from the patient anatomy. Part of the chapter is a version of the manuscript "Dose and dose rate objectives in Bragg peak and shoot-through beam orientation optimization for FLASH proton therapy"

in Medical Physics in 2022[45]. The rest of the chapter discusses the scenario in which delivery time, specifically gantry rotation time, hinders the ability for biological sparing in the critical region of interest. The study, "Split field IMPT optimization to maximize OAR dose rate and its implication for a competitive FLASH biological effectiveness", has been submitted for publication in the International Journal of Radiation Oncology Biology Physics in 2024 and discusses the opportunity for multiple beams to be delivered without sacrificing a FLASH effect, and uses a path-seeking gradient descent algorithm discussed in the published manuscript "A unified path seeking algorithm for IMRT and IMPT beam orientation optimization," which was published in the Physics in Medicine & Biology journal in 2023[46].

Finally, Chapter 5 identifies technical challenges for carbon ion radiotherapy translation into clinics. To avoid the use of a large gantry, we gently introduce the biologically-informed beam orientation optimization problem using previously-calculated RBE values for a fixed beamline setup with a rotational couch. This work, entitled "Fixed beamline optimization for intensity modulated carbon-ion therapy" was published in a special issue, IEEE Transactions on Radiation and Plasma Medical Sciences in 2021[47].

In each study, we model biological characteristics voxel-by-voxel in the dose fidelity term such that the selection of beams produces fluence maps that are more suitable for personalized treatment plans at cutting-edge particle therapy cancer centers.

2 RBE-WEIGHTED BEAM ORIENTATION OPTIMIZATION FOR OAR SPARING

2.1 Reformulated McNamara RBE-weighted beam orientation optimization

2.1.1 Introduction

Several empirical RBE models have been proposed to improve the calculation of RBE in human tissue[48-51]. Amongst these models, the McNamara model is fitted from extensive *in vitro* cell survival datasets published through 2015, making it one of the most comprehensive proton RBE models for treatment planning and optimization[51]. However, inverse optimization incorporating McNamara type of RBE is not straightforward due to its dependence on both the physical dose and LET-weighted dose. The non-linearity of the cost function renders typical optimization methods impractical. The RBE optimization problem is further complicated by the robustness consideration. As simplification, several alternative optimization problems were solved.

First, LET or LET weighted dose distribution was used as a surrogate for McNamara RBE-weighted dose distribution[52-57]. There is still debate on whether LET values alone are a sufficient input for optimization. Giantsoudi et. al. argues that variation in radiosensitivity is likely larger than variation in LET, and radiation necrosis has been shown to be correlated with dose, not with LET[58].

Second, the optimization problem was divided into subproblems calculating McNamara RBE, physical dose, and LET separately. The RBE dose was evaluated at the end of treatment planning[59,60] or sequentially in an iterative process[61], which does not promise problem convergence.

Another often overlooked factor influencing proton planning is the beam orientation selection. Compared with manually selecting beam orientations, we have shown that inverse optimization with a group sparsity term can more thoroughly search through the beam space for both superior physical dosimetry[39] and robustness[40]. Because the beam orientation separately affects the plan RBE due to the RBE variation along the beam direction, integrating RBE into the BOO framework would help select beams that are both dosimetrically and biologically desirable. To demonstrate the benefit, we previously studied LET weighted proton planning with BOO[57]. We showed that compared with manually selected beams, including LET substantially reduced the OAR LET weighted doses.

As a logical extension of previous research, in this study, we employ the same BOO framework for the RBE-weighted dose optimization problem. We reformulate the empirical McNamara model into a single and mathematically tractable optimization problem such that

the biological detail of the fitting parameters is preserved. A robustness analysis is also performed to assess the plan robustness with varying RBE considerations.

2.1.2 Methods

The general goal of our IMPT McNamara RBE-based BOO algorithm is to select 2-4 beams out of all candidate beams and simultaneously generate a robust fluence map that minimizes biological dose in the OARs while maintaining dose to the target, all while achieving sufficient physical dose distribution.

2.1.2.1 RBE-weighted Dose Fidelity

In a typical inverse optimization problem, we set the initial biological dose fidelity as

$$\boldsymbol{\Gamma(Ax)} = \sum_{\boldsymbol{i\in\mathcal{T}}} \boldsymbol{\omega_i} \left\| \boldsymbol{RBE_i(x)} \cdot \boldsymbol{D_i} - \boldsymbol{q_i} \right\|^2 + \sum_{\boldsymbol{i\in\mathcal{O}}} \boldsymbol{\omega_i} \left\| \boldsymbol{RBE_i(x)} \cdot \boldsymbol{D_i} - \boldsymbol{m_i} \right\|_+^2$$

Equation 2-1

where fluence map $\boldsymbol{x}$ is the optimization variable, dose is $D_i = \sum_j a_{ij} x_j$ and dose-averaged LET is $LETd_i = \frac{1}{D_i} \sum_j l_{ij} a_{ij} x_j$. The dose calculation matrix A includes all candidate beams, with each column being the vectorized doses delivered from one intensity spot to its surrounding voxels. The LET calculation matrix, L, is calculated similarly to dose matrix A for vectorized LET-weighted dose. Dose is multiplied voxel-wise by proton RBE vectors for each structure. The "·" represents the Hadamard product. The phenomenological McNamara model is used to calculate RBE values for protons in each voxel and is formulated as

$$RBE\left(D, \left(\frac{\alpha}{\beta}\right)_x, LET_d\right) = \frac{1}{2D}\left(\sqrt{\left(\frac{\alpha}{\beta}\right)_x^2 + 4D\left(\frac{\alpha}{\beta}\right)_x\left(p_0 + \frac{p_1}{(\alpha/\beta)_x} LET_d\right) + 4D^2\left(p_2 + p_3\sqrt{(\alpha/\beta)_x} LET_d\right)^2} - \left(\frac{\alpha}{\beta}\right)_x\right)$$

Equation 2-2

The fit coefficients are p0=0.99064 (Standard Error (SE) 0.014125), p1=0.35605 (SE 0.015038), p2=1.1012 (SE 0.0059972), and p3=-0.0038703 (SE 0.00091303)[51]. Without losing generality, the alpha-beta ratio values from reference photons $\left(\frac{\alpha}{\beta}\right)_x$ were assigned 10 Gy in the target volumes and 3 Gy in the surrounding normal tissues.

The first term minimizes the difference between the RBE-weighted dose to the target volumes $\mathcal{T}$ and the prescribed biological dose (GyRBE) q; the second one-sided quadratic term minimizes dose to OAR $\mathcal{O}$, where m is the maximum allowable biological dose (GyRBE) in that structure. Individual structure tuning is controlled by weights ω_i. CTV volumes were assigned highest priority.

However, this optimization problem is difficult to solve since Equation 2-2 also depends on optimization variable $\boldsymbol{x}$. We propose an alternative approach for incorporating the McNamara model within the optimization framework.

2.1.2.2 Reformulated McNamara RBE-Weighted Dose Fidelity

The alternative approach attempts to optimize the total dose in each structure. In inverse optimization schemes, the objective function is formulated to account for minimum and maximum dose constraints to the target and for maximum dose constraints to the OARs[56]. Since it would be difficult to satisfy both maximum and minimum total dose constraints in the target volume without loss of homogeneity, the following approach assumes previously calculated values of RBE (via physical dose optimization), which are static during the CTV biological dose optimization, and for OARs, a direct reduction of

biological dose using reformulated McNamara RBE values. The McNamara model can be written more simply as

$$(RBE \times D)_i = \frac{1}{2}\sqrt{a_1 + a_2 D_i + a_3 (LET \times D)_i + (a_4 D_i + a_5 (LET \times D)_i)^2} + a_6$$

Equation 2-3

where a_1-a_6 are constants derived from parameters in the McNamara model. For OARs, minimization of Equation 2-1 can be equivalently achieved by minimizing the following function $f_i(x)$,

$$f_i(x) = a_1 + a_2 D_i x + a_3 (LET \times D)_i x + (a_4 D_i x + a_5 (LET \times D)_i x)^2$$

Equation 2-4

Summing over all voxels, we obtain a new set of biological dose fidelity terms for OARs in Equation 2-5. $\vec{c}$ is the sum over the columns of matrix $a_2 D_i + a_3 (LET \times D)_i$ and H is simply $a_4 D_i + a_5 (LET \times D)_i$.

$$f(x) = \sum_i f_i(x) = \vec{c}x + \|Hx\|_2^2 + \text{constant}$$

Equation 2-5

The optimization problem is then extended in Equation 2-6 to include our previously formulated sensitivity and heterogeneity weighted group sparsity terms,

$$\underset{x}{\text{minimize}} \underbrace{\vec{c}\boldsymbol{x} + \|H\boldsymbol{x}\|_2^2}_{OAR\ RBE\ term} + \underbrace{\|RBE \cdot A\boldsymbol{x} - d\|_2^2}_{Static\ RBE\ dose\ for\ CTV} + \underbrace{\sum_{b\in\beta} \alpha_b h_b \|\boldsymbol{x}_b\|_2^{\frac{1}{2}}}_{group\ sparsity\ term} + \underbrace{\sum_{k\in\{u,v\}} \lambda_k \boldsymbol{s}_k^T \boldsymbol{x}}_{sensitivity\ term}$$
$$subject\ to\ \boldsymbol{x} \geq 0$$

Equation 2-6

where $\boldsymbol{x}_b$ is a vector representing the intensities of scanning spots from the candidate beam b, so optimization variable $\boldsymbol{x}$ is the concatenation of all vectors $\boldsymbol{x}_b$ ($b \in \beta$). The third term is

an L2,1/2-norm group sparsity term. A proper value of weighting hyperparameter α_b is set for each beam, defined as

$$\alpha_b = z\left(\frac{\left\|A_{CTV}^{b}\vec{1}\right\|_2}{n_b}\right)^{p/2}$$

Equation 2-7

, where A_{CTV}^{b} is the dose calculation matrix of the target volume for beam b, n_b is the number of candidate spots in beam b, and z is a regularization parameter. This weight ensures that most beams are penalized to be identically zero, turning most candidate beams off, and leaving a small number (2-4) of beams active. Parameter z is tuned higher to further force convergence to a smaller number of active beams. The lateral tissue heterogeneity observed along beam b is represented by its heterogeneity index h_b, choosing beams with less sensitivity to setup uncertainties. The fourth term is a sensitivity regularization term, where λ_k is a regularization parameter, $\boldsymbol{s_u}$ and $\boldsymbol{s_v}$ are longitudinal and lateral sensitivity vectors that account for range uncertainties for each spot in each beam, both in the beam direction ($\mathbf{u}$) and perpendicular to the beam ($\mathbf{v}$)[62].

FISTA, an accelerated proximal gradient method known as the Fast-Iterative Shrinkage Thresholding Algorithm[63], or Chambolle-Pock, a primal-dual algorithm[64], are used to solve this non-differentiable problem. Both proximal gradient and first order primal dual methods have efficiently solved inverse optimization problems with applications to treatment planning in the past[65,66] and are straightforward to implement for large scale, nondifferentiable, constrained convex optimization problems using a faster line-search method. Other algorithms like the alternating direction method of multipliers (ADMM)[67] must solve a large linear system at each iteration, while algorithms like CP and

FISTA require only matrix-vector multiplications[68]. Compared with CP with convergence rate of $O(1/k^2)$ FISTA is faster because of its high convergence rate of $O(1/k^2)$[69]. On the other hand, for non-convex problems such as the one at hand, CP may find a better local minimum[70]. Therefore, both solvers are studied here. The solution for the FISTA method is found in Appendix 6.1 and the CP method is described in Appendix 6.2.

2.1.2.3 Comparison with LET-Weighted Dose Fidelity

The above McNamara formulation is compared with our previously developed LETwBOO framework[57] to determine the efficacy of integrating RBE into proton treatment planning. Using the same SHBOO-FMO basis, the LET-weighted optimization problem is

$$\underset{x}{\text{minimize}} \sum_{i\in\mathcal{T}} \omega_i \|D_i - q_i\|^2 + \sum_{i\in\mathcal{O}} \omega_i \|D_i - m_i\|_+^2$$

$$+ \sum_{i\in\mathcal{T}} \omega_i \left\|LETd_i \cdot D_i - (LD)_i^{ref}\right\|^2 + \sum_{i\in\mathcal{O}} \omega_i \|LETd_i \cdot D_i\|_+^2 + \sum_{b\in\beta} \alpha_b h_b \|\boldsymbol{x}_b\|_2^{\frac{1}{2}} + \sum_{k\in\{u,v\}} \lambda_k \boldsymbol{s}_k^T \boldsymbol{x}$$

$$subject\ to\ \boldsymbol{x} \geq 0$$

Equation 2-8

The first two terms represent conventional physical dose fidelity and the third and fourth terms represent the LET x D conditions. $(LD)_i^{ref}$ is the minimum LET-weighted dose in the CTV to prevent cold spots in the biological dose. It was evaluated as the mean LET-weighted dose from conventional plans optimizing physical dose with manually selected beams. This problem was solved using FISTA.

2.1.2.4 Patient Evaluations

Three bilateral head-and-neck (HN) patients were tested. The original candidate beam set of 1162 non-coplanar beams was evenly distributed across a 4π space with 6° separation. A subset of about 220 beams were used for the head and neck patients, the rest excluded due to infeasible depths, undesired entrance through incompletely segmented vital organs as a result of limited CT range, or collisions between the proton nozzle and patient or couch. All beams were tested for collision using 3D visualizations of STL files of the IBA Proteus Plus gantry with PBS-dedicated nozzle, scissor couch, and each of the patient masks[71]. A range shifter was added to degrade the proton range to treat at superficial depths[72]. The dose loading matrix *A* and LET matrix *L* were calculated using matRad v2.1.0[41,42], describing the dose and LET from the scanning spots covering the CTV and a 5 mm margin to a voxels of resolution 2.5 x 2.5 x 2.5 mm^3. Energies are interpolated in matRad to achieve a uniform layer spacing of 3 mm in the beam direction, and the spot spacing in the lateral direction was 5 mm (please refer to matRad documentation for more information on dose influence matrix calculation). A single fraction was assumed purely for mathematical purposes to see how the optimization behaves with extreme values of proton dose and RBE. The CTV was set as the optimization target and CTV-based robust optimization was performed. The prescription dose, target volume, and average number of spots per beam for each patient are shown in Table 2-1.

Case		Prescription dose (GyRBE)	CTV volume (cc)	Average spots per beam
H&N 1	CTV54 CTV60	54 60	141.29 160.89	10065

	CTV63	63	68.00	
H&N 2	CTV54 CTV60	54 60	108.00 127.26	10077
H&N 3	CTV54 CTV60 CTV63	54 60 63	110.38 98.94 10.23	9433

Table 2-1. Prescription doses, CTV volumes and average number of spots per beam for each patient.

Three plans were created for each patient, all of them including group sparsity-based beam orientation optimization (SHBOO): 1) optimization of physical dose using the FISTA algorithm (Phys-FISTA); 2) optimization of the reformulated McNamara RBE-weighted dose using FISTA (McNam-FISTA); 3) optimization of the reformulated McNamara RBE-weighted dose using Chambolle-Pock (McNam-CP). A separate analysis is conducted with a fourth plan that was created for all three patients: 4) optimization of LET-weighted dose using FISTA (LET-FISTA), for direct comparison against McNam-FISTA. For each patient, all four plans were optimized using the same structure weighting. All plans are optimized using their respective biological dose fidelity terms. Once all optimizations were completed and fluence maps were obtained, final RBE dose (GyRBE) for each plan was calculated using Equation 2-3 and compared.

Plans were normalized such that 95% of the target volumes received the prescribed dose. CTV homogeneity, D95%, D98%, and maximum dose were evaluated. CTV homogeneity is defined as D95% /D5%. The maximum dose is defined as the dose to 2% of

the structure volume, D2%, following the recommendation by ICRU-83[73]. The mean and maximum doses for OARs were also evaluated. The robustness analysis considered twenty-one scenarios: a result of all combinations of (a) two range uncertainty worse-case scenarios, by scaling the CT number ± 3% and (b) six setup uncertainty worst-case scenarios, by shifting the beam isocenter by ± 3 mm along anteroposterior, superior-inferior, and mediolateral directions. The range and setup uncertainties were combined in the robustness analysis since they are not mutually exclusive. The robustness of each plan was evaluated by the DVH band plots[74]. Worst Dmax, D98%, D95%, and V95% for each CTV and worst Dmean and Dmax for OARs were calculated between plans.

2.1.3 Results

2.1.3.1 Runtime and Selected Beams

The dose, sensitivity and heterogeneity calculation for all candidate beams were performed with MATLAB and the Parallel Computing Toolbox on an i7 12-core CPU desktop. The average time per beam to calculate this data, along with the total beam orientation with fluence map optimization runtime for Phys-FISTA, McNam-FISTA, McNam-CP, and LET-FISTA for each patient is listed in Table 2-2. Dose calculation among patients used the same ray-tracing procedure in matRad for the same number of candidate beams[57]. Lateral tissue heterogeneity index values of all scanning spots in the same beam are calculated and averaged to represent the beam heterogeneity, adding more time to initial calculation[40]. The McNam-FISTA and McNam-CP plans increased the total optimization

time by 130-410% and 400-1370%, respectively, compared to Phys-FISTA. Since both McNamara plans use extra terms in their objective functions to accurately represent biological dose fidelity, it is understood that total optimization time increases. There is an 8-350% increase in runtime between FISTA and CP. Even with a higher regularization parameter z, CP struggled to produce less than 4 beams during beam selection. The increase can also be attributed to the fact that computation of additional proximal operators was necessary for reformulating the objective function into the CP standard form. McNam-FISTA increased optimization time on average by 11% compared to LET-FISTA.

	Calculation time (min)			SHBOO-FMO runtime (min)			
Case	Dose	Sensitivity	Hetero-geneity	Phys-FISTA	McNam-FISTA	McNam-CP	LET-FISTA
H&N 1	51	4	682	24	55	247	44
H&N 2	63	7	700	19	88	95	93
H&N 3	43	3	690	10	51	147	45

Table 2-2. Preparation time and runtime of each SHBOO-FMO method for the tested patients.

The couch and gantry angles for the beams for each case are listed in Table 2-3. The angle notation follows IEC 61217 coordinate conventions. A three-dimensional portrayal of beam angles selected are shown in Figure 2-1.

	Beams Selected (gantry, couch)			
Case	Phys-FISTA	McNam-FISTA	McNam-CP	LET-FISTA

H&N 1	(270,18), (30, 88)	(270,18), (30, 88)	(311, 41), (270, 18), (37, 43), (30,88)	(270, 18), (324, 301), (30, 88)
H&N 2	(101, 342), (316, 314)	(36,0), (316, 314), (30, 88)	(36,0), (315, 314), (321,308), (31,76)	(33, 294), (54, 353), (324, 301), (30,88)
H&N 3	(270, 18), (30, 88)	(333, 297), (30, 88)	(329,52), (43,18), (321, 308), (328, 291)	(270, 18), (101, 342), (25, 346), (312, 352)

Table 2-3. Beam angles (gantry, couch) in degrees selected for each patient.

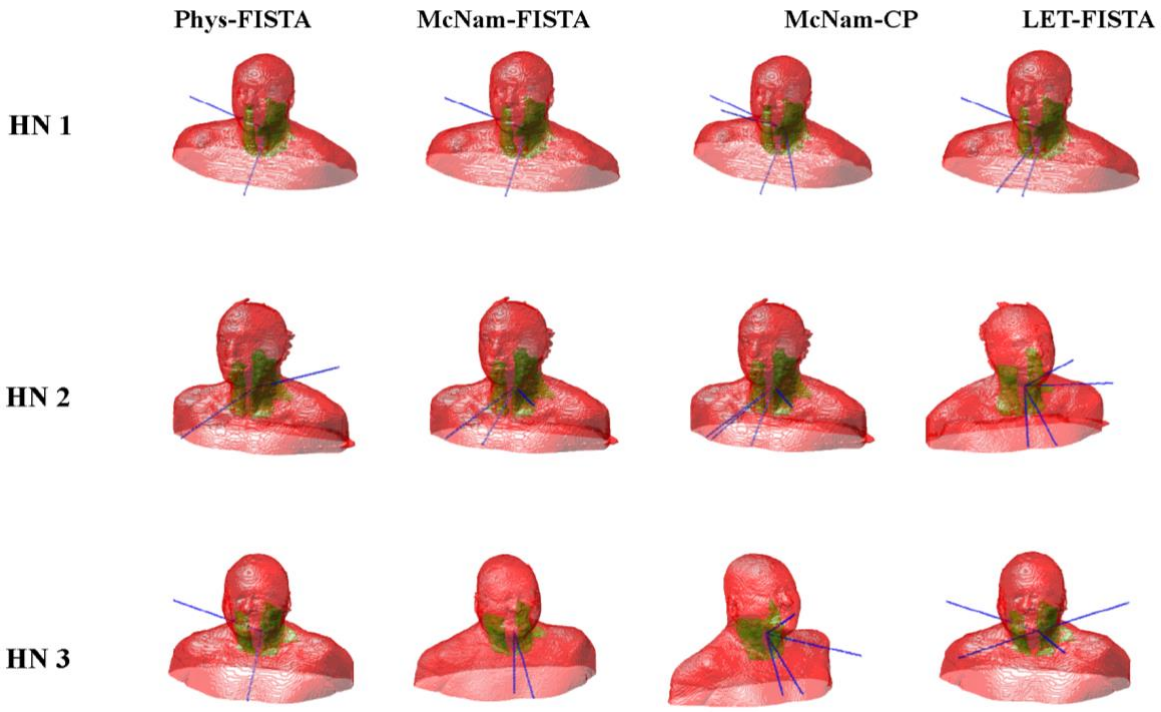

Figure 2-1. Beam angle comparison between Phys-FISTA, McNam-FISTA, McNam-CP, and LET-FISTA (left to right) for all three patients. CTVs are shown in green and blue lines represent beams entering the patient.

2.1.3.2 Patient Dosimetry

The dosimetric features across plans can be seen in Figure 2-2. Dose maps for each patient are normalized to the same biological dose for clear comparison. Compared to Phys-FISTA, CTV homogeneity index (HI) and maximum biological dose (Dmax) are either matched or improved by McNam-CP by an average of 0.00 and 0.05% of the prescription dose, respectively. McNam-FISTA did not improve the CTV homogeneity as shown by an average decline of 0.02 and 8.2% for HI and Dmax compared to Phys-FISTA. D95% and D98% are changed by McNam-FISTA and McNam-CP by [-3.5%, -0.3%] and [1.4%,0.8%] of the prescription dose, respectively, compared to Phys-FISTA. CTV statistics for the three patients are listed in Table 2-4. The best homogeneity indices were the highest values, and the best Dmax, D95%, and D98% values were the ones closest to the prescription dose for that CTV.

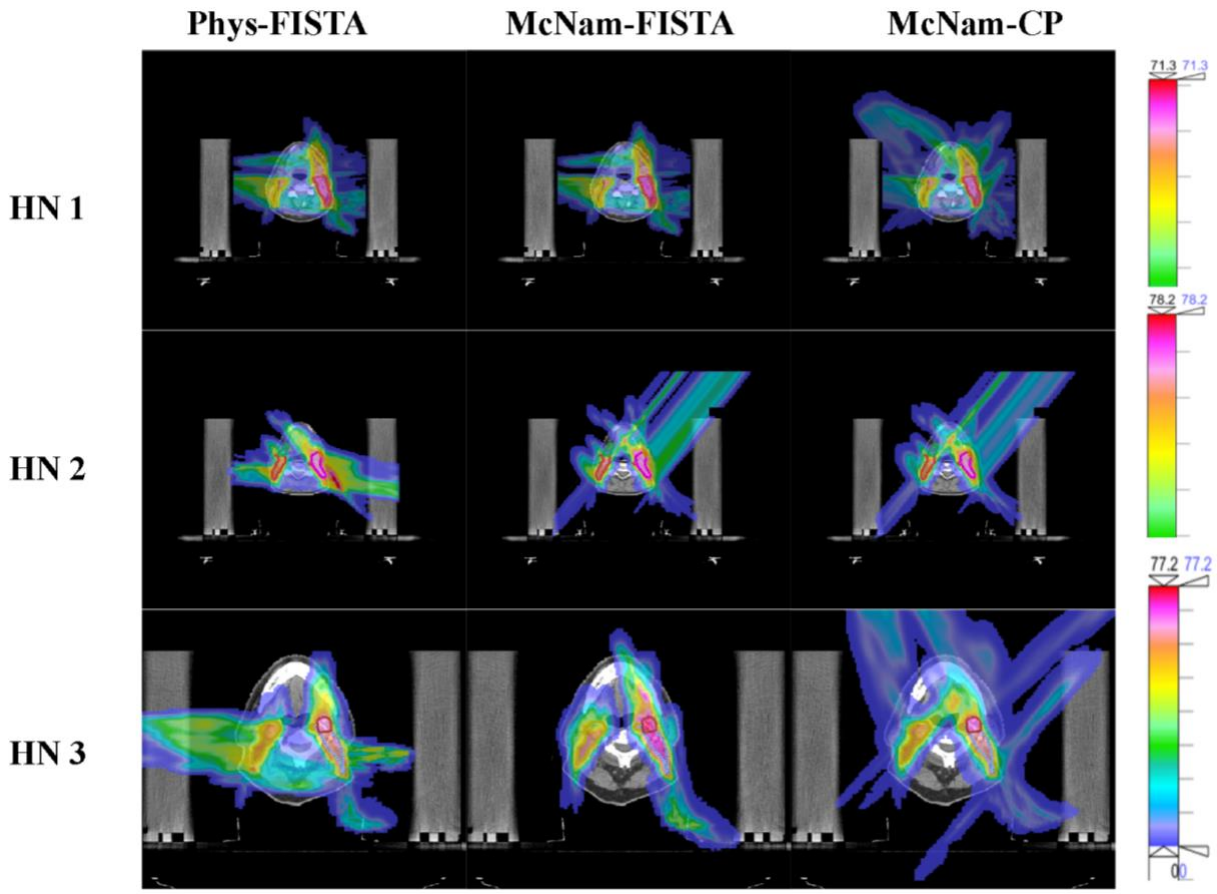

Figure 2-2. Isodose comparison in the transverse plane between Phys-FISTA, McNam-FISTA, McNam-CP (left to right) for all three patients.

	HI			Dmax			D95%		
Case	Phys-FISTA	McNam-FISTA	McNam-CP	Phys-FISTA	McNam-FISTA	McNam-CP	Phys-FISTA	McNam-FISTA	McNam-CP
HN #1									
CTV54	0.911	0.883	**0.921**	60.5	62.4	**59.8**	54.0	54.0	**54.0**
CTV60	**0.941**	0.925	0.932	65.6	68.0	**65.3**	61.2	62.0	**60.3**
CTV63	**0.948**	0.933	0.946	65.9	67.9	**65.6**	62.0	**62.6**	61.4

HN #2									
CTV54	0.877	0.842	**0.890**	62.5	66.2	**62.2**	**54.0**	**54.0**	**54.0**
CTV60	0.899	0.905	**0.919**	69.4	71.6	**69.3**	**61.6**	63.8	62.8
HN #3									
CTV54	**0.930**	0.817	0.928	**58.9**	67.1	59.1	**54.0**	**54.0**	**54.0**
CTV60	0.930	0.915	**0.937**	65.2	74.2	**65.1**	**59.9**	66.9	60.4
CTV63	0.930	0.914	**0.932**	**67.8**	76.6	69.3	**62.6**	69.2	64.0

Table 2-4. CTV statistic comparison between three methods for all patients. All biological dose values are reported in GyRBE. Best values are denoted in bold.

All RBE-weighted plans met the dosimetric standards set during optimization. Generally, relatively large improvement could be seen in the mean and maximum biological doses of all structures with the McNamara plans compared to the physical dose plan. Table 2-5 reports these dose statistics for all structures. The best values denoted were the lowest values across plans. [Dmean, Dmax] (GyRBE) were improved by [-1.8, 7.3] in the right submandibular gland, [1.7, 1.8] for the left parotid, [4.6, -2.0] for the right parotid, [4.0, 11.5] in the larynx, [2.3, 6.4] for constrictors, [4.5, 19.5] in the esophagus, and [5.1, 36.2] in the spinal cord for McNam-FISTA, with negative values representing better performance with Phys-FISTA. Similarly, [Dmean, Dmax] (GyRBE) were improved by [2.9, 7.4] in the right submandibular gland, [2.1, 0.8] for the left parotid, [4.5, -0.6] for the right parotid, [1.8, 5.2] in the larynx, [0.3, -1.1] for constrictors, [4.3, 19.5] in the esophagus, and [5.1, 36.2] in the spinal cord for McNam-CP. Biological dose volume histograms for the three H&N patients are shown in Figure 2-3.

HN #1	HN #2	HN #3

	Phys-FISTA	McNam-FISTA	McNam-CP	Phys-FISTA	McNam-FISTA	McNam-CP	Phys-FISTA	McNam-FISTA	McNam-CP
Right subm.									
Gland									
Dmean	6.6	**3.4**	4.6	13.1	**5.5**	6.6	10.8	27.0	**10.5**
Dmax	34.8	**25.7**	28.6	47.2	**30.2**	32.6	39.7	43.9	**38.4**
Left Parotid									
Dmean	7.0	**5.1**	5.4	12.6	**7.2**	9.1	9.8	12.0	**8.7**
Dmax	44.7	**38.9**	40.9	46.8	**40.2**	46.0	**49.8**	56.8	52.1
Right Parotid									
Dmean	13.4	**12.1**	12.2	7.3	**5.9**	7.5	19.2	8.2	**6.8**
Dmax	**44.4**	46.2	45.1	44.5	**43.5**	47.9	46.2	51.4	**43.9**
Larynx									
Dmean	3.6	**2.3**	3.4	13.6	**4.4**	7.7	3.7	**2.1**	4.4
Dmax	20.0	**15.6**	18.5	54.5	**30.0**	39.6	20.5	**15.0**	21.3
Constrictors									
Dmean	3.2	**1.3**	3.2	8.7	**4.8**	6.4	4.3	**3.2**	5.8
Dmax	17.2	**11.8**	18.0	43.7	**33.1**	37.6	27.3	**24.2**	35.9
Esophagus	N/A	N/A	N/A						
Dmean				9.2	**1.0**	1.3	1.8	**1.0**	1.1
Dmax				46.3	**10.1**	11.1	10.5	7.8	**6.7**
Spinal Cord									
Dmean	3.2	2.5	**2.2**	6.0	**0.0**	**0.0**	4.1	**0.0**	**0.0**
Dmax	14.0	12.1	**9.5**	43.4	0.4	**0.3**	29.4	**0.0**	**0.0**

Table 2-5. OAR statistics comparison between three methods for all patient under. RBExDmean (Dmean for simplification) and RBExDmax (Dmax) are reported in GyRBE. Best values are denoted in bold.

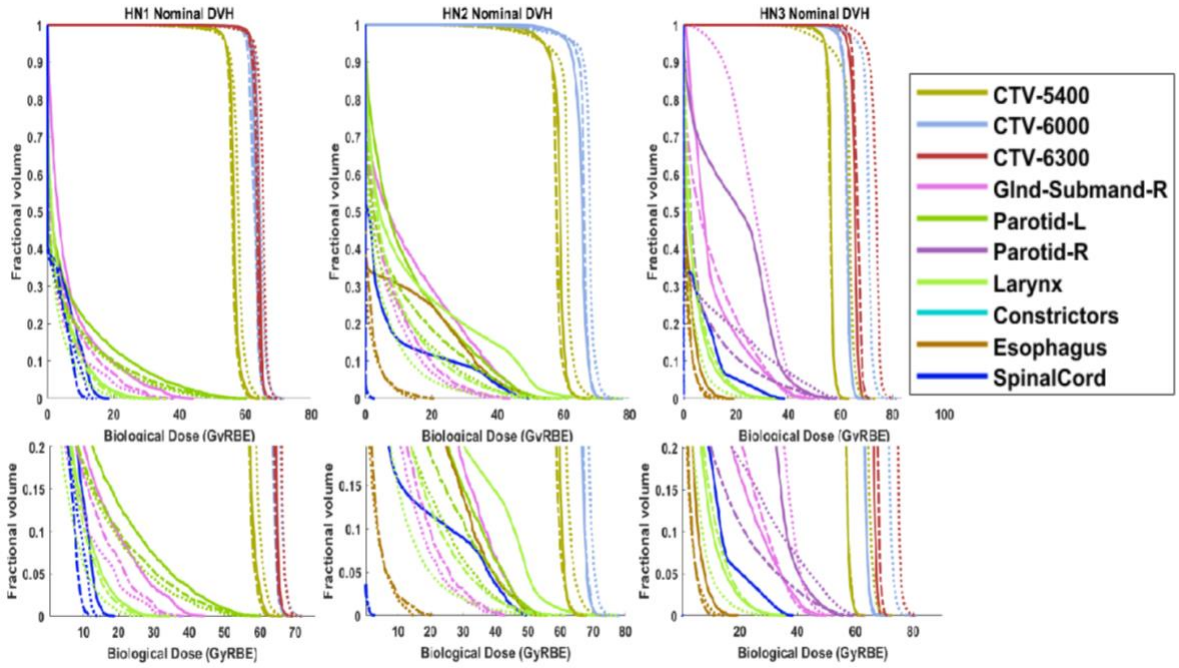

Figure 2-3. Biological dose volume histograms for all patients. Solid lines represent Phys-FISTA, dotted lines represent McNam-FISTA and dashed lines represent McNam-CP. The bottom set of images is included as magnification of the above DVHs. Select structures are shown for each patient to portray the larger differences in dosimetry between plans.

2.1.3.3 Plan Robustness

All plans were optimized to account for uncertainties in range and setup due to sensitivity regularization and heterogeneity weighting. The DVH bands of the three methods are shown in Figure 2-4. CTV robustness was improved for both McNam-FISTA and McNam-CP. Under range and setup uncertainties, narrower DVH bands, showing superior robustness, were generally observed with the McNam-CP plans for OARs compared to Phys-FISTA. McNam-FISTA also managed to provide comparable OAR robustness to Phys-FISTA plans.

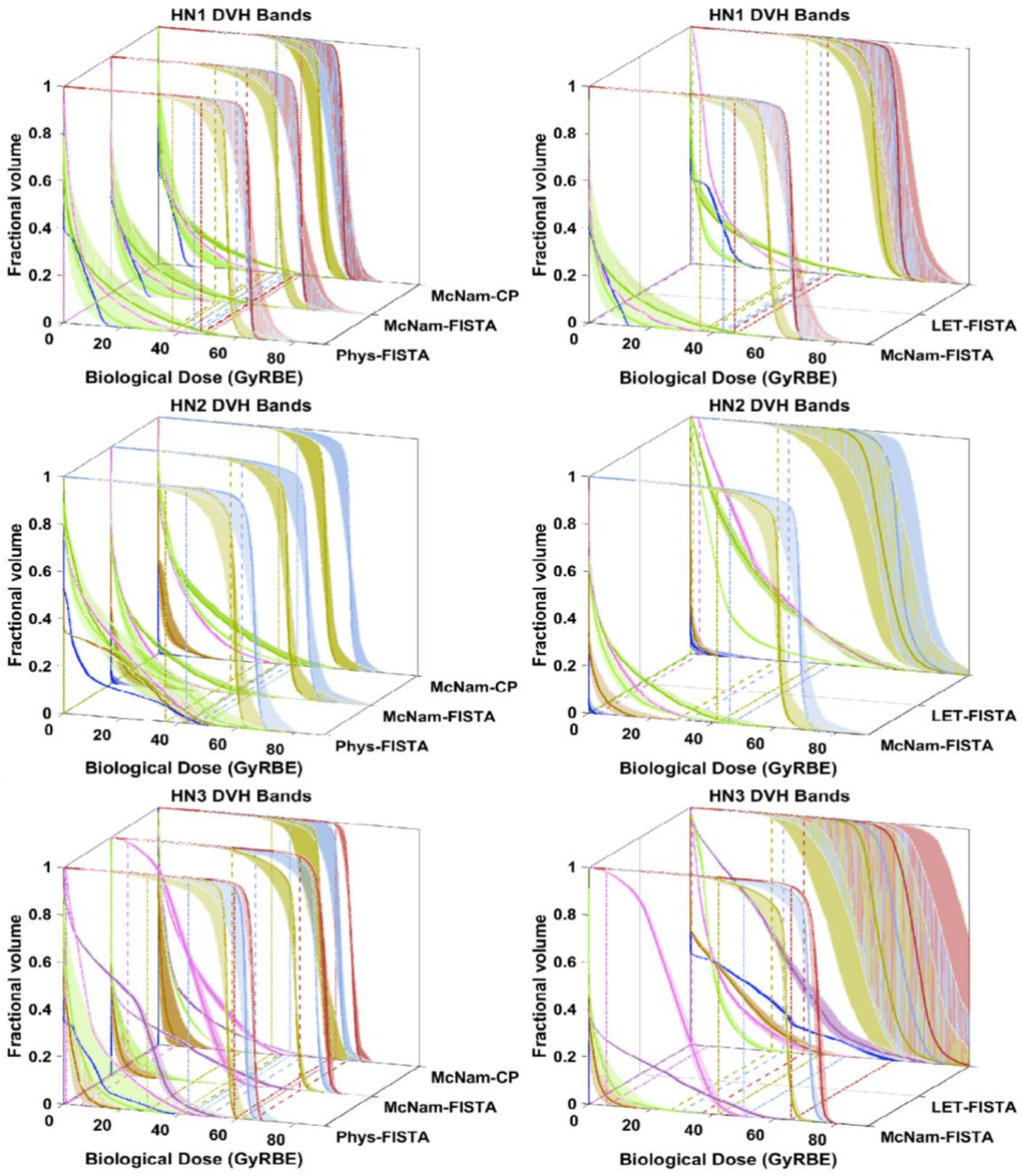

Figure 2-4. DVH band plots for three H&N patients, indicating the robustness of the beams chosen by different methods. Worst case comparison for the McNamara plans compared to Phys-FISTA are shown on the left and comparison of McNam-FISTA with LET-FISTA are shown on the right. The worst D98% of each method is labeled by reference lines in the x-y plane. Select structures are shown on each subplot to portray the larger differences in robustness between plans.

The worst (highest) Dmax, and worst (lowest) V95%, D95%, and D98% of each CTV were calculated and plotted in Figure 2-5. On average, the worst [Dmax, V95%, D95%, D98%] improved by [-6.6%, 6.2%, 6.0%, 4.8%] with McNam-FISTA and [2.7%, 2.7%, 5.3%, -4.3%] with McNam-CP compared to Phys-FISTA. The worst Dmax and Dmean for each OAR under range and setup uncertainty combinations were calculated and plotted in Figure 2-6. The worst [Dmax, Dmean] was improved by McNam-FISTA and McNam-CP by an average of [25.0%, 19.2%] and [29.5%, 36.5%], respectively.

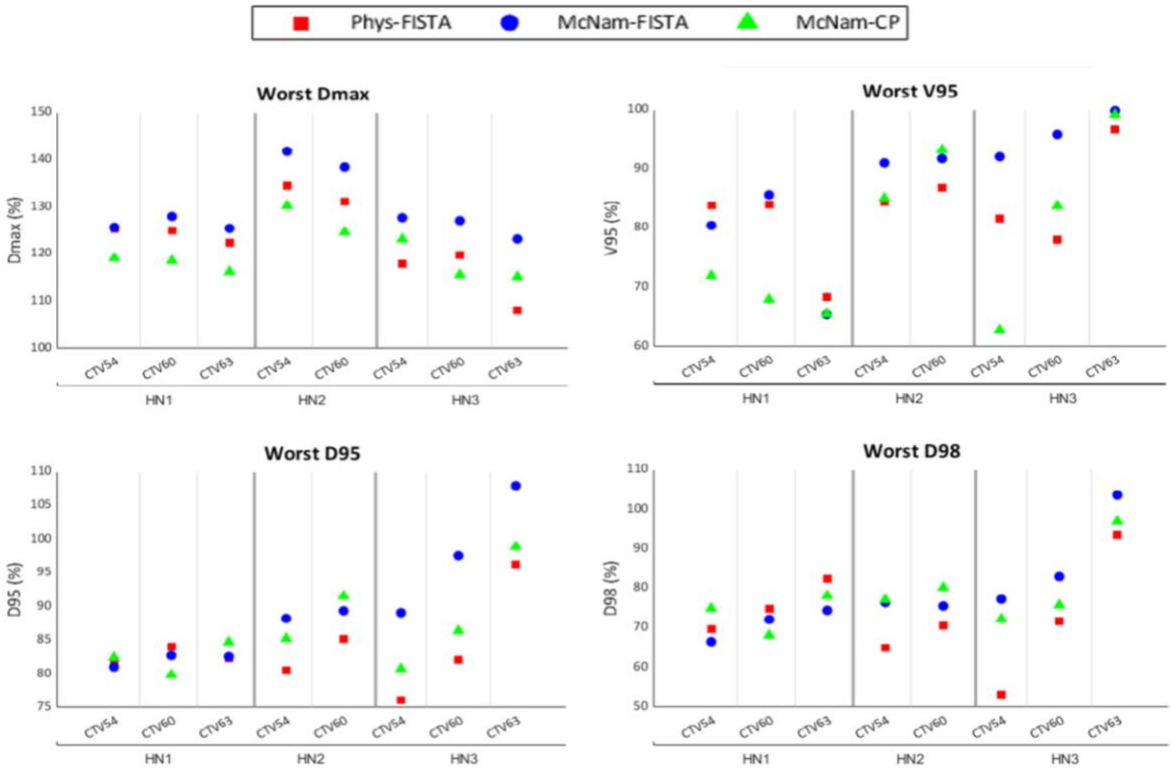

Figure 2-5. A comparison of worst Dmax, V95%, D95%, and D98% of the CTVs for each patient under range and setup uncertainties between Phys-FISTA, McNam-FISTA, and McNam-CP. Doses and volume are shown as a percentage of the prescription dose and total volume.

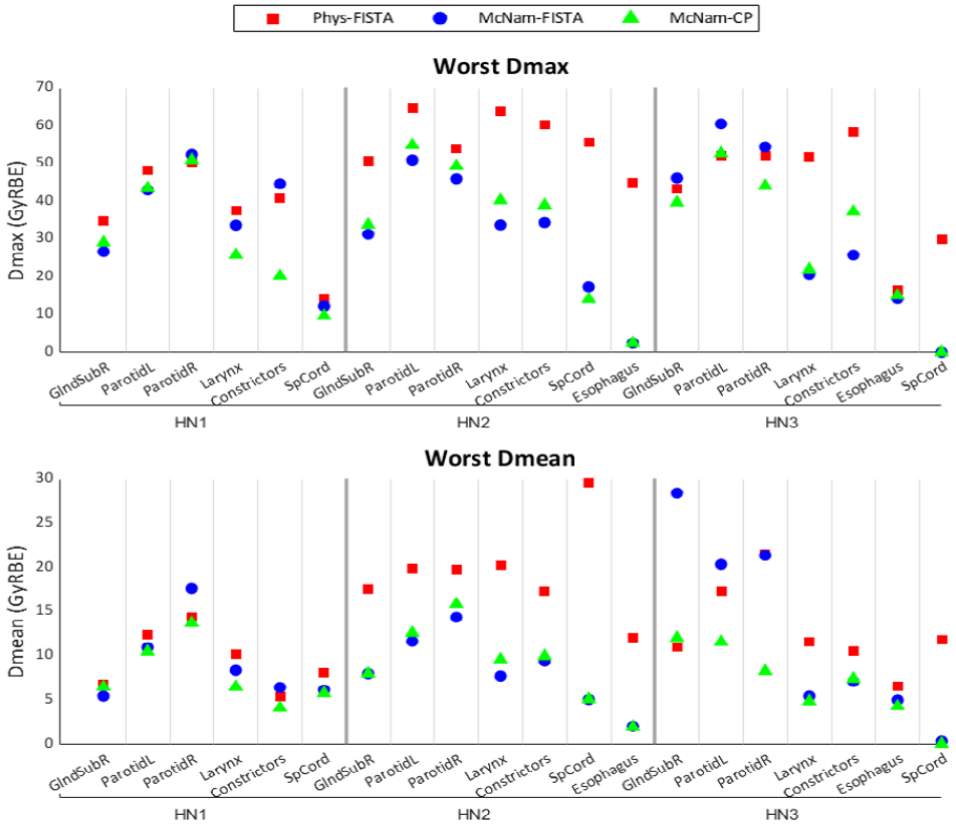

Figure 2-6. Worst Dmax and Dmean for each OAR in each patient under various uncertainties between Phys-FISTA, McNam-FISTA, and McNam-CP. Dose values are given in GyRBE.

2.1.3.4 McNamara RBE Comparison with LET

Tumor coverage and normal tissue sparing with McNam-FISTA plans were compared directly to LET-FISTA plans for all patients as well. McNam-FISTA was able to improve tumor [HI, Dmax, D95%, D98%] by [0.08, 10.8%, -3.0%, 0.4%]. Average [Dmean, Dmax] (GyRBE) were improved by McNam-FISTA by [0.9, 9.8] in the right submandibular gland, [5.2, 8.2] for the left parotid, [8.6, 7.6] for the right parotid, [2.9, 4.4] in the larynx, [7.0, 16.0] for constrictors, [3.3, 12.3] in the esophagus, and [5.1, 36.2] in the spinal cord.

Figure 2-7 shows a biological dose volume histogram comparison between plans for the three patients.

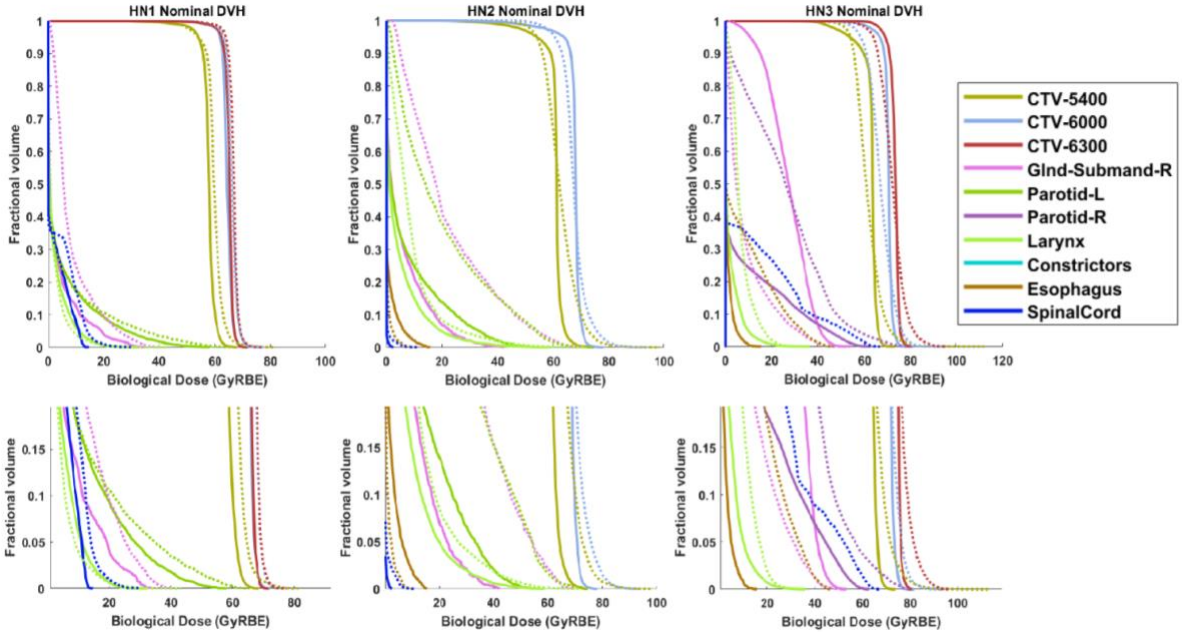

Figure 2-7. Biological dose volume histograms for all patients. Solid lines represent McNam-FISTA and dotted lines represent LET-FISTA. The bottom set of images is included as magnification of the above DVHs. Select structures are shown for each patient to portray the larger differences in dosimetry between plans.

In terms of CTV robustness, the worst [Dmax, V95%, D95%, D98%] improved with McNam-FISTA compared to LET-FISTA by [26.2%, 21.1%, 19.9%, 37.0%] under range and setup uncertainties. For OARs, however, the worst [Dmax, Dmean] was worsened by McNam-FISTA under uncertainties by an average of [2.3%, 4.4%]. The right-hand side of Figure 2-4 shows a biological DVH band plot representing the robustness comparison.

Although the McNamara model preferentially spares OARs, the OAR sparing is less robust than the LET model. For CTVs, the McNamara model is more robust. This shows that

for LET-FISTA, Bragg peaks are placed away from the distal edge of the CTV, giving a large range of RBE values within the tumor, showing a trade-off between dosimetry and robustness.

2.1.4 Discussion

In this study, we have reformulated the phenomenological McNamara RBE equation for tractable optimization solution. The McNamara RBE is directly incorporated into the BOO framework that performs a global search among all feasible candidate beams for optimal physical and biological dose distribution. Compared with previous approaches appending RBE or LET optimization to the physical dose optimization the linear McNamara reformulation further reduces biological dose in OARs without loss of tumor coverage.

The alpha/beta values used in this study are generalized based on type of structure (OAR vs CTV) rather than specific cell line. However, these values directly impact the voxel-based McNamara RBE calculations for each method. A Monte Carlo robustness study has gathered the uncertainties listed for the McNamara model parameters and alpha/beta values from a variety of studies[75]. Uncertainties in tumor radiobiology and their varying endpoints propagate errors throughout the optimization, disrupting the accurate assessment of tissue toxicities. While further investigations are needed to better understand the radiobiology of proton therapy, a method improving biological effectiveness is a safe and clinically acceptable solution.

From *in vitro* linear-quadratic model-based studies, we see several trends with RBE, namely, that RBE increases linearly with LETd, that RBE increases as dose decreases, and

RBE increases as the alpha-beta ratio decreases. However, we note that *in vitro* RBE models do not account for tissue and tumor heterogeneity, interactions of cells with their microenvironment, nor do they account for the role of the immune system[51]. A migration to *in vivo* modelling or mechanistic RBE models would generate further understanding of RBE's dependencies, particularly for heavy ions. Microdosimetric quantities can be modelled extensively via Monte Carlo track structure simulations (Geant4-DNA, TOPAS-nBio, PARTRAC)[76-78] to characterize the distribution of particle interactions within small volumes. To do this, other RBE models were proposed, such as the microdosimetric kinetic model (MKM)[79], the local effect model (LEM)[80], and the repair-misrepair fixation model (RMF)[81], all three of which are calculated from the repair of double-strand breaks and closer characterization of sublethal and potentially lethal damage to DNA. Even with these mechanistic models, there is still large variation in DNA damage prediction and resulting translation from the molecular level to the organ level. With our studies, we choose to use empirical data for ease of translation into the mathematical formulation, and from a voxel-based dose map, a generalized equivalent uniform dose (gEUD)[82] may be calculated for individual structures to incorporate structure seriality and likelihood of survival/ complication.

Because the main concern for the proton RBE is on normal organs[83,84], to formulate the RBE optimization problem for tractable solution, we focused our efforts on RBE-dose in the OAR structures. Since the OAR RBE term in Equation 2-6 represents a minimization over the total dose in the structure volume, the goal for total dose can be 0 GyRBE if for all voxels the desired dose is 0 GyRBE. It is not as straightforward to optimize the total CTV dose around a set value if, in each voxel, the dose is then allowed to significantly vary from

prescription dose. This would lead to inhomogeneity within the CTV. Although the reformulated method is not applied to the CTVs, McNamara RBE should still be incorporated into CTV dose optimization since *in vivo* RBE within large HN tumors may not be uniformly 1.1. Voxel-based RBE values for CTVs are therefore calculated via physical dose optimization prior to McNamara RBE-based optimization.

Because RBE values are largely dependent on LET values, the method calculation of LET values should be noted for this study. Due to the prohibitively long time required to calculate dose and LET for over 200 candidate beams using Monte Carlo, the current study used an analytical method for all patients. While the analytical method was shown to be acceptably accurate for dose calculation and BOO planning in previous studies[39,40], it is limited in LET calculation accuracy due to reasons including failing to account for secondary protons[85]. The deficiency is shown as overestimation of LET in the low-density region compared with the Monte Carlo method. It is also observed that a different dose and LET calculation method can result in different optimized beams.

A comparison between optimization algorithms was performed using the same formulation for our objective function. The problem is efficient to solve using FISTA, which has an optimal convergence rate of $O(1/k^2)$ among first-order optimization methods[69]. The problem demands more time and computational power for Chambolle-Pock with convergence rate of $O(1/k)$. With the heterogeneity weight included in the group sparsity term, Chambolle-Pock was unable to select 2-4 beams within a reasonable time span. The weight was excluded during beam selection to force convergence. Although CP convergence rate is not optimal, because of the non-convexity of the optimization problem, the CP plans

in some cases find a better local minimum and provide superior dosimetry compared to FISTA. The superior dosimetry can be attributed to effectively higher OAR RBE priority in CP without the heterogeneity index term. CP on average selects two more beams than FISTA plans, which may also explain the differences in results. Previous studies have shown improvement in dosimetry with three-angle plans over two-angle plans but no advantage with four-angle plans over three-angle plans[86,87].

Further research should be conducted to optimize both physical dose robustness towards geometrical and range uncertainties, and RBE robustness towards biological model parameter uncertainties. Biologically robust optimization algorithms that have thus far been proposed mostly consider worst case optimization[88-90], which would increase the computational burden of our current framework by at least 10-fold. Our sensitivity based robust planning method was able to handle physical dose robustness of IMPT plans with minimal additional computational cost. Therefore, a future direction is to incorporate the biological uncertainties into sensitivity regularization.

2.1.5 Conclusion

We have developed a robust RBE-weighted beam orientation optimization method using direct reformulation of the McNamara phenomenological model. The proposed optimization framework markedly improved OAR RBE doses while maintaining similar physical dose distribution compared with the conventional method assuming a generic RBE value for all voxels.

2.2 Nonlinear McNamara RBE-weighted beam orientation optimization using splitting

2.2.1 Introduction

While the reformulated McNamara RBE optimization produces a remarkable protective effect on OAR structures, the calculated RBE values in those structures are particularly high, due to the removal of the square root from Equation 2-3. A high RBE value within the OAR would convince the optimizer that physical dose must be pushed even lower than necessary to meet the optimization criteria (total biological OAR dose under a maximum value m), which could compromise tumor coverage. The optimizer in the study described above was able to achieve optimal OAR sparing with little reduction in tumor homogeneity using the FISTA algorithm, assuming a constant RBE of 1.1 in the tumor. However, we strive to better preserve the biological accuracy of the McNamara model in all structures, including the tumor volume.

Direct biological dose optimization for proton therapy with RBE weighting can improve biological effectiveness but is computationally challenging due to nonlinear dose dependence. As seen in Equation 2-1, the McNamara model depends not only on physical proton dose, which is the optimization variable we are attempting to solve for, but also the LETd, which is itself a function of proton dose. With several dependencies on fluence map $\boldsymbol{x}$, the biological dose optimization is difficult to separate from the group sparsity-based beam

orientation optimization. The split-Bregman optimization strategy proposed here decouples the calculation of McNamara proton RBE from the BOO problem.

2.2.2 Methods

The McNamara RBE-weighted BOO can be solved using a split-Bregman[91,92] approach described in Appendix 6.3. First, the biological dose fidelity terms (included in block 1), solved by variable x, are separated from the beam-regulating group sparsity term (included in block 2), solved by variable z. Fluence map variables x and z are pre-defined as randomized vectors and an initial RBE vector is calculated from x. Then, the first block, which includes the biological dose fidelity terms plus an equality constraint loosely minimizing the difference between variable x and constant z is solved using FISTA. Optimization of the second block, which includes the group sparsity term plus an equality constraint minimizing the difference between variable z and constant x, is then performed with FISTA. The cycle repeats as the two blocks are alternately solved with periodic RBE re-calculation using the normoxic model or the hypoxia informed RBE model described above for dose weighting. The relationship between optimization variables x and z are controlled by weight coefficient μ in line 6. At first, μ is small ($<10^{-4}$) to get rid of beams that do not aid the fluence map in reaching the dosimetry goals. As $\mu \rightarrow \infty$, the solutions x and z should be the same. The major advantage of the splitting algorithm is its compatibility with complex RBE forms. It also maintains a balanced relationship between the dose fidelity and group sparsity terms throughout the optimization.

The same three bilateral HN cases were used for this study with the same candidate set. The split-Bregman method was first compared to FISTA, with both methods optimized with the constant RBE of 1.1 (Phys-SB compared with Phys-FISTA). Then, Phys-SB and the previously calculated LET-weighted BOO (LET-FISTA) were compared to the McNamara RBE-based split-Bregman method (McNam-SB). Once all optimizations were completed and fluence maps were obtained, final RBE dose (GyRBE) for each plan was calculated using Equation 2-3 and compared, this time assuming a fractionation of schedule of 1.7GyRBE x 30 fractions. With a lower dose per fraction, the impact of RBE becomes more apparent (since its value increases significantly above the value of 1.1), especially for OAR structures with a low alpha-beta ratio. The same structure weighting used in the prior study was used for this study. CTV HI, D95%, maximum RBE-dose, and OAR mean and maximum RBE-dose were evaluated along with worst-case statistics.

2.2.3 Results

2.2.3.1 Runtime and Selected Beams

For all three patients, the Phys-SB plans selected the same beams as Phys-FISTA in the previous study. This ensured that the group sparsity term was able to reach the same global minimum when the RBE values passed to the first block were unchanged. Figure 2-8 displays the three-dimensional representation of the beam angles selected for each plan using the IEC 61217 coordinate system.

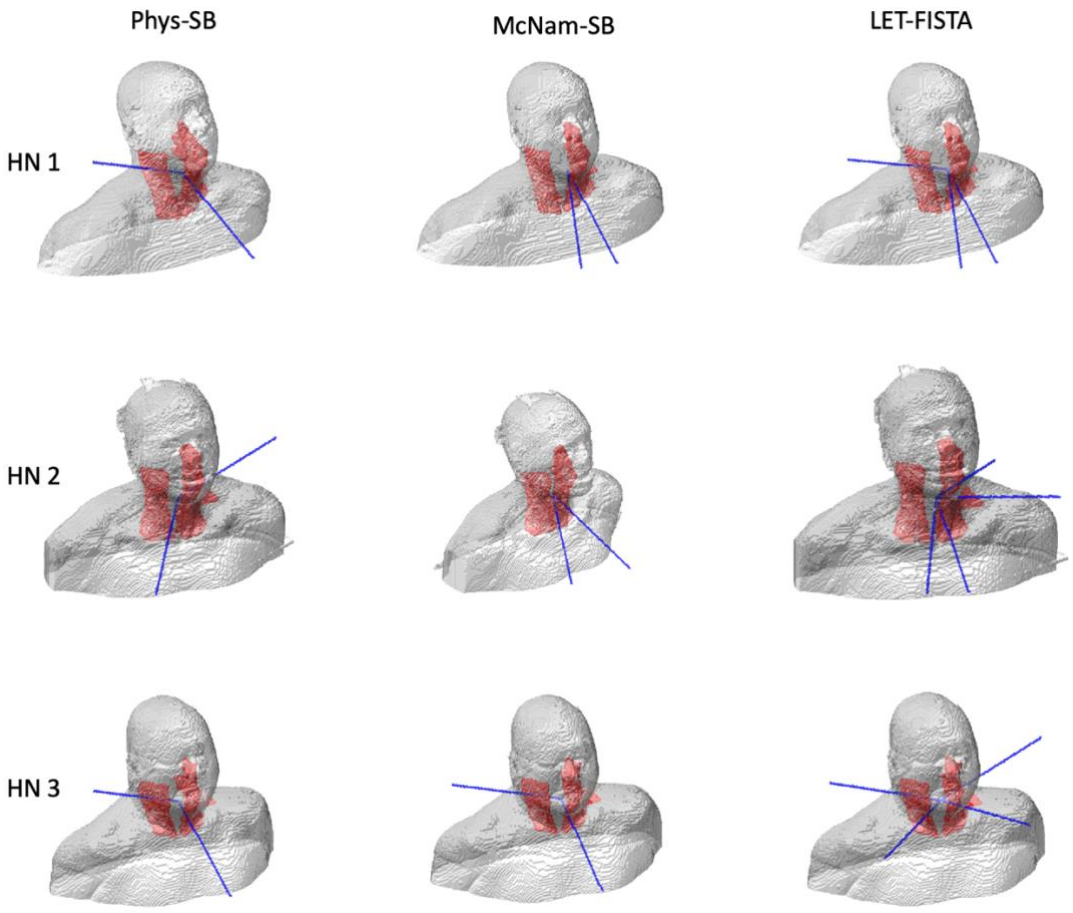

Figure 2-8. Beam angle comparison between Phys-SB, McNam-SB, and LET-FISTA (left to right) for all three patients. CTVs are shown in red and blue lines represent beams entering the patient.

Table 2-6 compares the runtimes of Phys-SB, McNam-SB, and LET-FISTA. The Phys-SB and McNam-SB plans took [26.1%, 46.8%] longer than FISTA to optimize since there were two separate blocks that needed to be optimized on each round. McNam-SB took 17.7% longer than Phys-SB to optimize since the optimization blocks for McNam-SB passed large RBE vectors between them, which was avoidable for a constant RBE. While typical physical dose optimization in the clinic is much faster, Phys-SB plans were still solved with the split-

Bregman approach, adding approximately 10-20 minutes extra time depending on plan complexity.

	Phys-SB	**McNam-SB**	**LET-FISTA**
HN 1	76	85	44
HN 2	101	119	93
HN 3	44	54	45

Table 2-6. SHBOO-FMO runtime in minutes using the split-Bregman technique for physical dose optimization (Phys-SB) and McNamara RBE optimization (McNam-SB) compared with runtime for LET-FISTA.

2.2.3.2 Dosimetric Comparison

Compared to Phys-SB, CTV [HI, Dmax, D95%, D98%] declined significantly with LET-FISTA on average by [11.0%, -2.6%, 28.2%, 180.6%] but only marginally with McNam-SB by [0.3%, 3.4%, 5.1%, 5.8%]. CTV statistics are shown in Table 2-7. LET-FISTA and McNam-SB both improved [Dmean, Dmax] in OARs on average compared to Phys-SB by [2.4%, 9.3%] and [16.8%, 12.8%], respectively. The values for each structure are shown in Table 2-8. The impact of RBE is shown in Figure 2-9. For OAR structures, wherever there is a high RBE (for LET-FISTA, the right submandibular gland, and for McNam-SB, the larynx and constrictors), both optimizers reduce physical dose significantly to compensate, resulting in superior sparing in that structure. In normal tissue structures with lower alpha-beta ratio, LET may be a good substitution for RBE. However, this is not the case for tumor structures with high alpha-beta ratio. There is a clear lack of homogeneity and many hot spots surrounding the CTVs for the LET-based plan.

	HI			Dmax			D95%		
Case	Phys-SB	LET-FISTA	McNam-SB	Phys-SB	LET-FISTA	McNam-SB	Phys-SB	LET-FISTA	McNam-SB
HN #1									
CTV54	**0.926**	0.855	0.912	63.1	**59.3**	64.0	57.4	49.1	**57.2**
CTV60	0.934	0.913	**0.939**	70.1	**63.5**	69.6	64.8	**57.0**	64.9
CTV63	0.936	0.916	**0.951**	70.7	**63.8**	70.1	**65.4**	57.4	66.2
HN #2									
CTV54	**0.933**	0.768	0.922	63.4	67.9	**63.3**	58.1	49.8	**57.4**
CTV60	**0.941**	0.821	0.938	**69.1**	**69.1**	**69.1**	**64.2**	54.4	**64.2**
HN #3									
CTV54	0.936	0.780	**0.937**	**62.7**	67.6	62.8	58.0	50.0	**57.9**
CTV60	**0.931**	0.792	0.917	**69.9**	71.1	70.8	64.4	54.5	**64.1**
CTV63	**0.943**	0.814	0.940	**70.6**	75.1	72.2	**66.2**	59.0	67.4

Table 2-7. Homogeneity index, maximum dose (Dmax), and D95% comparison between Phys-SB, McNam-SB, and LET-FISTA for all CTVs in each patient. Best values are denoted in bold.

	HN #1			HN #2			HN #3		
	Phys-SB	LET-FISTA	McNam-SB	Phys-SB	LET-FISTA	McNam-SB	Phys-SB	LET-FISTA	McNam-SB
Right subm. Gland									
Dmean	9.7	**7.5**	23.0	**16.3**	19.9	19.4	15.7	**8.2**	15.5
Dmax	54.2	**36.8**	53.9	**57.2**	62.6	57.9	60.0	**48.7**	59.0
Left Parotid									
Dmean	9.9	**5.3**	9.2	17.9	17.7	**15.1**	13.7	13.9	**13.7**

Dmax	66.0	**58.9**	68.7	**63.3**	65.7	64.3	70.3	**64.2**	72.2
Right Parotid									
Dmean	15.1	10.9	**4.2**	**10.2**	12.6	12.1	**18.9**	22.7	19.6
Dmax	60.0	**56.6**	63.2	**62.7**	64.5	65.5	**61.0**	73.8	62.7
Larynx									
Dmean	6.1	**2.0**	4.3	14.1	**7.8**	7.9	6.2	6.1	**5.6**
Dmax	54.3	**39.6**	46.2	73.4	**66.3**	73.3	49.9	**34.6**	49.3
Constrictors									
Dmean	3.8	3.3	**2.7**	12.1	9.7	**8.8**	11.9	18.8	**11.3**
Dmax	37.1	**36.3**	40.1	59.1	**58.4**	68.1	**63.6**	70.4	65.4
Esophagus	N/A	N/A	N/A						
Dmean				5.3	**0.4**	1.6	3.2	7.1	**2.7**
Dmax				48.9	**9.0**	25.4	32.3	40.6	**23.2**
Spinal Cord									
Dmean	3.7	3.3	**0.1**	5.9	0.2	**0.1**	**3.4**	9.5	4.5
Dmax	21.4	25.9	**0.1**	48.4	11.0	**7.0**	**39.6**	39.7	57.0

Table 2-8. OAR statistics comparison between three methods for all patient under. RBExDmean (Dmean for simplification) and RBExDmax (Dmax) are reported in GyRBE. Best values are denoted in bold.

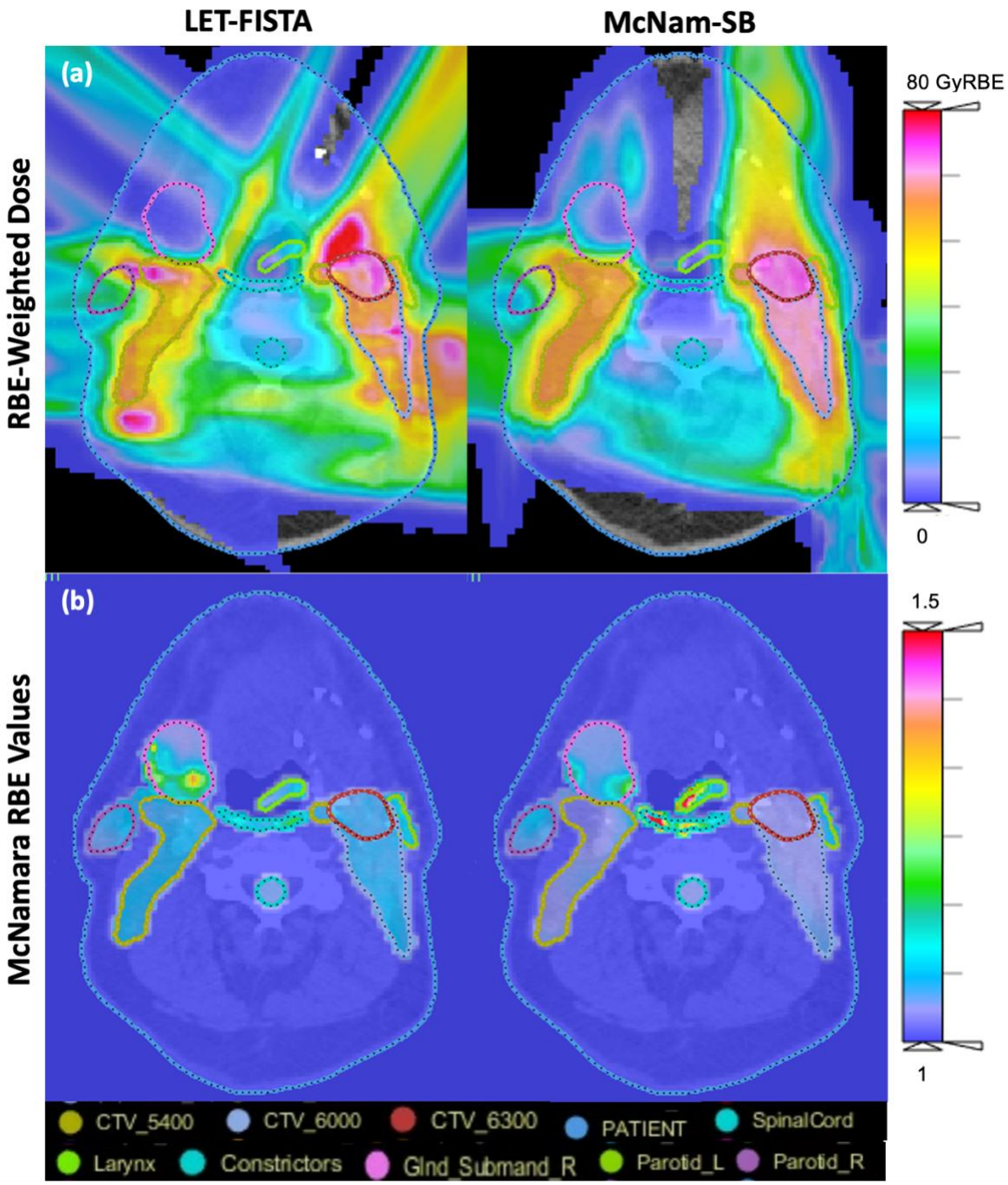

Figure 2-9. (a) McNamara RBE-weighted dose map (GyRBE) and (b) RBE values for HN 3 for an LET-based BOO plan solved with FISTA (left) and RBE-based BOO plan solved with split-Bregman methods (right).

*2.2.3.3 **Robustness***

As for robustness, Phys-SB and McNam-SB improved the worst-case CTV [HI, Dmax, D95%, D98%] compared to LET-FISTA by [33.7%, 25.2%, 18.3%, 20.4%] and [38.1%, 26.3%, 21.0%, 21.9%], respectively. McNam-SB improved the statistics by [3.6%, 1.3%, 2.4%, 1.8%] compared to Phys-SB. A DVH band plot for all three patients is shown in Figure 2-10, where the lack of robustness can be seen with LET-FISTA based on the width of the CTV band. Additionally, McNam-SB reduced the worst-case OAR Dmax on average by [17.8%, 6.8%] compared to [Phys-SB, LET-FISTA] but increased worst-case Dmean on average by [3.7%, 17.0%], with individual statistics shown in Figure 2-11.

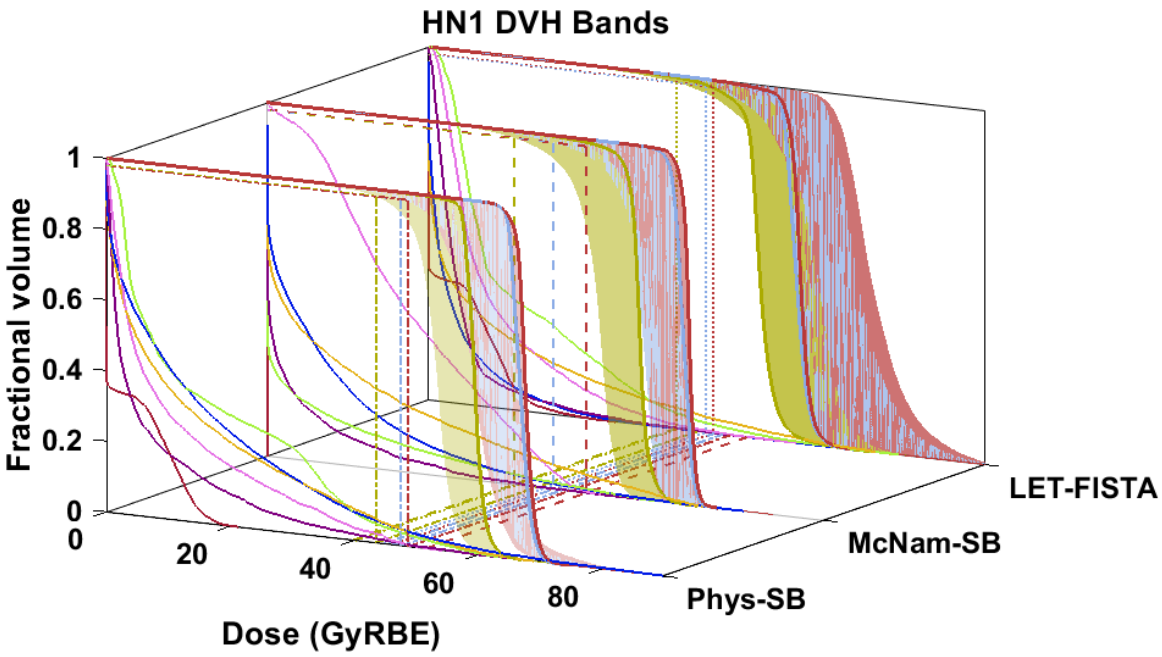

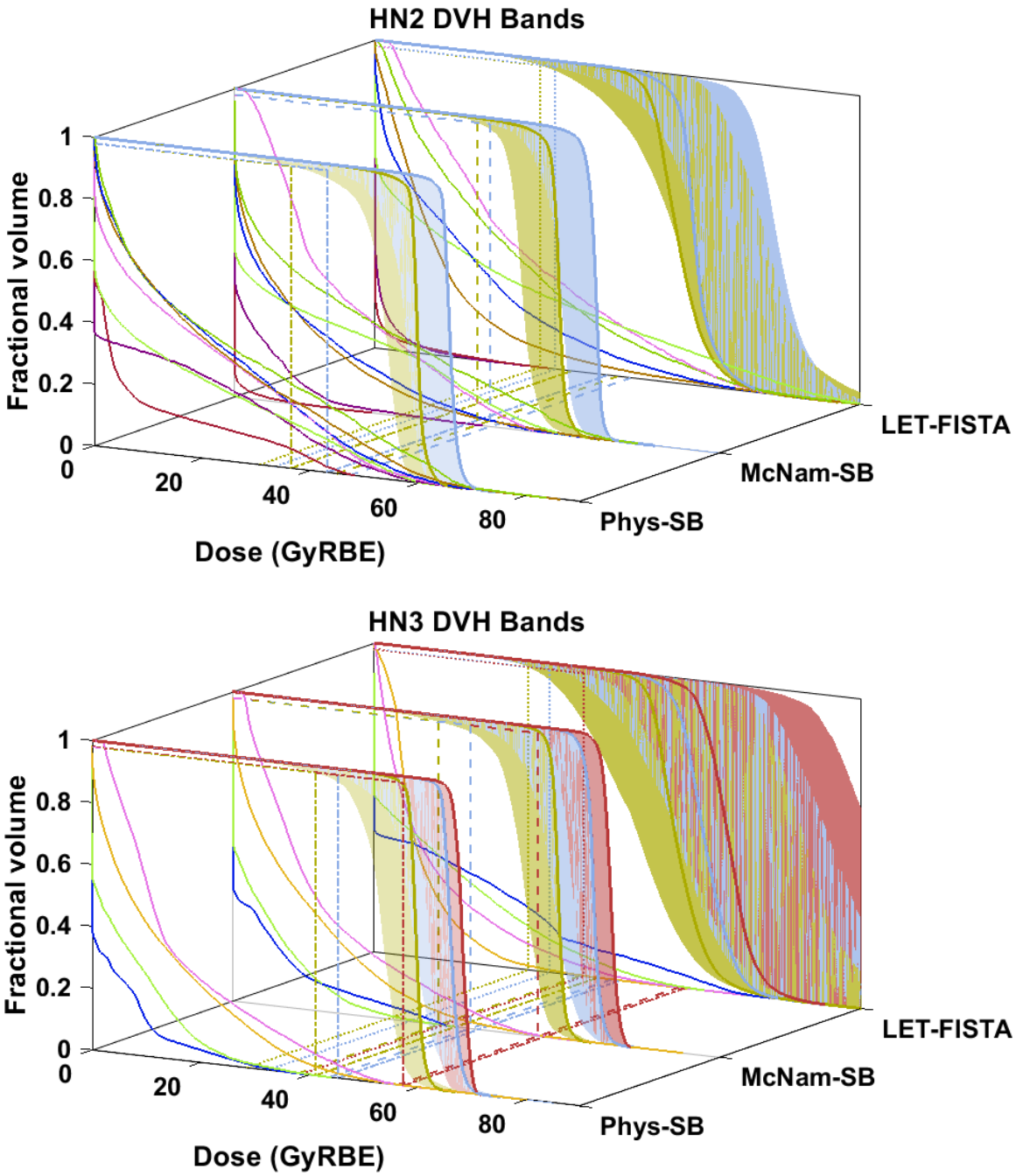

Figure 2-10. DVH band plots for the three patients, indicating the robustness of the beams chosen by Phys-SB, McNam-SB, and LET-FISTA. The worst D98% of each method is labeled by reference lines in the x-y plane.

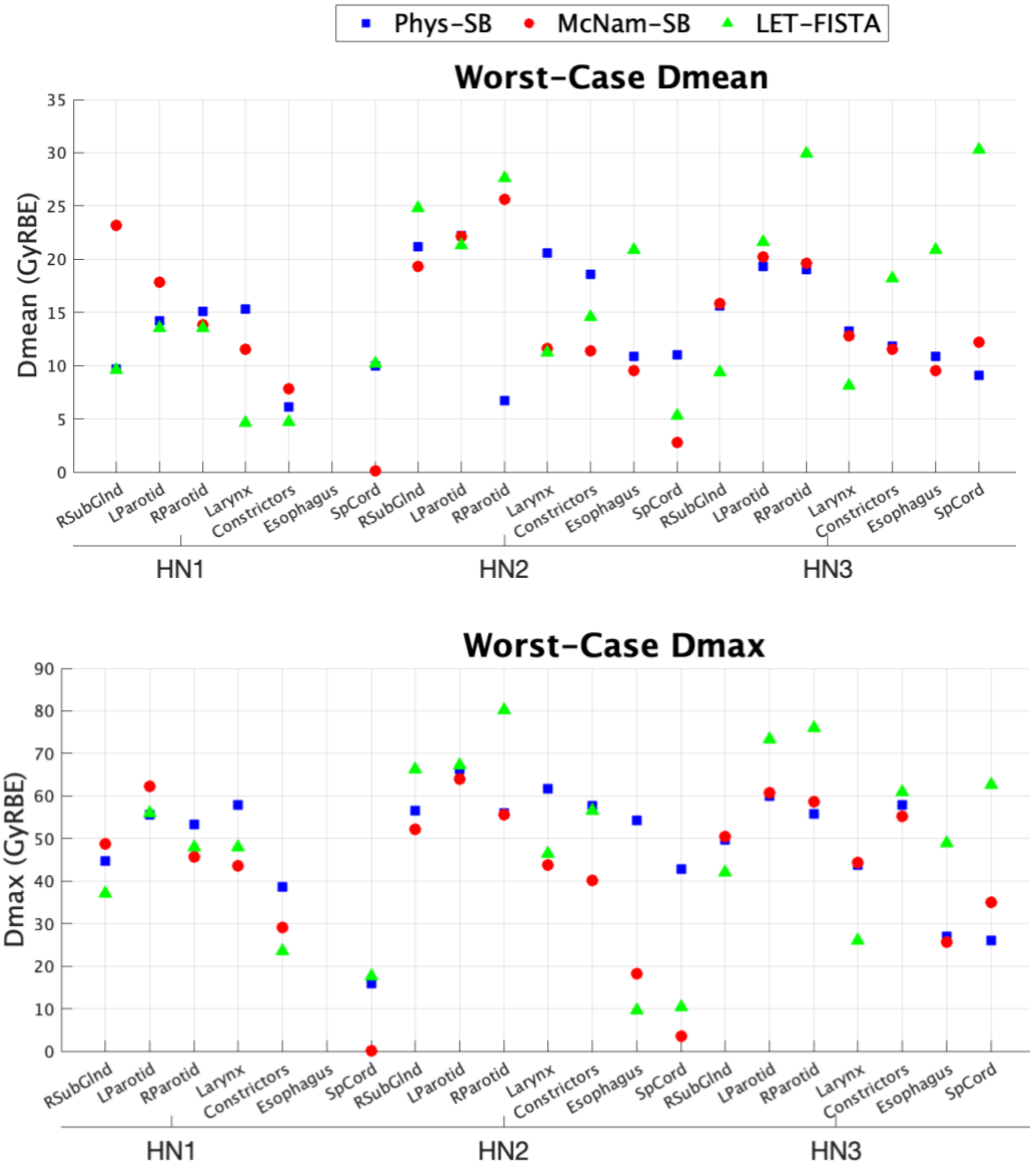

Figure 2-11. Worst-case OAR Dmean and Dmax (GyRBE) comparison between the three methods for all patients.

2.2.4 Discussion

The major limitation of the splitting scheme is its high dependence on the number of iterations per block. Generally, the splitting scheme is robust in that, regardless of which starting vectors and RBE values are chosen, the optimization will select the same beams. However, if the number of iterations for the first block is too high (>30 iterations), especially towards the beginning of the optimization, it is likely that the problem will get trapped in a local minimum and struggle to find the global optimal solution. Several rounds of parameter tuning were required to match the results of Phys-FISTA to that of Phys-SB. Moreover, the group sparsity term in both FISTA and the second block of SB, which commands the beam selection, is reliant on the weighting parameter α_b. If α_b is too high, the algorithm could eliminate several beams in the same iteration, prohibiting interpretation of the differences between beam numbers, particularly in the 1-10 beam range. If α_b is too low, the algorithm would take hundreds of extra iterations to eliminate beams down to 4 or fewer, unnecessarily adding to optimization runtime. Particularly with the SB method, α_b needed to be increased during optimization to force the convergence within a reasonable time frame, which may or may not have affected the final outcome. Although not explicitly reported, this tuning step added substantial planning time (>1 hour), and could lead to inconsistencies dependent on the planner's experience.

With regards to the comparison of McNam-SB to LET-FISTA, we note that the LET-based optimization with final RBE-dose weighting automatically creates a disadvantage due to the change in variable. The results show that RBE and LET should not be used as a surrogate for the other. If one were to optimize and weight with LET, it's likely that the

dosimetry would be desirable on paper, but this bars us from seeing what the true biological effect is. While LET is a physical quantity that is easy to calculate, it does not represent a measurable biological endpoint within the patient.

2.2.5 Conclusion

The splitting scheme provides an alternative solution for performing proton beam selection without compromising RBE modelling accuracy. We have shown that BOO performed with McNamara RBE is superior in dosimetry and robustness compared to constant RBE optimization or LET substitution methods.

3 HYPOXIA-INFORMED BEAM ORIENTATION OPTIMIZATION FOR TUMOR DOSE MODELLING

3.1 Hypoxia-informed RBE-weighted beam orientation optimization

3.1.1 Introduction

The particle track structure, LET, RBE, and OER have all been modeled in various Monte Carlo packages[93-96]. Existing studies have been primarily focused on determining the values of RBE and OER but minimally on methods to incorporate the values into treatment plans to overcome hypoxia-related radioresistance[97]. Such a study in the context of a beam selection framework is noticeably missing. This is partly due to the difficulty of formulating hypoxia-informed RBE into a tractable optimization problem. Thus far, constant RBE, variable RBE and/or LET alone have informed the selection and orientation of spot-scanning proton beams. As previously stated, attempts to incorporate RBE into optimization has led to nonlinear and nonconvex optimization problems. Indirect or sequential optimization frameworks used previously do not promise convergence to the optimal solution. The additional hypoxia consideration further complicates the

optimization problem. Here, we address the optimization challenge in hypoxia-based planning by testing the splitting scheme that is compatible with general voxel-based RBE forms without reformulation or simplifying approximate linearization.

Identifying tumor oxygen levels in real-time is the second barrier to hypoxia-based planning. Non-invasive hypoxia imaging techniques currently include blood-oxygen-level-dependent (BOLD)-MRI, electron paramagnetic resonance (EPR) oximetry, and PET/CT-based imaging[98-100]. While BOLD may produce a high spatial resolution and contrast, there is a weak correlation between the signal response and pO_2,[101] which may be worsened by the perturbation of the local magnetic field in the region of interest[102]. Additionally, EPR imaging has a low spatial resolution for voxel-level treatment planning. In contrast, [^{18}F]-fluoromisonidazole (FMISO), [^{18}F]-pentafluorinated etanidazole (EF5), and [^{18}F]-fluoroazomycin arabinoside (FAZA) are notable agents used for the imaging of hypoxia and have shown high repeatability[102-104]. Using information from images such as the [^{18}F]-FMISO-PET/CT data, one can obtain a voxel-by-voxel mapping of partial oxygen pressure (pO_2). With the advent of new technologies, including biologically guided radiotherapy (BgRT)[105], hypoxia imaging using PET may be an ideal solution for the dose optimization proposed in this study.

The benefit of the BOO algorithm is its ability to choose beams with superior dosimetry than beams chosen manually in the clinic. Since we have shown that BOO responds well to biological information, this study extends the optimization to leverage partial oxygen pressure (pO_2) information and proton OER for enhanced hypoxic tumor treatment.

3.1.2 Methods

The following section describes the BOO problem with a dose fidelity term weighed by hypoxia-informed RBE values. This study aims to select beams from a candidate set that maximizes pO_2-informed RBE to the hypoxic tumor cells while improving normal tissue sparing.

3.1.2.1 Calculation of RBE using [^{18}F]-FMISO-PET Images

Generally, after a physical dose distribution has been determined, proton RBE vectors for each tumor volume or OAR structure may be constructed using the variable RBE model[106] below, derived from the linear-quadratic model, where α_x and b_x are photon radiosensitivity parameters and α_p and b_p are proton radiosensitivity parameters.

$$RBE(x) = \frac{1}{Ax}\left(\sqrt{\left(\frac{\alpha_x}{2\beta_x}\right)^2 + \frac{(\alpha_p Ax + \beta_p (Ax)^2)}{\beta_x}} - \frac{\alpha_x}{2\beta_x}\right)$$

Equation 3-1

As in the previous study, we set the photon alpha-beta ratio to general values of 3 in OARs and 10 in the tumor volumes, but these values may be updated with available data[107,108].

Proton parameters α_p and β_p have been modeled by several *in vitro* studies[48,51], including the study performed by McNamara et al, which simply replaces $\alpha_p = y_0 + \frac{y_1}{(\frac{\alpha_x}{\beta_x})}L$ and $\beta_p = \left(y_2 + y_3\sqrt{\frac{\alpha_x}{\beta_x}}L\right)^2$. Dose-averaged LET ($L$) is also computed analytically in matRad using tabulated primary proton LET values as a function of depth in water. The model

changes based on oxygenation conditions. To model hypoxia-informed proton RBE as a metric of radioeffectiveness in each voxel, relative to photon irradiation in normoxic conditions, we calculate hypoxic proton alpha and beta values,

$$\alpha_{p,h} = \frac{\alpha_p(L, p_a)}{OER(L, p_h)}$$

Equation 3-2

$$\beta_{p,h} = \frac{\beta_p(p_a)}{OER^2(L, p_h)}$$

Equation 3-3

where OER is calculated as a function of L and normoxic and hypoxic partial oxygen pressure (p_a and p_h) using the following set of equations.

$$OER(L, p_h) = \frac{\sqrt{\alpha_p^2(L,p_h) - 4\beta_p(p_h)\ln(S)} - \alpha_p(L,p_h)}{\sqrt{\alpha_p^2(L,p_a) - 4\beta_p(p_a)\ln(S)} - \alpha_p(L,p_a)} \times \frac{\beta_p(p_a)}{\beta_p(p_h)}$$

Equation 3-4

$$\alpha_p(L, p_*) = \frac{(c_1 + c_2 L)p_* + (c_3 + c_4 L)K}{p_* + K}$$

Equation 3-5

$$\sqrt{\beta_p(p_*)} = \frac{c_5 p_* + c_6 K}{p_* + K}$$

Equation 3-6

Equations 3-5 and 3-6 use the Wenzl and Wilkens model fitted to proton data[16] with a survival fraction S of 10%, with parameters $c_1 = 0.10\ Gy^{-1}$, $c_2 = 0.0010\frac{\mu m}{Gy*keV}$, $c_3 = 0.010\ Gy^{-1}$, $c_4 = 0.0100\frac{\mu m}{Gy*keV}$, $c_5 = 0.765\ Gy^{-1}$, and $c_6 = 0.273\ Gy^{-1}$. The value K is set to a value of 3 mmHg. p_a is assumed to be a normoxic oxygen pressure of 30 mmHg. To obtain p_h values, we reference the PET images. First, we normalize the uptake values to values in blood. In previous head and neck cancer patients, after 3.7 MBq/kg injections of [^{18}F]-FMISO were delivered intravenously, the hypoxia threshold was defined as a tissue to blood uptake ratio of >=1.4 at 120-160 post-injection[109]. For our study, we use the same uptake threshold to define our hypoxic region within the clinical target volume (HypCTV), corresponding to a pO_2 value of <=2.5 mmHg. Then, a nonlinear least square curve, described in Equation 3-7, is used to convert the normalized uptake values to pO_2.

$$pO2 = \frac{C(A - Uptake)}{B - (A - Uptake)}$$

Equation 3-7

The curve fitting to roughly determine A, B, and C is based on points including the hypoxic threshold and reported pO_2 values of 29.2 mmHg in the muscle and 33.8 mmHg in the normal brain[110]. Detailed [^{18}F]-FMISO uptake data may be used in the future to provide this conversion[111], but here, we focus the study on the mathematical approach detailed below.

3.1.2.2 Plan Evaluations

Three glioblastoma patients with [^{18}F]-FMISO PET/CT imaging were selected for the study. After registration of earlier MR scans to the patient's treatment planning CT scan,

GTV and CTV regions, along with OARs including optic apparatus, lobes, and brainstem, were segmented by a single radiation oncologist according to EORTC guidelines[112]. The MRI and PET/CT acquisitions were 1, 0, and 11 days apart for the three patients. Uptake values from the pre-operative PET images were normalized and then converted to pO_2 values as described above. Figure 3-1 (a-b) shows the PET scan of one patient with its corresponding pO_2 map. pO_2 values under the hypoxic threshold within the CTV were segmented for the purpose of evaluation and labelled as the hypoxic region (HypCTV).

Robust group sparsity-based beam orientation optimization was performed using scanning spots covering the CTV as the optimization target plus a 5 mm margin, and the desired endpoint for the optimizer was less than four IMPT beams. The candidate set included approximately 220 non-coplanar beams in the 4π space after excluding infeasible beams due to truncated CT segmentation below the neck or collision detection[71]. Analytical dose calculation was performed in matRad with longitudinal and lateral spot spacing of 3 mm and 5 mm, spot size ranging from 11.8 mm for 31.7 MeV to 5.4 mm for 236 MeV, and a voxel resolution of 2.5 x 2.5 x 2.5 mm^3. The prescription dose, target volume, and the average number of spots per beam for each patient are shown in Table 3-1. Three fractionation schedules with a biologically equivalent dose (BED) of 60 GyRBE were tested for all RBE calculations: 1.7 GyRBE x 30 fractions, 4.2 GyRBE x 10 fractions, and 6.2 GyRBE x 6 fractions.

Case	Prescription BED (GyRBE)	CTV volume (cc)	Average spots per beam
Case 1	60	442	12,895

Case 2	60	447	13,908
Case 3	60	169	6,204

Table 3-1. CTV volumes with prescription doses and the average number of spots per beam for each patient.

Three plans were created for each of the patients, using the following dose fidelity terms: 1) physical dose with a constant RBE of 1.1 (which is currently used in clinical settings[54]), 2) a normoxic RBE-weighted dose (RegRBE) and 3) a hypoxic RBE-based dose with pO_2 values derived from the PET images (HypRBE). To identify the beam angles, all plans were solved using the split-Bregman (SB) approach. Then, the spots from the beams selected were optimized separately during a fluence map optimization step, using the RBE values computed on the final iteration of the beam orientation optimization. After the fluence map optimization, the HypRBE-weighted doses were calculated from all three final spot fluences. The same structure weights were used across all plans for comparability. Figure 3-1 (c-e) shows the final physical dose distributions and Figure 3-1 (f-h) shows the final HypRBE-weighted dose maps of the cRBE, RegRBE, and HypRBE optimizations for one patient as an example of the workflow. The figure denotes the hypoxic CTV region (HypCTV) and correspondingly low HypRBE-weighted dose maps with cRBE and RegRBE optimizations.

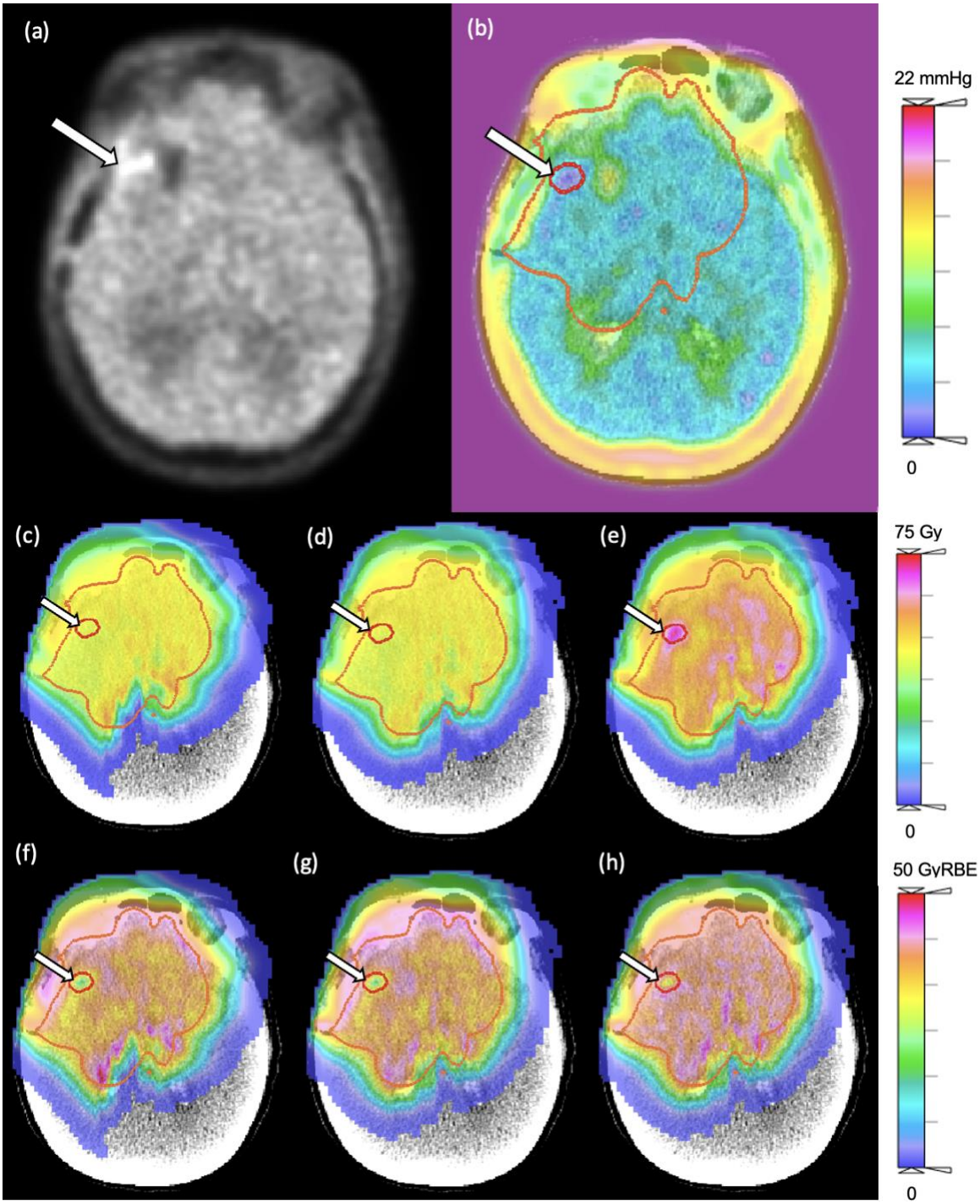

Figure 3-1. From Case 1, (a) [^{18}F]-FMISO-PET image; (b) partial oxygen pressure (mmHg) calculated from the PET normalized uptake values; unnormalized fluence map-optimized physical dose (Gy) using the (c) cRBE optimization method, (d) RegRBE optimization method, and (e) HypRBE optimization method; final HypRBE-weighted biological dose maps (GyRBE) for (f) cRBE, (g) RegRBE, and (h) HypRBE optimization. The CTV and HypCTV regions are outlined in orange and red, respectively.

Isotoxic dose normalization has been suggested for heterogenous glioblastoma multiforme tumors since a uniform dose escalation may increase toxicity to OARs. The hypoxia-informed RBE factor complicates this issue further. The alternative strategy respects the OAR constraints while allowing the CTV dose to be escalated to the highest achievable level[113,114]. All plans were normalized in relation to the maximal dose in the brainstem. CTV D95%, Dmax, and HI were calculated as an indicator of therapeutic index and consistency across voxels. Biological Dmean and Dmax along with a therapeutic index (TI)[115] were also calculated, which we define in Equation 3-8 as the ratio of generalized equivalent uniform doses from the CTV and each OAR. The generalized equivalent uniform dose (gEUD) quantifies the volume effect of each structure considered, and the phenomenological parameter "a" here represents the seriality of the organ. If $a \rightarrow 1$, gEUD→ Dmean. If $a \rightarrow +\infty$, gEUD→ Dmax. If $a \rightarrow -\infty$, gEUD→ Dmin[116]. The values of "a" and relative weights chosen for each structure are defined in Table 3-2. In Equation 3-8, n represents the number of fractions, N_{CTV} and N_{OAR} are the number of voxels in the CTV and OAR structures, and d is the dose per fraction. For the robustness analysis, we evaluated worst-case CTV HI, D95%, and Dmax and worst-case OAR Dmean, Dmax, and TI under twenty-one combinations of range and setup uncertainties simulated by scaling CT number by ±3% and shifting the beam isocenter ± 3 mm along three axes.

$$TI = \frac{gEUD_{CTV}}{gEUD_{OAR}} = \frac{n\left(\frac{1}{N_{CTV}}\sum_{i=1}^{N_{CTV}} d_i^{a_{CTV}}\right)^{\frac{1}{a_{CTV}}}}{n\left(\frac{1}{N_{OAR}}\sum_{i=1}^{N_{OAR}} d_i^{a_{OAR}}\right)^{\frac{1}{a_{OAR}}}}$$

Equation 3-8

Structure	**Volume Effect Parameter a**	**Relative Weight ω**
CTV	-10	1
Brainstem	20	1
Cochlea_R	1	0.1
Hippocampus_L	20	0.5
Hippocampus_R	20	0.7
Optic Chiasm	20	1
Optic Nerve L	20	0.7
Optic Nerve R	20	0.7
Temporal Lobes	20	0.3

Table 3-2. Volume effect parameter "$\boldsymbol{a}$" and relative optimization weight "$\boldsymbol{\omega}$" for all structures.

3.1.3 Results

3.1.3.1 Runtime and Selected Beams

Table 3-3 compares the runtimes of cRBE, RegRBE, and HypRBE. The RegRBE and HypRBE plans took longer than cRBE to optimize since the optimization blocks passed large RBE vectors between them, which was avoidable for a constant RBE. Generally, RegRBE and HypRBE plans took 13.3% and 33.3% longer, respectively, compared to cRBE.

Figure 3-2 displays the three-dimensional representation of the beam angles selected for each plan. We note that even if the same beams are selected, the HypRBE re-calculation post-BOO still greatly influences the fluence map optimization step.

	Case 1			**Case 2**			**Case 3**		
	30x	10x	6x	30x	10x	6x	30x	10x	6x
cRBE	27.5	30.0	27.7	56.1	57.6	56.5	29.5	31.2	23.7
RegRBE	39.2	39.1	39.4	57.8	60.9	56.2	29.6	27.1	25.7
HypRBE	42.3	42.6	41.6	73.9	74.1	66.4	34.7	35.0	34.3

Table 3-3. Total optimization runtime comparison (in minutes) between cRBE, RegRBE, and HypRBE for all patients and fractionation schedules.

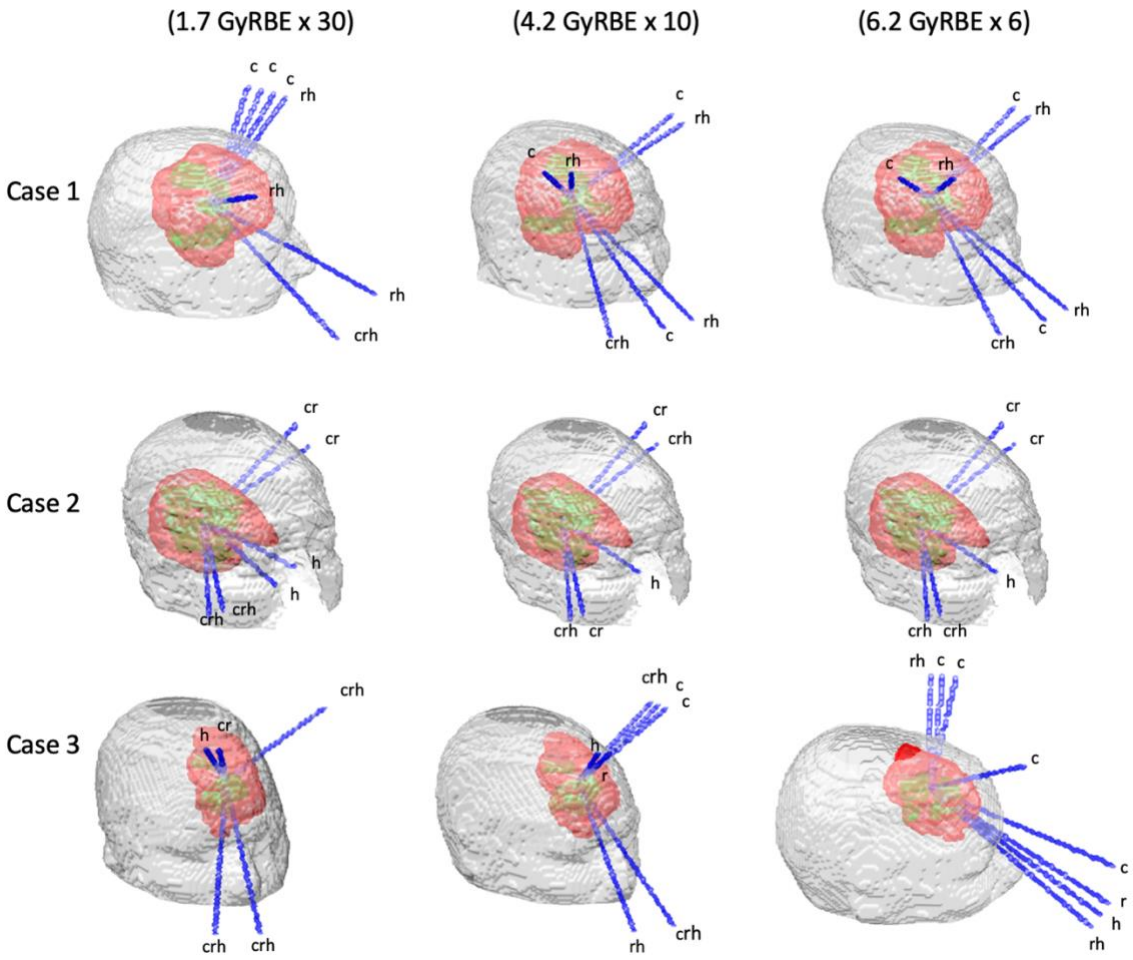

Figure 3-2. Three-dimensional representation of the optimized beam angles for glioblastoma patients with CTV structure shown in red and HypCTV shown in green. Blue lines labeled with "c", "r", and/or "h" represent beams chosen by cRBE, RegRBE, and HypRBE optimizations, respectively.

3.1.3.2 Dosimetry

Figure 3-3 shows CTV HI, D95%, and Dmax between all plans. Compared to cRBE plans and RegRBE plans, [HI, D95%, Dmax] averaged across all patients and fractionation schemes increased with HypRBE by [31.3%, 50.4%, 48.6%] and [31.8%, 23.8%, 27.1%]. Within the HypCTV region, [HI, D95%, Dmax] increased with HypRBE by [7.5%, 65.4%, 49.2%] and [6.5%, 31.6%, 20.3%]. As seen in Figure 3-1, the HypRBE-weighted dose cold

spot is largely eliminated with HypRBE optimization. Besides the improved dose homogeneity consistent with numerical values, the large drop in HypCTV DVH with cRBE and hypoxia-informed RegRBE optimization is compensated with RBE-weighted optimization.

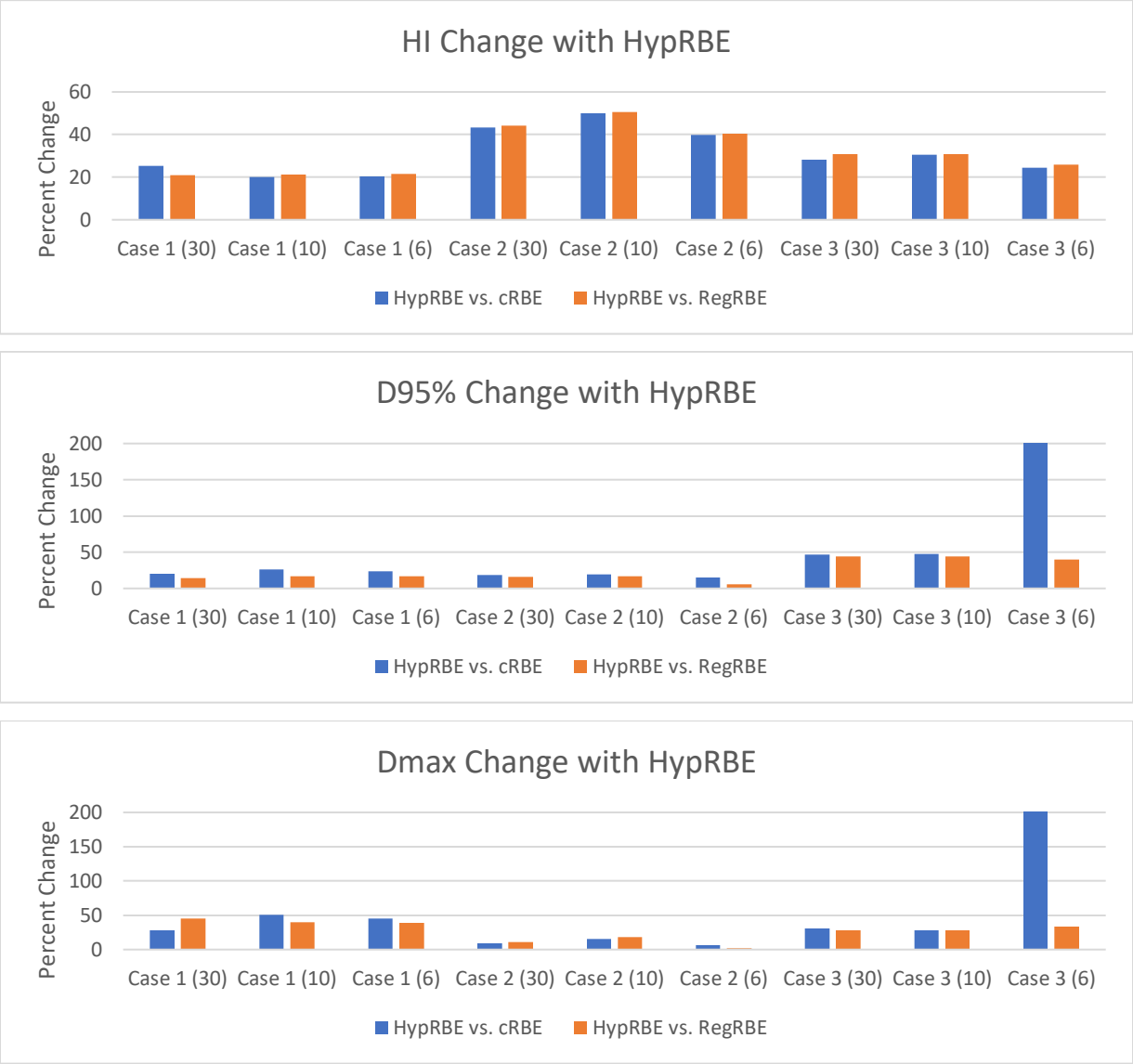

Figure 3-3. CTV HI, D95%, and Dmax percent change with HypRBE compared to cRBE (blue) and RegRBE (orange) for all plans. Higher HI and higher Dmax and D95% each represent a consistent spread of dose across the tumor with a larger therapeutic ratio.

The therapeutic index (TI) was calculated to characterize the difference in dose between each OAR and the CTV for ease of comparison. While OAR dose may increase with CTV dose escalation, the therapeutic window may still widen with HypRBE optimization. Figure 3-4 displays OAR biological Dmean and Dmax and TI for the 1.7 GyRBE x 30 fraction plans (the most difficult fractionation schedule to optimize) for all three patients after HypRBE re-calculation. Compared to cRBE, average biological [Dmean, Dmax] across all plans decreased with HypRBE optimization by [0.3%, 0.2%] in the brainstem, [4.5%, 0.5%] in the right cochlea, and [17.6%, 17.4%] in the left hippocampus, and [-0.8%, 7.5%] in the right hippocampus, but increased by [12.8%, 24.1%] in the chiasm, [34.9%, 20.0%] in the left optic nerve, [13.7%, 61.9%] in the right optic nerve, and [24.4%, 24.6%] in temporal lobes. Compared to [cRBE, RegRBE], average TI across all plans in the brainstem decreased by [7.7%, 8.3%], the right cochlea increased by [26.6%, 22.9%], the left and right hippocampus increased by [47.1%, 42.5%] and [12.4%, 12.4%], the optic chiasm increased by [11.4%, 11.4%], the left and right optic nerves increased by [80.1%, 78.9%] and [8.1%, 7.9%], and the temporal lobe increased by [14.6%, 10.1%] with HypRBE. Between fractionation schedules, from [30 to 10, 10 to 6] fractions, averaged across RBE models, CTV HI changed by [0.7%, -1.4%], CTV D95% by [-3.4%, 6.2%], Dmax by [-3.1%, 6.9%], and average OAR TI increased by [5.5%, 3.4%]. We hypothesize that the 6 fraction plans are able to achieve optimal tumor coverage and better OAR sparing since the RBE values do not change dramatically with doses near 6.2 GyRBE, whereas with lower doses per fraction, we see larger RBE changes.

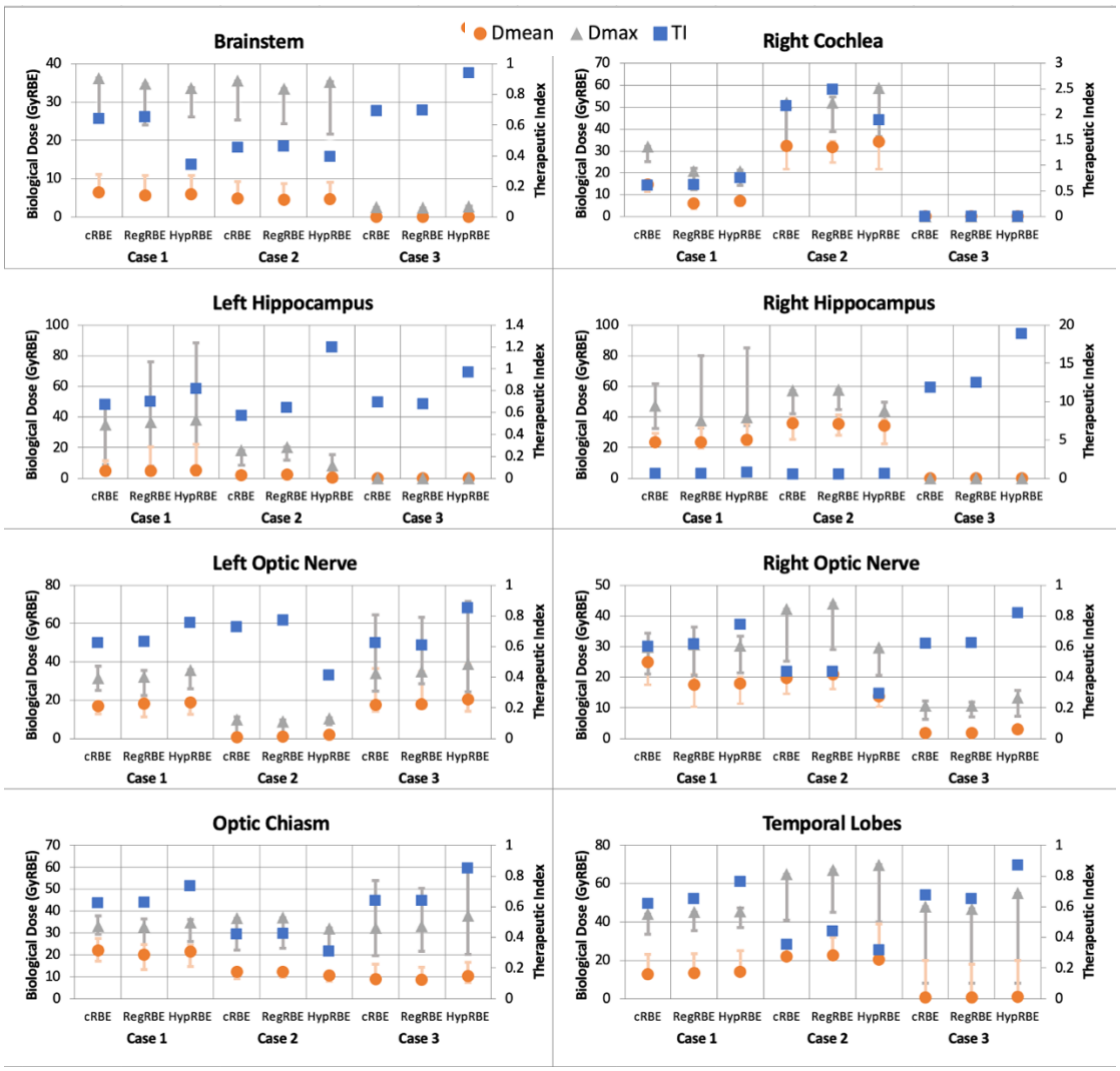

Figure 3-4. OAR mean and maximum biological dose (GyRBE) and therapeutic indices (TI) after isotoxicity normalization across cases for the 30-fraction schedule. Lower OAR dose is ideal, but a higher TI indicates a wider separation between tumor and OAR dose. The upper and lower error bars on mean and maximum biological doses represent the worst and best-case scenario statistics, respectively.

Fluence maps optimized without any hypoxia information (i.e., using either cRBE or RegRBE) cannot fully encompass patient tumor characteristics. The final LET maps show significant differences in addition to the final hypoxia-informed RBE values. The LET values were calculated using the dose-averaged LET definition from the final fluence map. Figure 3-5 shows the LET maps for all three optimization methods for Case 1. Across all patients

and fractionation schemes, [cRBE, RegRBE, HypRBE] optimizations in the CTV attain average mean and maximum LET values of [2.12, 2.14, 2.19] and [7.13, 7.38, 8.76] keV/μm. While a higher LET is commonly associated with a smaller OER (i.e., a ratio of normoxic to hypoxic RBE closer to 1), we show that the physical dose could either increase or decrease OER. As shown in Figure 3-6, plotting the McNamara RBE formula as a function of LET for a range of dose values suggests that the OER is highest for proton LET up to 8 keV/μm, above which it then decreases for doses higher than 3 Gy. Since the LET values achieved across the tumor are generally lower than or just meeting the 8 keV/μm threshold, the elevated LET across the tumor region after HypRBE optimization is consistent with the larger difference in normoxic and hypoxic RBE values.

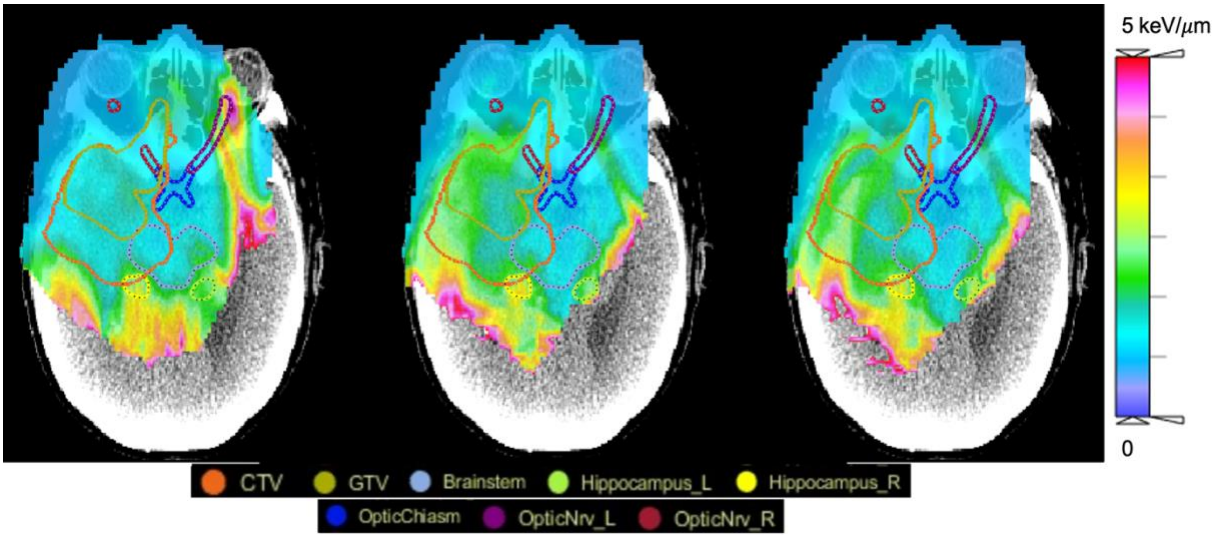

Figure 3-5. Dose-averaged LET distribution for (left to right) cRBE, RegRBE, and HypRBE optimizations for Case 1 (1.7 GyRBE x 30).

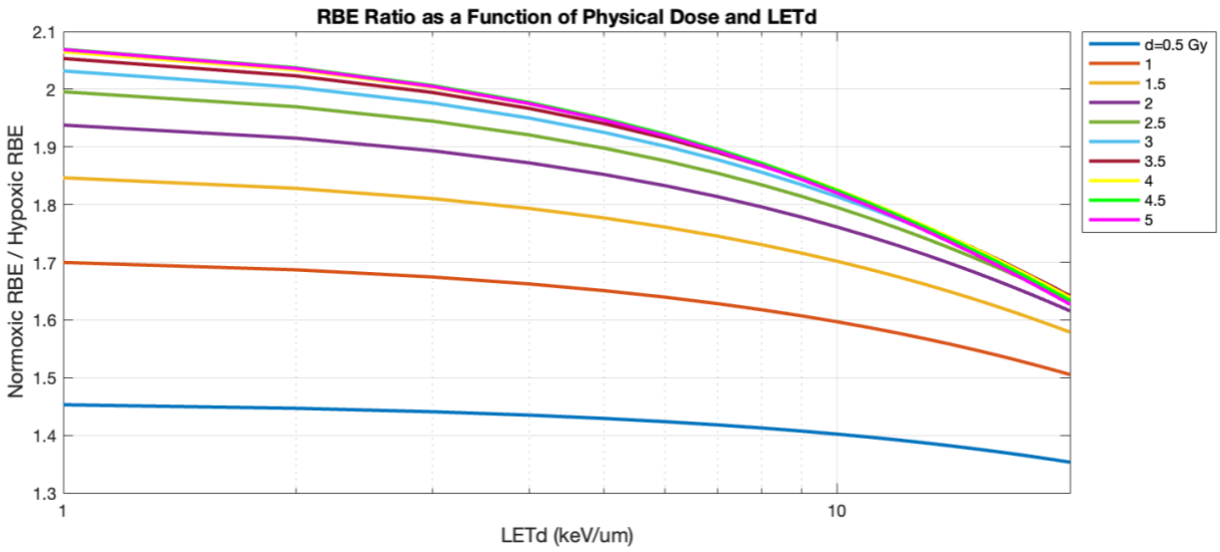

Figure 3-6. Ratio of normoxic and hypoxic McNamara RBE values as a function of proton LET (keV/µm) and proton physical dose (Gy). The ratio generally increases with increasing dose, but decreases with high LET greater than 8 keV/µm.

3.1.3.3 Robustness

Compared to cRBE plans and RegRBE plans, the worst-case scenario [HI, D95%, Dmax] for the CTV averaged across all plans increased with HypRBE by [12.5%, 22.3%, 7.3%] and [14.7%, 2.1%, -8.9%]. However, HypRBE could not match the robustness of cRBE and RegRBE plans due to HypRBE's high physical dose and resulting higher sensitivity to setup uncertainties. This tradeoff between conformal dosimetry and robustness is consistent with previous studies on RBE-driven dose painting. Compared to cRBE, [RegRBE, HypRBE] changed worst-case biological Dmean in the brainstem by [-2.1%, -3.4%], in the right cochlea by [-5.1%, -3.2%], in the left and right hippocampus by [22.9%, 19.8%] and [-0.1%, -0.1%], in the optic chiasm by [18.2%, -17.0%], in the left and right optic nerves by [25.7%, 40.6%] and [11.5%, 26.0%], and in the temporal lobe by [36.5%,

47.2%]. Worst-case biological Dmax changed in the brainstem by [-5.6%, -8.5%], in the right cochlea by [-0.1%, -1.7%], in the left and right hippocampus by [11.5%, 7.4%] and [2.6%, 0.2%], in the optic chiasm by [24.4%, 28.4%], in the left and right optic nerves by [32.7%, 32.0%] and [57.0%, 86.9%], and in the temporal lobe by [46.2%, 51.0%]. Additionally, [RegRBE, HypRBE] decreased worst-case TI in the brainstem by [1.0%, -33.4%], in the right cochlea by [20.2%, -6.6%], in the left and right hippocampus by [-4.9%, -17.5%] and [13.7%, 5.1%], in the optic chiasm by [3.8%, -16.7%], in the left and right optic nerves by [0.5%, 9.4%] and [3.9%, -16.9%], and in the temporal lobe by [90.6%, 64.2%]. Figure 3-7 shows a DVH band plot for Case 1 as a representation of robustness. Due to hypoxia-informed RBE final dose weighting, we expect a large range of biological dose values within the tumor volume and therefore a wide DVH band for all plans. Hypoxia-based analysis, whether it is considered during optimization or not, is not inherently robust, but is informative for large, heterogenous tumors.

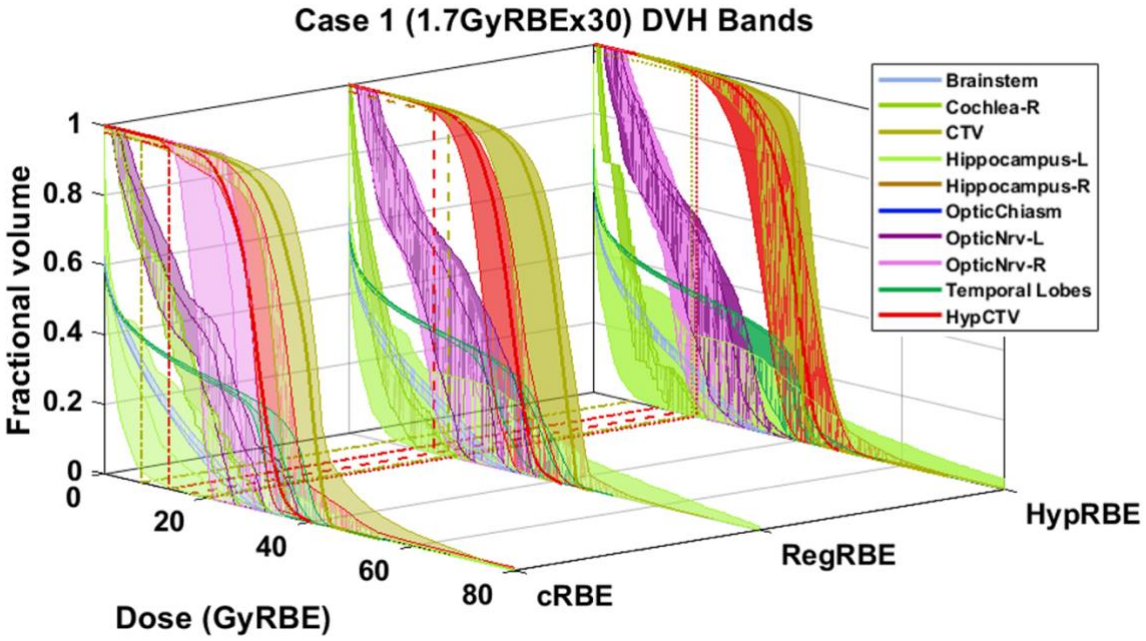

Figure 3-7. DVH band plot for Case 1, showing robustness comparison between cRBE, RegRBE, and HypRBE. CTV bands show the range between the lowest and highest possible biological doses (GyRBE) along with the nominal plan (solid line) and a projection onto the dose axis representing worst CTV D95% (dashed and dotted lines). All other solid lines represent the highest possible biological dose (GyRBE) to the OAR structures in the worst-case scenario.

3.1.4 Discussion

Radioresistance due to tumor hypoxia has been considered a critical barrier to achieving local control for many types of tumors[117-122], yet the potential of physically escalating the dose to the hypoxic volume is limited[123] due to normal tissue dose constraints and robustness concerns. The current study suggests the feasibility of achieving more potent biological effectiveness escalation to the tumor hypoxic subvolumes without increasing surrounding normal tissue dose or toxicity. To our best knowledge, we describe the first beam orientation optimization method incorporating hypoxia-informed RBE dose in a single IMPT treatment planning framework. Incorporating beam orientation in RBE optimization is vital as proton LET changes with depth and energy. Protons from different beam directions delivering the same physical dose to the same location have different RBE and hypoxia-informed RBE. Beyond beam selection, our optimization framework calculates proton RBE values reflecting oxygenation as a relevant metric of radioresistance in comparison to normoxic photon irradiation. Since cells with lower oxygen pressure are more radioresistant and have a lower RBE value[22], a greater physical dose is combined with optimized hypoxia RBE to hypoxic tumor cells as the result of optimization. We showed that the combination was effective in elevating the hypoxia tumor subvolume RBE

dose after considering OER, which led to a large increase in the optimized tumor RBE dose and dose homogeneity. We clarify that for some structures, the escalation of tumor dose did result in a slight increase in normal tissue dose. However, the associated increase in therapeutic index suggests that the plan may be normalized to below the tolerance doses of the OARs in question, with no resulting increase in normal tissue complication probability.

Our optimization framework is agnostic to imaging modalities that generate pO_2 maps. Brain [^{18}F]-FMISO-PET was chosen as the oxygenation imaging source due to its well-defined hypoxia threshold for uptake and partial oxygen pressure. The newly developed [^{18}F]-FAZA-PET tracer has also been tested as a hypoxia marker and has recently undergone clinical trials[104,124]. The FAZA tracer may facilitate future studies for OER optimization, but existing images and information on hypoxic threshold are limited. We caution that a conversion from uptake to pO_2 that results in a wider tissue oxygen disparity and/or higher threshold for hypoxia may further complicate HypRBE optimization by closing the initial therapeutic window.

Besides converting images to partial oxygen maps, the input image should provide sufficient resolution for voxel-level optimization. [^{18}F]-FMISO-PET measures uptake to the millimeter resolution, which is comparable with proton delivery resolution, with a spot size of ~3 mm in the lateral direction and ~5 mm in the longitudinal direction. Separate from the achievable imaging and dose delivery resolution, spatial oxygen distribution can vary at a significantly finer scale to μm[125]. The value of RBE, if it were calculated with finer resolution, could change drastically without voxel averaging. Therefore, spatial uncertainty

in OER and RBE can contribute to the overall uncertainties for further robustness analyses, especially for more spatially dynamic or irregularly shaped disease sites.

Besides spatial variation, the uncertainties in RBE propagated from combining PET/CT and MR scans, calculating pO_2 from uptake values and calculating OER from pO_2 certainly pose challenges to the optimization framework. As an example, a tumor voxel receiving a physical dose of 1.3 Gy and LET of 2 keV/μm would have ideal normoxic and hypoxic RBE values of 1.73 and 1.41. Assuming a 200% error in pO_2 value, a 10% error in all OER parameters, and the errors defined by the McNamara model, the normoxic and hypoxic RBE values could vary from 1.71-1.76 and 1.20-1.65, respectively, closing the initial therapeutic window on the lower end and opening it on the higher end. Further analysis is warranted to reduce imaging and modelling uncertainties with refined registration techniques, more data points for uptake conversion, and improved fitting methods for OER and variable RBE. Additionally, future study may minimize potential uncertainties within the cost function itself, similar to the heterogeneity index or sensitivity regularization terms. On a positive note, FMISO images show high reproducibility in uptake due to their reflection of diffusion-related chronic hypoxia, which is more stable compared to perfusion-related transient or acute hypoxia[126-128]. While [^{18}F]-FMISO-PET captures chronic hypoxia[129], complement transient hypoxia can be reflected in different imaging methods such as BOLD-MRI[130]. Incorporating both chronic and transient hypoxia in proton plan optimization would require an adaptive therapy approach, where, for each fraction, adjustments should be administered to the treatment plan after each imaging to ensure accurate dose delivery.

In practice, fractionation schedule, treatment duration, and dose rate all influence oxygenation levels. For V79 Chinese hamster cells and T1 human kidney cells under extreme hypoxia, when the dose per fraction was increased, OER changed up to 22% for low LET, and 4% for high LET particles[16]. OER is expected to increase while RBE decreases with higher doses per fraction. Our fractionation analysis reports that CTV Dmax and therapeutic ratio increase with higher doses, which aligns with the OER increase expectation.

matRad was used in the study for handling the beam orientation optimization problem but it was shown to overestimate LET values due to its failure to model secondary protons[57], which decreases the OER values in our study and may affect the beam selection and final RBE calculation. Without changing the optimization framework, Monte Carlo dose calculation using tools such as TOPAS-nBio[77] may be used to estimate the RBE more accurately.

One of the main takeaways of this study is the optimization aspect of complicated biologically-guided treatment planning. The split-Bregman method can simultaneously solve two separate problems (the RBE-weighted dose optimization and the beam orientation optimization). We caution that the SB framework is created for convex problems, and since our objective function includes a highly nonconvex group sparsity term, a global minimum may not be achieved. Manual tuning of the group sparsity term weight significantly affects the beam selection and final dose distribution, but this was held constant in our study for direct comparison between cRBE, RegRBE, and HypRBE plans. While our results also show the significantly increased complexity in evaluating

optimization using different RBE re-calculation methods, the results motivate the development of better optimization methods and analysis tools for better leveraging the high LET radiation to treat hypoxic tumors.

3.1.5 Conclusion

Tumor hypoxia is known to contribute to radioresistance. The higher RBE of protons for the hypoxic tumor volume is leveraged in the optimization study, which models the OER as a function of pO_2 derived from [^{18}F]-FMISO-PET images. The results show that tumor hypoxia-informed proton RBE optimization leads to substantially escalated biological effective dose to these radioresistant subvolumes without significantly increasing surrounding normal tissue dose.

4 Dose Rate Optimization with Beam Orientation Optimization for the Critical Region of Interest

4.1 Dose and Dose Rate Objectives in Bragg peak and shoot-through beam orientation optimization for FLASH proton therapy

4.1.1 Introduction

Recently, FLASH radiotherapy has attracted intense research and clinical interests due to its potential to reduce normal tissue toxicity while maintaining tumor cell killing, improving the therapeutic ratio[29]. The most appealing feature of FLASH is its ability to spare normal tissues without compromising tumor control, making it ideal for the tumor-normal tissue interface that mandates a high physical dose.

Delivering the ultra-high FLASH dose rates is a challenge, particularly so in clinical settings. More importantly, as a general principle, the radiobiological benefits of FLASH

should not be offset by physical dose degradation. Clinical linacs have been modified to operate in the photon mode without the X-ray converter for FLASH electron beams, which are suited for preclinical and clinical superficial treatments. X-ray FLASH radiotherapy would be more widely applicable to human tumors but achieving ultra-high dose rates and intensity-modulating such beams pose paramount engineering challenges. Several initiatives including PHASER[132] and ROAD[133] to overcome such challenges are in varying stages of development from engineering prototyping to conceptual designing. While electron and photon beams have shown FLASH effects for instantaneous dose rates between 10^4 and 10^9 Gy/s, and clinical proton accelerators only deliver dose rates in the low end of this range[134], proton beams have been validated for FLASH irradiation in the clinic and are readily available to treat deep-seated tumors[135]. Proton therapy systems operating with pencil beam scanning include isochronous cyclotrons and proton linacs[136], and are currently able to produce high instantaneous doses up to 800 Gy/s. Dose rate values reported for ProBeam systems (Varian Medical Systems, Palo Alto, CA) and Proteus proton therapy systems (Ion Beam Applications S.A, Louvain-La-Neuve, Belgium) were 240 and 200 Gy/s, respectively, for proton pencil beam scanning in clinical conditions[137]. However, the duration of the spot scanning process may decrease the mean dose rate to 1-2 Gy/min, which inhibits the study of the FLASH effect with IMPT over large irradiation fields[31,134]. Another consideration for FLASH therapy is the fractionation scheme of a typical IMPT plan, which may deliver small doses (~2 Gy) in multiple fractions (20-30)[138]. Studies have indicated that hypofractionation increases MU and thus dose rate, and that the combination of high doses and dose rates improve normal tissue sparing[139-142]. It is debated whether FLASH effects are observable only with doses above a certain threshold

(ranging up to 5-10 Gy), or whether the FLASH effect increases with dose[143]. However, high doses should still be delivered with caution since they may still worsen normal tissue dose before any FLASH sparing is observed[142]. While a full spatio-temporal report (including frequency and length of pulses, energy switching, beam switching, etc.) for proton FLASH delivery should be considered[144], we investigate the impact of a single parameter on dosimetry: the spot distribution.

To maintain FLASH dose rate, transmission or shoot-through beams have been suggested. Unlike IMPT, which places multiple Bragg peaks or spots within the target, shoot-through beams are single, high-energy beams with their Bragg peak placed behind the target, accelerating the delivery dose rate[145,146]. The depth-dose curves of shoot-through beams and Bragg peak beams are shown in Figure 4-1.

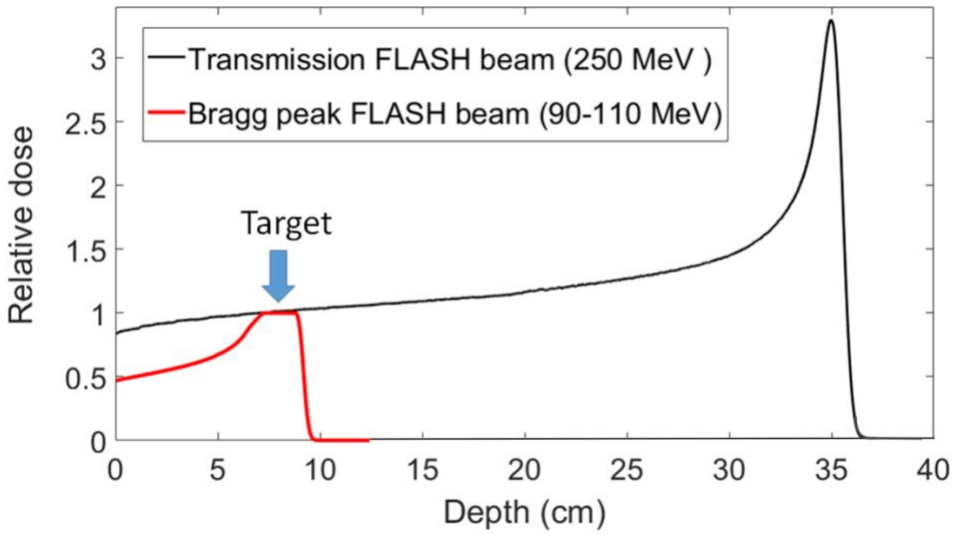

Figure 4-1. Depth-dose curve for a proton shoot-through or transmission beam vs. a Bragg peak beam.[147]

Studies have discussed using target-specific range compensators and a universal range shifter to adjust proton ranges to align with the distal edge of the tumor while still

using a single energy[148]. However, planning with single energies still may not be practical with challenging tumor geometries and may cause overdose in normal tissue[149,150].

Simultaneous dose and dose rate optimization (SDDRO) has been proposed for hybrid IMPT Bragg peak and shoot-through beams[140,149]. While SDDRO using Bragg peak beams was able to improve dose rate for IMPT, the SDDRO-joint method was able to improve both target conformality and dose rate by using both Bragg peak and shoot-through beams. With these current methods, beam angles were manually chosen without optimization, despite the implication of beam direction in the optimality of dose and dose rate for hybrid planning. To fully investigate the potential of these spot-placement methods, we consider the beam angle selection in the new joint optimization problem.

4.1.2 Methods

The dose and dose rate BOO problem is formulated to select scanning spots and/or shoot-through beams from a candidate set while minimizing dose to OARs, maintaining dose to the target, and increasing dose rate in the critical region surrounding the CTVs.

4.1.2.1 Dose Rate Objective for the Robust Scanning Spot Method

Because in proton therapy, high doses tend to spill to the normal tissue volume adjacent to the tumor, the same volume would benefit most from the FLASH effect. We select a region of interest (ROI) around the CTV structures, which covers the 10 mm 3D inner margin of the CTV outwards to the 10 mm outer margin of the CTV. To optimize the

dose rate for every voxel i in each ROI, we use the dose-averaged dose rate (DADR) definition proposed by Van de Water et al.[151],

$$\gamma_i = \frac{1}{\boldsymbol{d}_i} \sum_{j=1}^{N_x} \left(A_{ij}\boldsymbol{x}_j\right)\left(A_{ij}\boldsymbol{I}_j\right), i \leq N_d$$

Equation 4-1

which averages the dose rate $A_{ij}\boldsymbol{I}_j$ from all spots j (from all beams) and is weighted by the dose $A_{ij}\boldsymbol{x}_j$ to voxel i. The dose distribution $\boldsymbol{d}$ is determined by a physical dose calculation between dose influence matrix A and fluence map x. N_x is the number of proton spots from all beams and N_d is the number of spatial voxels. We choose DADR to define dose rate since it reports a 3D dose rate distribution for the whole plan and each voxel can be evaluated as receiving FLASH dose and dose rates based on defined thresholds. It is debated that DADR is an optimistic dose rate definition because it excludes the effective irradiation time, which begins when the cumulative dose rises above a certain threshold, and should include the time spent between spots. These concerns are addressed in the PBS dose rate definition proposed by Folkerts et al[152]. In their study, it was found that the total dose delivery plus pencil beam traversal time was 2.5 ms per spot for modern proton scanning systems[152]. To compensate for dead time between spot deliveries and to allow the linearity of the dose rate constraint described below, we replace beam intensity I with the value $\boldsymbol{x}$/t for each spot, where t=3 ms is assigned as the spot duration. We note that this spot duration is recorded within a monoenergetic layer. Energy-switching time for the Bragg peak method would add to effective irradiation time, but for the purposes of this mathematical framework, in which the total number of spots per layer and number of layers is meant to be reduced, the DADR definition is sufficient.

Defining B = A/t as a separate matrix, we expand our general BOO algorithm to include a lower and upper dose rate term,

$$minimize \underbrace{\sum_{r\in CTV} w_r\|A_r\boldsymbol{x}-\boldsymbol{l}_r\|_2^2}_{CTV\ term} + \underbrace{\sum_{s\in OAR} w_s\|(A_s\boldsymbol{x}-\boldsymbol{m}_s)_+\|_2^2}_{OAR\ term}$$

$$+ \underbrace{\sum_{q\in ROI} w_q\left\|(\gamma_0 * \boldsymbol{D} - (A_q.*B_q)(\boldsymbol{x}.*\boldsymbol{x}))_+\right\|_2^2}_{lower\ dose\ rate\ limit} + \underbrace{\sum_{q\in ROI} w_q\left\|((A_q.*B_q)(\boldsymbol{x}.*\boldsymbol{x}) - \boldsymbol{D}*\gamma_{max})_+\right\|_2^2}_{upper\ dose\ rate\ limit}$$

$$+ \underbrace{\eta\|\boldsymbol{x}\|_1}_{spot\ sparsity\ term} + \underbrace{\sum_{b\in\beta} h_b\alpha_b\|\boldsymbol{x}_b\|_2^{\frac{1}{2}}}_{group\ sparsity\ term} + \underbrace{\sum_{k\in\{\boldsymbol{u},\boldsymbol{v}\}} \lambda_k \boldsymbol{s}_k^T\boldsymbol{x}}_{sensitivity\ term}$$

Equation 4-2

The optimization variable $\boldsymbol{x}$ is a vector of the intensities of all scanning spots. The dose calculation matrix A contains the vectorized doses delivered to voxels in the patient from each spot. The first two terms are dose fidelity terms for the CTV and OAR structures, respectively. $\boldsymbol{l}_r$ is the prescription dose to the rth CTV and $\boldsymbol{m}_s$ is the prescribed maximal allowed dose to the sth OAR. The third and fourth terms represent minimization in deviation of DADR from $\gamma_0 = 40$ Gy/s and $\gamma_{max} = 150$ Gy/s, as lower and upper limits. The SDDRO objective function provided an upper bound constraint on proton spot weights to represent the highest beam intensity that the machine could produce[140]. With our formulation, an upper limit on dose rate is introduced voxel-by-voxel to penalize dose rate values greater than what a typical proton beam can produce (~200 Gy/s). The 150 Gy/s setting here is conservative; this value can be easily tuned according to machine specifications. $\boldsymbol{D}$ is a precalculated physical dose. Elementwise multiplication is shown between A and B, where the substitution of B imitates the dose rate. Weights w are the

structure-specific weighting parameters that emphasize the importance of different structures and terms. The fifth term provides sparsity regularization on the scanning spots to reduce the number of active spots and improve delivery efficiency and, therefore, dose rate, and η is its weighting parameter. The sixth term encourages most candidate beams to be zero, resulting in a small number of beams being selected. $\boldsymbol{x}_b$ is a vector representing the intensities of spots from candidate beam b, so $\boldsymbol{x}$ is the concatenation of all vectors $\boldsymbol{x}_b$ ($b \in \beta$). Hyperparameter α_b, defined as

$$\alpha_b = z\left(\frac{\left\|A_{CTV}^{b}\vec{1}\right\|_2}{n_b}\right)^{p/2}$$

Equation 4-3

, includes the dose calculation matrix A_{CTV}^{b} of the CTV divided by the number of candidate spots n_b in beam b, and z is a regularization parameter tuned higher to force convergence. To consider the robustness of this method against range and setup uncertainties, we add our previous sensitivity and heterogeneity-weighted formulation. Lateral heterogeneity index h_b for beam b encourages the selection of beams with less sensitivity to setup uncertainties. The last term accounts for range uncertainties in the beam direction (**u**) and perpendicular to the beam (**v**) by using longitudinal and lateral sensitivity vectors with a weighting parameter λ_k. FISTA is used to solve this non-differentiable problem.

4.1.2.2 The Addition of Shoot-Through Beams to the Candidate Set

Similar to SDDRO-joint, the following method takes advantage of both available candidate sets (Bragg peak and shoot-through).

$$minimize \underbrace{\sum_{r\in CTV} w_r \|A_r \boldsymbol{x} - \boldsymbol{l}_r\|_2^2}_{CTV\ term} + \underbrace{\sum_{s\in OAR} w_s \|(A_s \boldsymbol{x} - \boldsymbol{m}_s)_+\|_2^2}_{OAR\ term}$$

$$+ \underbrace{\sum_{q\in ROI} w_q \left\|(\gamma_0 * \boldsymbol{D} - (A_q .* B_q)(\boldsymbol{x} .* \boldsymbol{x}))_+\right\|_2^2}_{lower\ dose\ rate\ limit} + \underbrace{\sum_{q\in ROI} w_q \left\|((A_q .* B_q)(\boldsymbol{x} .* \boldsymbol{x}) - \boldsymbol{D} * \gamma_{max})_+\right\|_2^2}_{upper\ dose\ rate\ limit}$$

$$+ \underbrace{\eta \|\boldsymbol{x}\|_1}_{spot\ sparsity\ term} + \underbrace{\textstyle\sum_{b\in\beta} h_{b,BP} \alpha_{BP} \left\|\boldsymbol{x}_{BP,b}\right\|_2^{\frac{1}{2}}}_{group\ sparsity\ for\ BP} + \underbrace{\textstyle\sum_{b\in\beta} h_{b,ST} \alpha_{ST} \left\|\boldsymbol{x}_{ST,b}\right\|_2^{\frac{1}{2}}}_{group\ sparsity\ for\ ST} + \underbrace{\textstyle\sum_{k\in\{\boldsymbol{u},\boldsymbol{v}\}} \lambda_k \boldsymbol{s}_k^T \boldsymbol{x}}_{sensitivity\ term}$$

Equation 4-4

Dose matrix A and fluence map $\boldsymbol{x}$ in each term are concatenations $[A_{BP}\ A_{ST}]$ and $\begin{bmatrix}\boldsymbol{x}_{BP}\\ \boldsymbol{x}_{ST}\end{bmatrix}$. Multiplying these vectors gives the total dose from both sets of beams $A_{BP}\,\boldsymbol{x}_{BP} + A_{ST}\,\boldsymbol{x}_{ST}$. Hyperparameters α_{BP} and α_{ST} are tuned separately within the group sparsity terms to minimize the number of Bragg peak and shoot through beams from their respective candidate beam sets. Bragg peak beams are specifically chosen to cover the inner target area, while shoot-through beams are chosen to cover the tumor boundary. Separate heterogeneity indices are calculated for each group sparsity term.

4.1.2.3 Patient Evaluations

The proposed planning method was evaluated using the same three bilateral HN patients as used in Chapter 2. We note that the purpose of the evaluation is not to obtain clinically acceptable hypofractionated treatment protocols for these patients. We simply use the complexity of the head and neck cases to demonstrate the contrast in plan quality using different optimization frameworks. A 6 Gy fraction delivery with a proton arc shoot-through method may be required to achieve FLASH dose rates in the clinic[136], but here, a

single fraction is assumed for each plan to visualize the tradeoff between high normal tissue dose and the FLASH sparing effect.

For beam orientation optimization, we selected a subset of 220 non-coplanar beams from the total of 1162 evenly distributed beams in the 4π space with 6° spread after excluding infeasible beams due to collision and incomplete CT extension. The collision detection was performed based on the CAD model of the IBA Proteus Plus gantry with a PBS-dedicated nozzle, patient masks, and a scissor couch. A range shifter was assumed for superficial depths. The dose influence matrix A was calculated using matRad, describing the dose from the scanning spots covering the CTV and a 5 mm margin to voxels of resolution 2.5 x 2.5 x 2.5 mm^3. For the scanning spot method, lateral spot spacing was set to 5 mm, while energies were interpolated in the beam direction to obtain a layer spacing of 3 mm. For the shoot-through method, dose matrix A was generated with the 229 MeV proton energy only, creating a single layer with spots separated by 5 mm in the lateral direction. Robust optimization was performed using CTV as the target. The prescription dose, target volume, and the average number of spots per beam for each type of beam and for each patient are shown in Table 4-1.

Case		Prescription dose (Gy)	CTV volume (cc)	Average spots per BP beam	Average spots per ST beam
H&N 1	CTV54 CTV60 CTV63	54 60 63	141.29 160.89 68.00	10065	737
H&N 2	CTV54 CTV60	54 60	108.00 127.26	10077	697

H&N 3	CTV54	54	110.38	9433	604
	CTV60	60	98.94		
	CTV63	63	10.23		

Table 4-1. CTV volumes with prescription doses and average number of spots per Bragg peak and shoot-through beam for each patient.

We created four plans for each patient: 1) IMPT dose optimization using scanning spots without dose rate optimization (BP); 2) dose and dose rate optimization from a selection of scanning spots using spread-out Bragg peaks (BP-DR); 3) dose and dose rate optimization from only shoot-through beams (ST-DR); and 4) dose and dose rate optimization from a selection of both Bragg peak and shoot-through beams (BPST-DR). In terms of Equation 4-4, BP uses the CTV term, OAR term, the spot sparsity term, group sparsity term for BP, and the sensitivity term. BP-DR uses the first six terms and the sensitivity term. ST-DR uses the first five terms and the shoot-through group sparsity term, and BPST-DR method uses all terms. Note that the ST-DR method does not use a sensitivity term since range uncertainties should not affect the dose inside the patient. Similar structure weighting for each patient was used across plans for a fair comparison.

We normalized the plans to cover 95% of the CTV by the prescription dose. CTV homogeneity and maximum dose were evaluated. OAR Dmean and Dmax were also evaluated. The volume of ROIs surrounding each CTV as well as the volume of each OAR (%) receiving greater than 40 Gy/s ($V_{\gamma 0}$) was calculated as an evaluation of dose rate. We considered twenty-one worst-case scenarios in the robustness analysis, including combinations of range and setup uncertainties as follows: CT number was scaled by ± 3%

to simulate range uncertainties, and the beam isocenter was shifted by ± 3 mm along three axes to simulate setup uncertainties. We compared worst Dmax and D95% for each CTV and worst Dmean and Dmax for OARs among plans.

4.1.3 Results

4.1.3.1 Runtime and Selected Beams

Table 4-2 lists the average time per beam to calculate the dose data for the Bragg peak and shoot-through methods, along with the total optimization runtime for BP, BP-DR, ST-DR, and BPST-DR for each patient. The BP-DR and BPST-DR plans increased the total optimization time on average by a multiple of 4.4 and 7.3, respectively, compared to the BP plans. In comparison, the ST-DR plans saved about 1-4 minutes per plan.

	Calculation time (min)			Total optimization runtime (min)		
Case	BP Dose	ST Dose	BP	BP-DR	ST-DR	BPST-DR
H&N 1	19	11	6	45	5	52
H&N 2	24	9	7	28	5	47
H&N 3	16	7	7	11	3	46

Table 4-2. Dose calculation time and runtime of each optimization method for the tested patients

The number of beams for each case is listed in Table 4-3. Figure 4-2 shows the 3D rendering of beam angles. The gantry and couch angles follow IEC 61217 coordinate conventions. The percentage of active spots remaining after optimization with BOO is listed

in Table 4-4. The dose rate plans, [BP-DR, ST-DR, BPST-DR] were able to further reduce the number of active spots on average by [2.5%, 25.2%, 9.0%] compared to BP.

	Number of (Bragg peak, shoot-through) Beams Selected			
Case	BP	BP-DR	ST-DR	BPST-DR
H&N 1	(3,0)	(4,0)	(0,9)	(4,1)
H&N 2	(3,0)	(4,0)	(0,12)	(4,1)
H&N 3	(3,0)	(3,0)	(0,13)	(4,1)

Table 4-3. Beam numbers selected for each patient as a result of BOO.

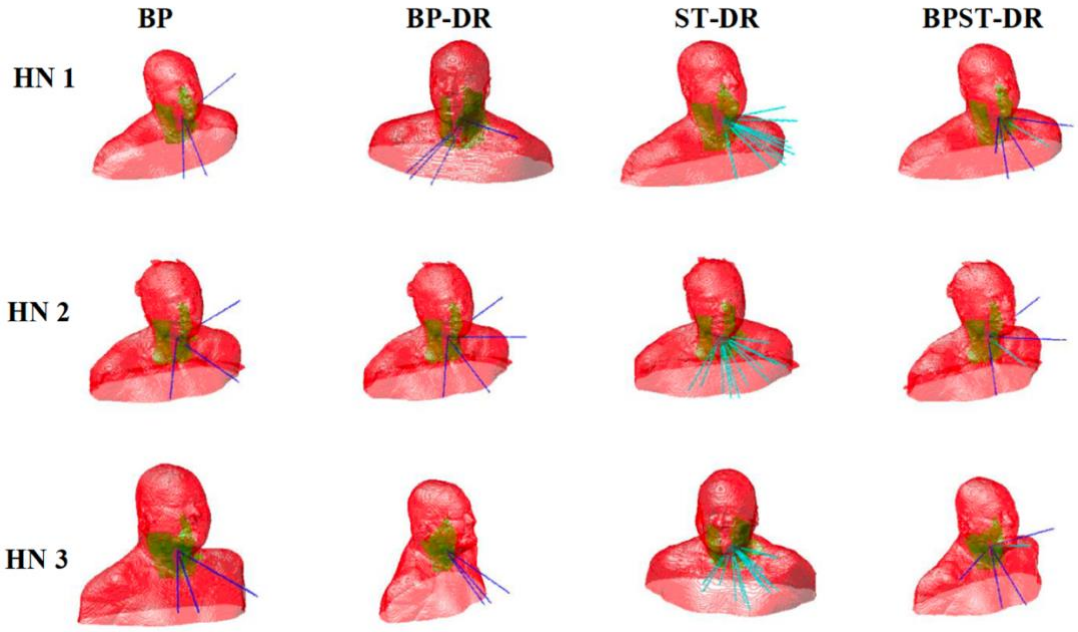

Figure 4-2. Optimized beam angles for BP, BP-DR, ST-DR, and BPST-DR (left to right). CTVs are displayed in green, dark blue lines represent incident Bragg peak beams, and light blue lines represent incident shoot-through beams.

	Active Spots After Beam Selection			
Case	BP	BP-DR	ST-DR	BPST-DR

H&N 1	31.3%	30.9%	4.3%	17.4%
H&N 2	25.6%	20.0%	3.0%	17.9%
H&N 3	28.0%	26.5%	2.0%	22.5%

Table 4-4. Percentage of candidate spots that are active for each plan after BOO.

4.1.3.2 CTV Dose and Dose Rate Statistics

The dosimetry and dose rate are compared in Figures 4-3 and 4-4 with consistent scales. Compared to BP plans, the average CTV HI and maximum dose are most improved by BPST-DR plans by 5.8% and 6.0% of the prescription dose. BP-DR and ST-DR plans were unable to match this CTV coverage, resulting in an average decline in [HI, Dmax] of [2.2%, 2.2%] and [28.4%, 22.5%], respectively, compared to BP. In terms of dose rate, the improvement in the volume of each ROI receiving more than 40 Gy/s was remarkable for all dose rate plans. BP-DR, ST-DR, and BPST-DR were able to significantly improve $V_{\gamma 0}$ by 89.7%, 98.8%, and 90.8% of the original BP dose rate. A dose-rate volume histogram (DRVH) is shown for ROIs in Figure 4-5. All CTV statistics are shown in Table 4-5.

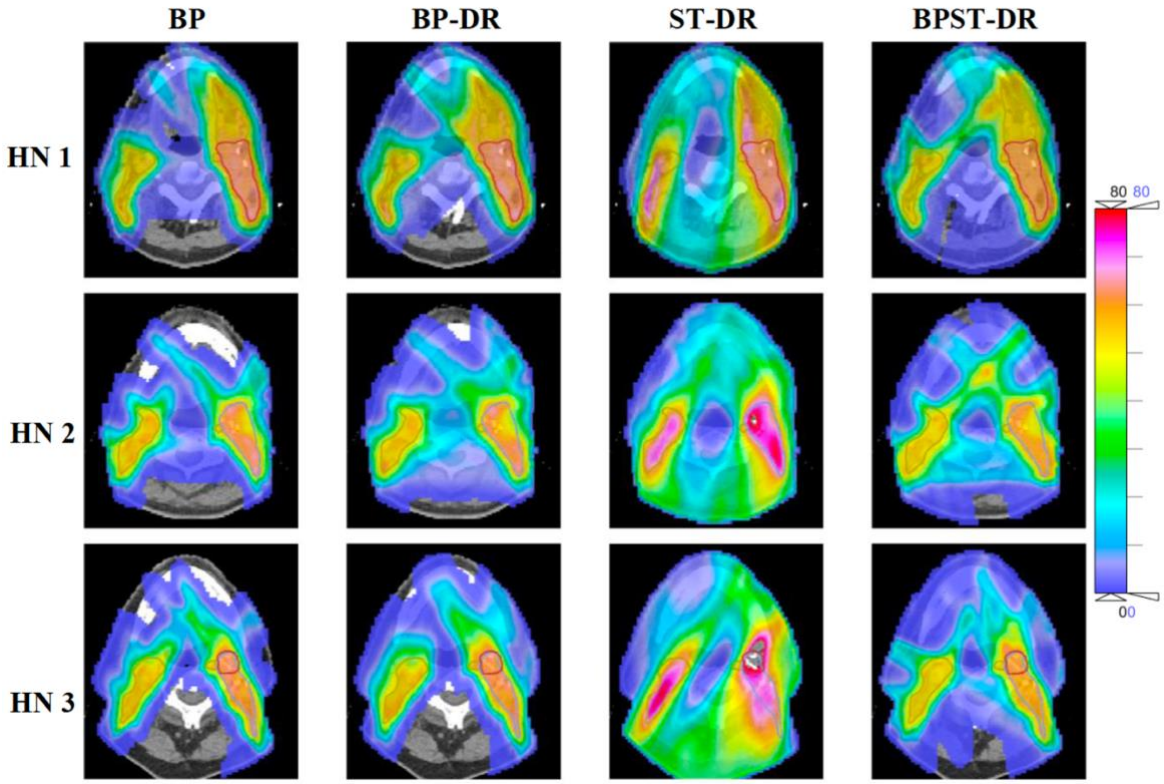

Figure 4-3. Dose (Gy) comparison between all four plans for each head-and-neck patient

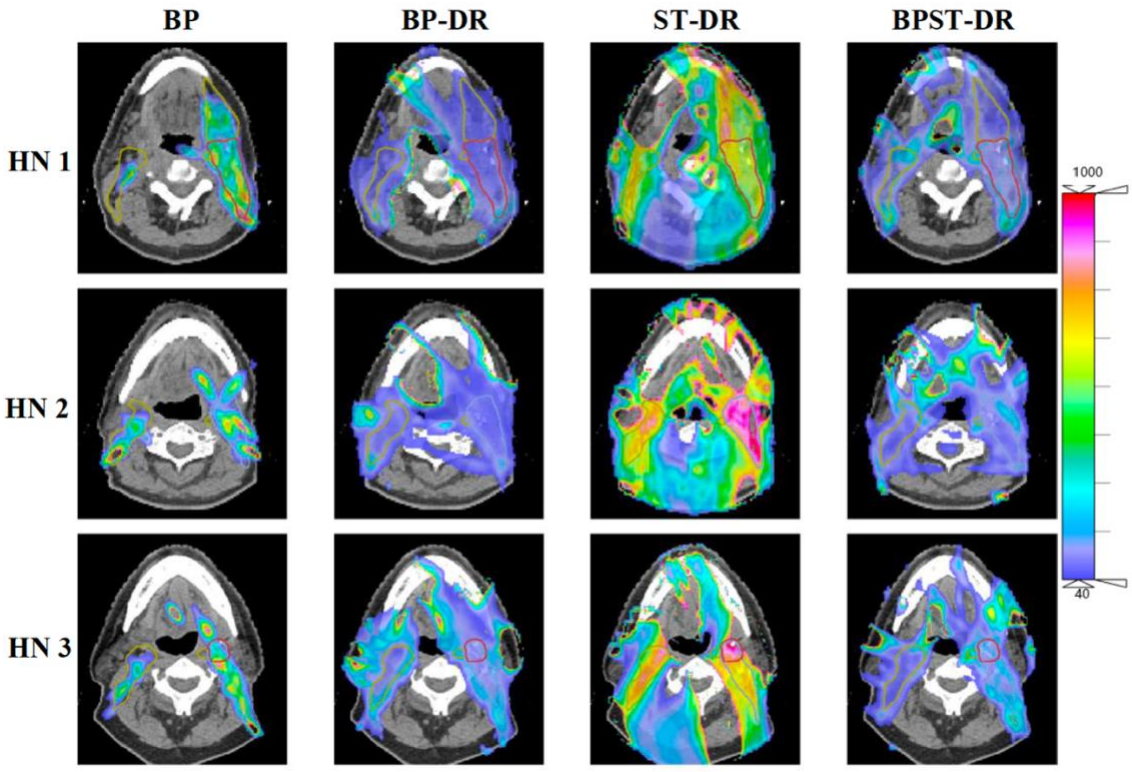

Figure 4-4. Dose rate (Gy/s) comparison between all four plans for each head-and-neck patient.

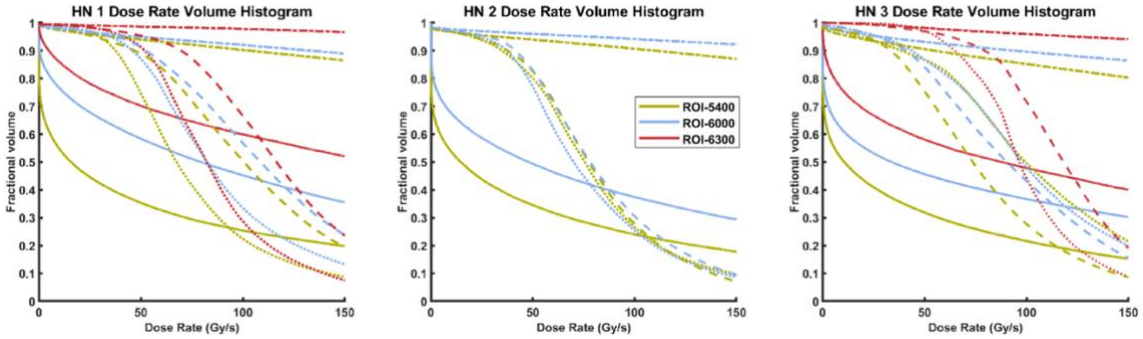

Figure 4-5. Dose rate volume histograms (Gy/s) for ROIs in HN 1, HN 2, and HN 3 (left to right). Solid lines represent BP plans, dotted lines represent BP-DR plans, dash-dotted lines represent ST-DR plans, and dashed lines represent BPST-DR plans.

	HI				Dmax (% of prescription dose)				$V_{\gamma 0,ROI}$ (% of ROI volume)			
Case	BP	BP-DR	ST-DR	BPST-DR	BP	BP-DR	ST-DR	BPST-DR	BP	BP-DR	ST-DR	BPST-DR
HN #1												
CTV54	0.860	0.832	0.655	**0.927**	109	112	134	**103**	38.4	87.6	**94.7**	92.0
CTV60	0.914	0.843	0.660	**0.948**	107	111	131	**101**	61.8	93.2	**95.5**	94.5
CTV63	0.929	0.901	0.810	**0.955**	**102**	105	120	97.1	73.1	95.5	**98.8**	96.8
HN #2												
CTV54	0.842	0.832	0.636	**0.899**	109	110	136	**103**	37.6	87.2	**94.5**	89.0
CTV60	0.877	0.881	0.713	**0.936**	108	108	137	**102**	52.7	87.9	**96.4**	90.9
HN #3												
CTV54	0.858	0.832	0.595	**0.943**	108	110	146	**101**	34.9	89.6	**91.7**	85.2
CTV60	0.896	0.885	0.587	**0.942**	107	109	139	**101**	48.1	91.6	**93.9**	90.4

CTV63	0.908	0.920	0.840	**0.937**	103	103	137	**97.3**	61.1	**98.9**	98.7	97.9

Table 4-5. Homogeneity index, maximum dose to the CTV (Dmax) as a percentage of the prescription dose, and volume of the ROI surrounding each CTV receiving at least 40 Gy/s for the four methods for all patients. Best values are denoted in bold.

4.1.3.3 OAR Dose and Dose Rate Statistics

All scanning spot plans were able to meet dosimetric standards set during optimization. Generally, the ST-DR plans could not provide sufficient tumor coverage even with over 10 beams, and this resulted in high dose spillage into OARs. Table 4-6 reports dose and dose rate statistics for all OAR structures for each plan. The average percent decrease in mean and maximum dose for each structure for all dose rate plans compared to BP are shown in Figures 4-6 and 4-7. BPST-DR is the only plan able to lower both mean and maximum doses in the right submandibular gland, left parotid, and larynx. BP-DR is able to match or improve the maximum dose in the right submandibular gland, left and right parotids, constrictors, and spinal cord. $V_{\gamma 0}$ in the right submandibular gland increased by [49.8%, 68.9%, 25.3%], the left parotid increased by [55.6%, 67.9%, 54.4%], the right parotid by [24.0%, 30.5%, 30.5%], the larynx by [66.5%, 65.7%, 23.3%], the constrictors by [47.7%, 45.7%, 20.9%], the esophagus by [21.6%, 35.9%, 10.4%], and the spinal cord by [7.5%, 72.8%, 13.0%] with BP-DR, ST-DR, and BPST-DR, respectively.

	HN #1				HN #2				HN #3			
	BP	BP-DR	ST-DR	BPST-DR	BP	BP-DR	ST-DR	BPST-DR	BP	BP-DR	ST-DR	BPST-DR

RSubGlnd												
Dmean	11.0	12.2	42.1	**9.5**	12.8	14.5	35.0	**8.5**	16.1	23.7	37.3	**9.4**
Dmax	36.3	35.4	58.4	**32.0**	39.2	38.1	51.4	**36.0**	40.3	41.4	55.3	**36.3**
$V_{\gamma 0}$	15.0	51.2	**99.9**	69.4	50.1	91.2	**99.7**	68.3	27.8	**100**	99.9	31.0
L_Parotid												
Dmean	8.5	10.7	18.7	**6.0**	11.7	13.7	24.6	**10.9**	**7.2**	10.7	31.8	8.1
Dmax	41.9	42.3	55.1	**38.1**	45.3	44.8	64.0	**41.9**	47.3	48.9	68.0	**45.3**
$V_{\gamma 0}$	16.1	63.4	**92.8**	78.4	20.1	83.4	**97.8**	76.8	7.6	**64.0**	56.9	51.9
R_Parotid												
Dmean	**2.5**	3.0	2.7	3.0	**5.7**	8.0	9.9	5.8	4.7	7.2	**4.3**	8.0
Dmax	29.5	33.1	27.1	**29.2**	**39.1**	43.8	55.4	39.6	37.7	45.5	**33.2**	39.9
$V_{\gamma 0}$	0.0	9.7	**31.6**	18.6	8.1	33.7	**41.9**	26.5	1.9	38.4	27.8	**56.3**
Larynx												
Dmean	6.4	11.4	8.8	**2.7**	10.1	14.9	9.4	**8.1**	4.1	7.3	12.2	**3.2**
Dmax	29.8	32.7	33.1	**15.4**	38.5	39.5	31.8	**30.2**	21.4	31.0	41.0	**17.0**
$V_{\gamma 0}$	32.0	83.2	**90.5**	39.6	18.2	**93.8**	91.1	49.0	1.9	**74.4**	67.6	33.3
Constrictors												
Dmean	4.7	8.0	7.1	**3.1**	**5.5**	12.2	6.9	6.4	**7.2**	9.3	9.0	9.4
Dmax	**18.7**	33.5	27.9	19.2	31.6	35.7	34.9	**30.6**	42.0	48.0	**38.1**	44.9
$V_{\gamma 0}$	44.7	60.6	**74.7**	35.1	13.5	**94.2**	71.1	41.7	2.5	49.0	**52.0**	46.6
Esophagus												
Dmean	N/A	N/A	N/A	N/A	5.0	5.8	6.5	**2.2**	**0.6**	1.3	13.0	1.8
Dmax					24.1	26.0	30.1	**12.2**	**4.6**	7.7	37.0	8.9
$V_{\gamma 0}$					17.9	35.7	**47.7**	23.9	0.0	25.4	**42.0**	14.7
Spinal Cord												
Dmean	0.5	0.2	15.1	**0.1**	**1.2**	3.5	14.4	5.0	**0.0**	**0.0**	16.5	2.6
Dmax	3.7	2.1	35.2	**0.8**	**12.1**	12.8	42.0	18.8	**0.0**	**0.0**	45.2	12.3

$V_{\gamma 0}$	0.0	0.2	**91.0**	1.9	0.0	22.4	**81.1**	20.8	0.0	0.0	**46.4**	16.3

Table 4-6. OAR statistic comparison between the four methods for each patient. The Dmean and Dmax to each OAR are listed in Gy, and the volume of each OAR receiving at least 40 Gy/s are listed as percentages. Best values are denoted in bold.

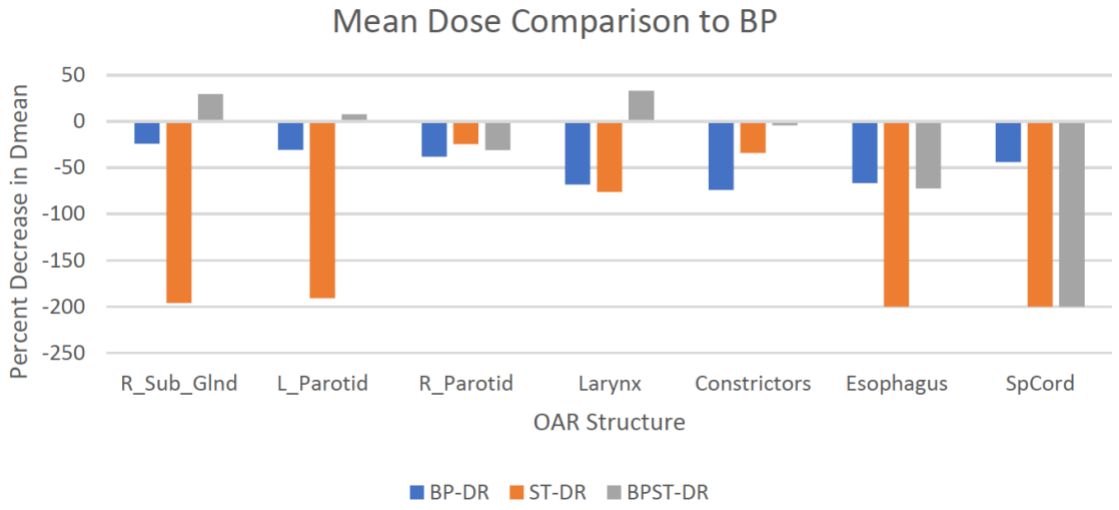

Figure 4-6. Percent decrease in Dmean for BP-DR, ST-DR, and BPST-DR compared to BP plans for each OAR structure.

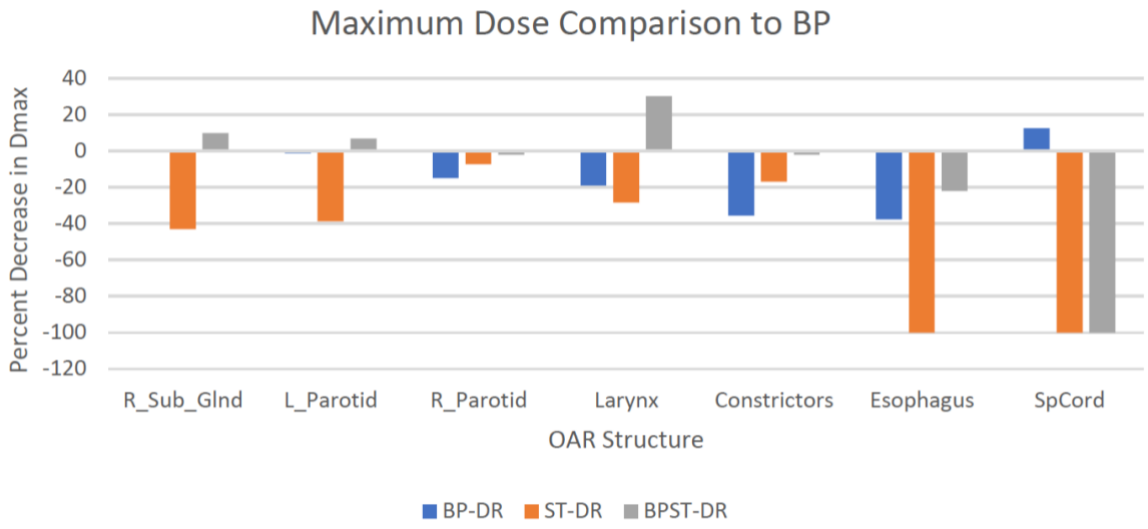

Figure 4-7. Percent decrease in Dmax for BP-DR, ST-DR, and BPST-DR compared to BP plans for each OAR structure.

4.1.3.4 Robustness

Dose rate plans did not improve worst Dmax to CTVs; BP improved this value on average by [4.2%, 24.3%, 5.1%] compared to [BP-DR, ST-DR, BPST-DR]. BP-DR was able to improve worst D95 by 3.1% but was worsened with ST-DR and BPST-DR by [3.4%, 1.7%]. As for OAR robustness, the worst Dmax and Dmean were better with BP plans compared to [BP-DR, ST-DR, BPST-DR] plans by on average [17.1%, 36.3%, 3.2%] and [37.3%, 91.4%, 9.8%], respectively.

4.1.4 Discussion

FLASH radiotherapy has recently emerged as a potentially ground-breaking method to more effectively treat tumors without increasing toxicity. Protons are the most clinically equipped among all treatment modalities due to their achievable high dose rates and deep tissue penetration. However, with the FLASH mechanisms yet to be elucidated, it is imperative in FLASH treatment that the loss in physical dose conformity does not offset the potential gain in the biological therapeutical ratio. Therefore, it is essential in proton FLASH therapy to simultaneously optimize both the dose and dose rate. However, the interdependence of dose and dose rate in proton optimization typically results in a highly non-linear and non-convex optimization problem, such as SDDRO, that is difficult and slow to solve without considering the pertinent beam orientation optimization and robustness problems.

In this study, we have used an integrated beam orientation and scanning spot optimization framework to perform a global search among all feasible Bragg peak and

shoot-through beams to optimize physical dose and encourage high dose rate. Our BPST-DR method improved tumor coverage and allowed the high dose normal tissue volume to benefit from the FLASH effect. By substituting single optimization variable $\boldsymbol{x}$ into the dose-averaged dose rate definition and linearizing the dose rate constraint, the joint optimization problem is significantly simpler and faster to solve than SDDRO. The integrated beam orientation optimization solution is particularly valuable for complex proton FLASH optimization problems where manual beam selection based on experience and intuition is no longer feasible. Furthermore, in our previous studies with BOO, the improvement in dosimetry from the heavier tuning of the L1-norm spot sparsity term was overshadowed by the L2,1/2-norm group sparsity term. In this study, we are able to observe the sparsifying effect of scanning spot regularization through an increase in dose rate. BPST-DR also highlights the speed advantage of sensitivity-based robustness planning vs. worst-case scenario, which multiplies the time for complex planning.

The reported algorithm does not consider variable RBE, which is another layer of complexity. While the ST-DR plans, with their spot placement outside the patient's body, would not rely on these values, the BP, BP-DR, and BPST-DR plans may be affected by such changes in biological dose close to the critical regions of interest. This pattern can also be seen with robustness. Errors in the plan such as physical shifts or CT changes do not strongly affect the dose given by the shoot-through beams within the patient, but the Bragg peak beams, in response to these worst-case scenarios, do have much larger differences from their planned doses. The lack of robustness in the dose rate plans may be explained by the increase in space between spots, caused by the increase in delivery efficiency and the subsequent decrease in number of spots. The increased space increased dose variation

with setup and range uncertainties. Another explanation for the robustness regression in the proposed method is that the BP plan uses a simpler optimization and may prioritize robustness more than the dose rate plans, but we see that the most robust plan out of the three dose-rate plans is the BPST-DR plan, which combines the robust nature of the shoot through beam with an acceptable dose map provided by the Bragg peak beams.

The deliverability of the proton FLASH plans also depends on the specific proton systems. The algorithm produces dose rate values that may be high for the average proton beam. For cyclotrons, reaching high currents in a treatment room may cause large beam losses because of energy switching. Short treatment times may also pose a challenge for non-continuous-wave accelerators like synchrotrons[134]. However, the high dose rate values found in this study may be offset by treatment assumptions made by the DADR definition. There are several main time considerations that threaten the practicality of using DADR in our calculation. First, reoxygenation may occur in between delivery to spots in the same layer and between layers. Current design capabilities for a proton linac report 1 ms as the dead time between spots and 5 ms as the energy switching time[136]. Here, our dose rate optimization is able to significantly lower the number of spots, and the employment of shoot-through beams reduces the number of layers to unity. Improvements in delivery efficiency for Bragg peak beams may be achieved by increasing the longitudinal spot separation or layer spacing in matRad, but further analysis is needed to investigate its impact on plan quality.

Another consideration that may lower the dose rate is the gantry switching time. In a typical IMPT planning process, 2-4 proton fields are chosen[35], but with FLASH modality, a

single beam is chosen in the clinic to avoid reoxygenation as the beam rotates. One way to avoid this is to spatially separate the beams as much as possible to ensure that normal tissue voxels do not receive dose from more than one beam. In our previous studies, we found that the L2,1/2-norm group sparsity term selected spatially separate beams compared to an L2,1-norm. Nevertheless, a larger number of beams must be selected in the shoot-through method to achieve acceptable OAR sparing[146], compared to the Bragg peak-based plans, which need fewer beams for superior dose conformity. In the current study, adding a single shoot-through beam is shown valuable to sparsify the spots from Bragg peak beams within ROIs and then increase the dose rate. Furthermore, the careful positioning of Bragg peak and shoot-through beams pushes dose closer to the center of the CTVs, decreasing hot spots and sparing critical surrounding organs. Extra shoot-through beams might be worth an increase in delivery time if the dose averaged dose rate is maintained above a higher threshold.

The proposed DADR model was dependent on estimations of intensity for a pulsed proton beam[151] and has yet to be validated against experimental data. In this work, the time spent per spot must be high enough to counter reoxygenation effects, but more experimentation is needed to determine how impactful these effects are over the course of FLASH treatment[153,154]. The DADR definition, with its ability to be linearized into the form of our objective function with a single 3D instantaneous dose distribution, is simply an instrument used to investigate the role of beam positioning and spot selection in the refinement of dosimetry with ultra-high dose rates.

4.1.5 Conclusion

We have developed an efficient and robust dose and dose rate optimization method with automated beam and spot selection. Combined use of Bragg peak and shoot-through beams was shown to significantly improve dose rate in the regions of interest surrounding the tumor while maintaining physical dose conformity compared to traditional IMPT methods. The proposed method thus can be a planning option for future proton FLASH clinical studies.

4.2 Multi-field optimization feasibility for FLASH pencil-beam scanning proton therapy

4.2.1 Introduction

Pencil-beam scanning IMPT has been recognized for its ability to widen the therapeutic ratio by positioning spots precisely within the target volume[155]. However, one limitation of IMPT is its relatively slow delivery of radiation, as it typically requires a continuous dose to those spots spanning several minutes[156,134]. Given this limitation, the feasibility of FLASH radiotherapy using protons is called into question.

Several recent studies have shown that proton FLASH radiotherapy can increase radioresistance and reduce potential damage to healthy tissue via mechanisms possibly related to oxygen consumption but not completely understood[20,33,146,157]. However, clinical delivery of FLASH dose rates with PBS-IMPT is not trivial due to finite spot and energy layer switching times to cover a target volume and gantry rotation times to achieve optimal dosimetry[158,159]. This dead time may result in reoxygenated and potential elimination of normal tissue sparing effects. The inclusion of dead time differs between definitions of FLASH dose rate. On the upper limit, the voxel-based DADR definition proposed by van de Water et. al. does not consider energy switching or gantry switching times[151]. On the lower limit, the average dose rate definition accounts the total delivery time from all dose contributions, including spot switching, energy switching, and gantry switching time[160]. The problem is further complicated by the variability in switching times between clinical systems. For example, the reported energy layer switching time for a cyclotron is 100 ms, but only 5 ms for a proton linac[136]. Furthermore, there is variability in the definition of dose rate[160]. This obstacle can be mitigated with an energy modulator, e.g., ridge filters[161].

However, the gantry rotational time for multiple beam angles cannot be easily overcome. Recent studies have objected to using more than one beam angle[162], showing that the average dose rate drops significantly due to the long gantry switching times, which may be ~1 minute long for a 360-degree rotation[163]. Using a single beam would compromise physical dose conformity, which elevates the normal tissue toxicity that is exacerbated with necessary hypofractionation to increase MU and FLASH dose rates. The simple solution would be to manually separate the IMPT beams in space to minimize multiple dose contributions to voxels, but there is no current evidence to suggest the

feasibility of achieving FLASH dose rates with this method without compromising dosimetry.

The study has two objectives: first, we investigate a novel optimization method to eliminate the impact of gantry rotation time on average dose rate via a spatially separated beam orientation optimization (SSBOO) algorithm. We then determine what the minimal "biological effectiveness" of FLASH radiotherapy would have to be for the resulting dosimetry of the SSBOO plan to outperform standard multi-field IMPT plans, which are still dosimetrically superior.

4.2.2 Methods

4.2.2.1 Spatially separated beam orientation optimization for dose overlap minimization

The spatially separated beam orientation optimization (SSBOO) formulation, represented by Equation 4-5, expands on the BOO framework by selecting beams that are further apart in space to penalize dose overlap while maintaining sufficient dose to the tumor region. For a pre-defined subdivision of the tumor (e.g., left and right sides for a bilateral head and neck case), the SSBOO framework may simply select parallel opposing beams as the most obvious solution.

$$minimize \underbrace{\sum_{r\in CTV} w_r \|A_r \boldsymbol{x} - p_r\|_2^2}_{CTV\ term} + \underbrace{\sum_{s\in OAR} w_s \|(A_s \boldsymbol{x} - m_s)_+\|_2^2}_{OAR\ term}$$

$$+ \underbrace{\sum_{q\in ROI} w_q \left\| \left(\sum\nolimits_{b=1}^{B} \sigma\left(\left(A_q x\right)_b\right) - 1\right)_+ \right\|_2^2}_{voxel\ repetition\ term}$$

Equation 4-5

The voxel repetition term includes a sigmoid function represented by $\sigma(d)$, which is similar to the Heaviside step function. It binarizes the dose contribution in each voxel for each beam[164]. Then, the number of beams delivering dose to voxels in the regions where a FLASH effect is desired would be forced to be under one. Unlike the Heaviside function, the sigmoid transform is differentiable over all dose values. The parameter θ may be tuned to control the steepness of the binarization, essentially creating a step function that is neither convex nor concave. Here we define the function in Equation 4-6 below.

$$\sigma(d) = \frac{1 - e^{-\theta d}}{1 + e^{-\theta d}}$$

Equation 4-6

4.2.2.2 Optimization Algorithm

Since a global search using a top-down approach would be tedious for the selection of 1-2 beams, we propose that the beam orientation optimization be performed with a modified version of our previously developed PathGD technique, a greedy path-seeking gradient descent algorithm with beam fitness calculation. The modified PathGD with voxel repetition penalization is shown in Appendix 6.4. The gradients of the two dose fidelity terms are first calculated, showing the direction of the steepest descent towards a local minimum. Next, we calculate the gradient for the voxel repetition term, which determines which beams would produce the least amount of overlap given their possible dose contributions (i.e., given the gradient from the dose fidelity). The beam that produces the largest descent, which is deemed to be most fit as the next beam chosen, is then selected and optimized. Besides its computational speed and automated beam selection, PathGD can

provide a beam-by-beam analysis of dosimetric cost as well as ultra-high dose rate capability. After the beam(s) have been selected, FISTA may be used for an extra fluence map optimization step.

4.2.2.3 Average dose rate definition

The spot sparsity term(s) above can be tuned higher with weight η to increase the dose rate. By increasing spot sparsity, the number of spots contributing dose to a voxel are lowered, decreasing the delivery time. The average dose rate is defined by the total dose delivered to a given voxel divided by the amount of time required to deliver all spot contributions to that voxel. In Equation 4-7, D_i represents the total dose to voxel i in Gy, $t_1 = t_i(D_i^-)$ and $t_0 = t_i(0^+)$. We use the expressions – and + to remove the beam-on time before and after the dose contribution to each specific voxel.

$$\dot{D}_i = \frac{D_i}{t_1 - t_0}$$

Equation 4-7

The average dose rate definition ensures that spot scanning time, energy layer switching time, and gantry rotation time are incorporated into the total voxel delivery time. The average dose rate is comparatively lower than other dose rate definitions, including the PBS dose rate, the percentile dose rate, and the dose-averaged dose rate[160].

4.2.2.4 Patient evaluation

The following study reports the trade-off between optimal dosimetry using multiple proton fields and FLASH sparing using a single field, assuming the average dose rate definition is used for analysis. Aperture optimization is not yet considered. We perform a spatially separated beam orientation optimization using PathGD to select 2 beams from the 4π space and compare this plan (2BM-VR) to 1-4 beam plans without the voxel repetition term (nBM-NVR).

One bilateral head-and-neck (H&N) case, one pancreas (PANC) case, and one prostate (PRT) case were used for the study, listed here in order of increasing complexity due to critical structures surrounding the tumor. The original candidate beam set consisted of 1162 non-coplanar beams distributed across a 4π space with 6° separation. A subset of around 215-250 beams were created for each patient, with many beams excluded due to gantry and couch collisions, infeasible depths, or an undesired entrance through the partially segmented body mask. Spots were separated laterally by 5 mm, and the energy layer separation was 3 mm. Table 4-7 lists the tumor information for each patient along with the average number of available proton spots covering all tumors.

Case		Prescription Dose (Gy)	CTV volume (cc)	Average spots per proton beam
PRT	CTV40	40	111	2,452
PANC	CTV35	35	76	2,080
H&N	CTV54	54	110	9,433
	CTV60	60	99	
	CTV63	63	10	

Table 4-7. Prescription doses and volumes for each target with average number of spots per proton beam for each patient.

After performing fluence map optimization for the selected beams, plans were normalized to 95% of the target volumes receiving prescription dose. CTV HI, D98%, and maximum dose, and mean and maximum OAR dose were evaluated. We calculate the average dose rate assuming a spot scanning time of 2.5 ms and an energy layer switching time of 5 ms. We then identify the voxels receiving dose from more than 1 beam and add on the calculated partial gantry rotation time to t_1, assuming a full 360-degree gantry rotation time of 1 minute, to determine whether the average dose rates in the OARs are still above 40 Gy/s. More specifically, we ensure that the voxels of the OARs receiving doses above clinically defined radiation limits receive FLASH dose rate protection. Radiation dose constraints for the relevant cases are listed in Table 4-8.

Organ	**Rx Dose**	**Constraints**	**Source**
Submandibular+ Parotid glands	58-72Gy x 40	V15Gy < 67%, V30Gy < 45%, V45Gy < 24%, Dmean < 25Gy	Deasy et al (2010)[165]
Larynx	54-70Gy x 30	V50Gy < 27%, Dmean < 44Gy, Dmax < 66Gy	Anderson et al (2010)[166]
Constrictors	54-70Gy x 35	V50Gy < 70%, Dmean < 50Gy	Mazzola et al (2014)[167]
Rectum	64-72Gy x 35	V50Gy < 50%, V70Gy < 30%	Li et al (2021)[168]
Bladder	64-72Gy x 35	V55Gy < 50%, V70Gy < 30%	Li et al (2021)[168]
Penile Bulb	64-72Gy x 35	V50Gy < 70%, V70Gy < 30%	Li et al (2021)[168]

Bowels, Stomach	33-40Gy x 5	V35Gy < 10cc, V20Gy < 30cc, Dmax < 40Gy	Rhee et al (2023)[169]
Kidneys	33-40Gy x 5	V12Gy < 25%	Rhee et al (2023)[169]
Liver	33-40Gy x 5	V12Gy < 50%, Dmax < 55Gy	Rhee et al (2023)[169]

Table 4-8. Radiation dose limits for organs involved in patient cases.

4.2.3 Results

*4.2.3.1 **Beam angle selection***

The SSBOO method was tested on the three patient cases, which selected beams with (gantry angle, couch angle) following IEC 61217 coordinate conventions. The beams are displayed in Figure 4-8. For [1BM, 2BM-NVR, 2BM-VR] plans, the number of active/ non-zero spots (and percentage of the total available spots) after fluence map optimization were [796 (32.1%), 1140 (23.0%), 1251 (25.2%)] for the PRT case, [541 (25.8%), 746 (17.9%), 1200 (28.5%)] for the PANC case, and [3205 (46.9%), 6362 (46.7%), 3667 (26.8%)], for the H&N case.

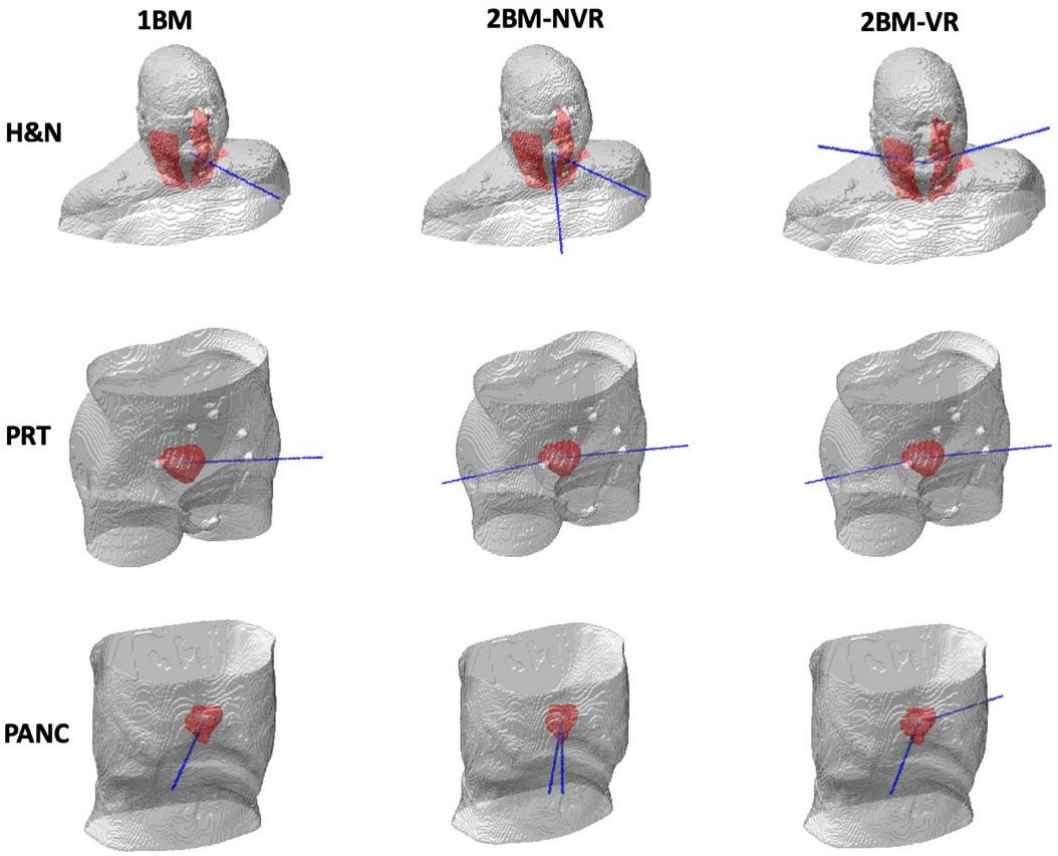

Figure 4-8. Beam angle diagrams for 1BM, 2BM-NVR, and 2BM-VR plans for all three cases. Beams are chosen by the PathGD framework. CTVs are shown in red and blue lines represent beams entering the patient.

The dose map for 2BM-VR plans, showing the entrance of each beam through the patient, is shown in Figure 4-9. The optimizer spatially separates the beams enough so that dose from one beam does not overlap the dose from the other beam.

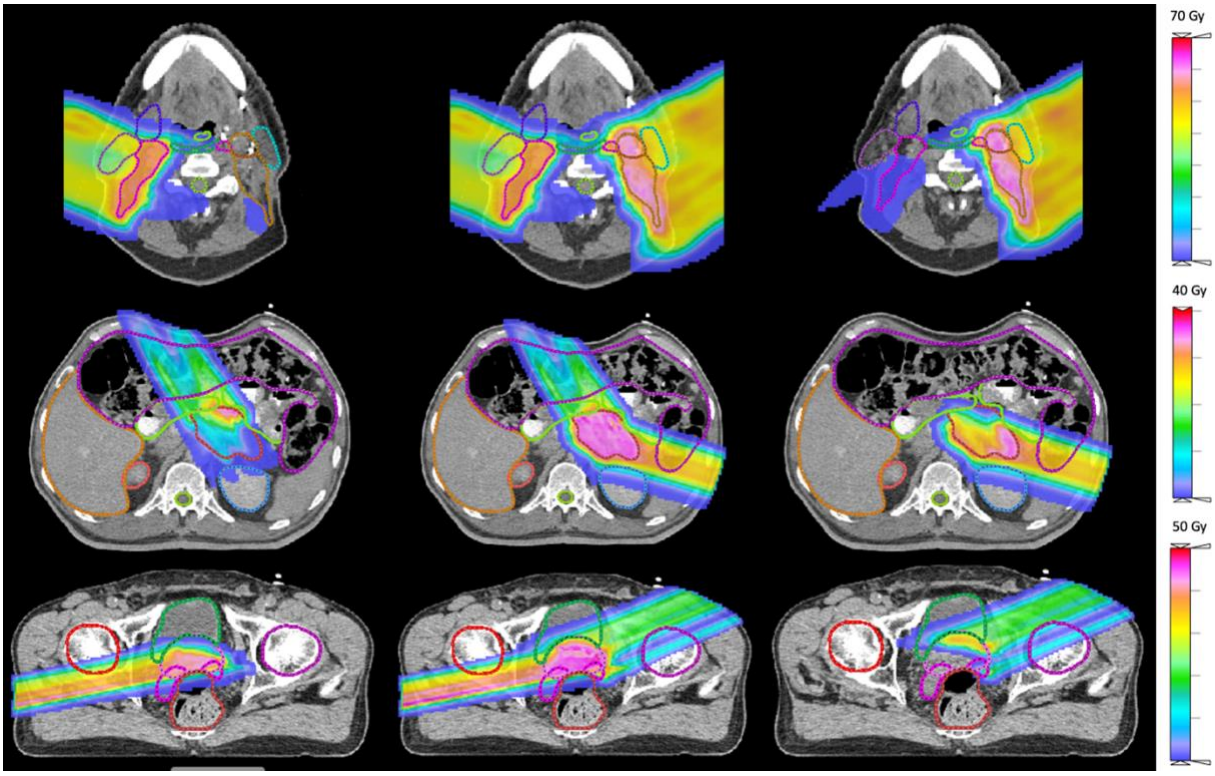

Figure 4-9. Dose map representation (Gy) of 2BM-VR plans for all patients, including the contributions from the individual beams.

4.2.3.2 Dose statistics

Unsurprisingly, the two beam plans showed superior dosimetry compared to 1BM, with a [5.0%, 4.7%, 6.1%, 3.7%] improvement in CTV [HI, D95%, D98%, Dmax] for 2BM-NVR and a [5.1%, 5.9%, 7.7%, 2.4%] improvement for 2BM-VR. 2BM-NVR experienced a drop in OAR mean and maximum dose by on average a 11.4% and 8.5% compared to 1BM, while 2BM-VR dropped by on average 5.8% and 1.7% in structures, with the exceptions being the right parotid and spinal cord for the H&N case, the right femur for the PRT case, and liver and left kidney for the PANC case. A higher number of active spots did not necessarily correlate with the improved dosimetry with the two beams. The SSBOO framework attempts to increase the dose (adding more active spots) within a smaller region inside the CTV, which

increases the entrance dose to that of a single beam but decreases the dose to the contralateral side of the CTV, thus affording greater flexibility to spare the OARs near the CTV. Nevertheless, the improved OAR statistics for 2BM-VR over 1BM are still inferior to 2BM-NVR due to the additional field separation constraints. The next step is to determine the minimal FLASH effect needed to compensate for the loss in physical dose conformity. The dose-volume histograms for all three cases are shown in Figure 4-10, and the improvement in OAR dosimetry with [1BM, 2BM-NVR, 2BM-VR, 3BM-NVR] compared to 4BM-NVR dosimetry is shown in Figure 4-11. The black bars shown for each plan represent the improvement in cost, assuming that the biological effectiveness of the FLASH effect is a 30% decrease in dose. From the figure, we see how large of an improvement can be made with such an assumption for 1BM and 2BM-VR plans, in particular, due to the FLASH dose rate effect.

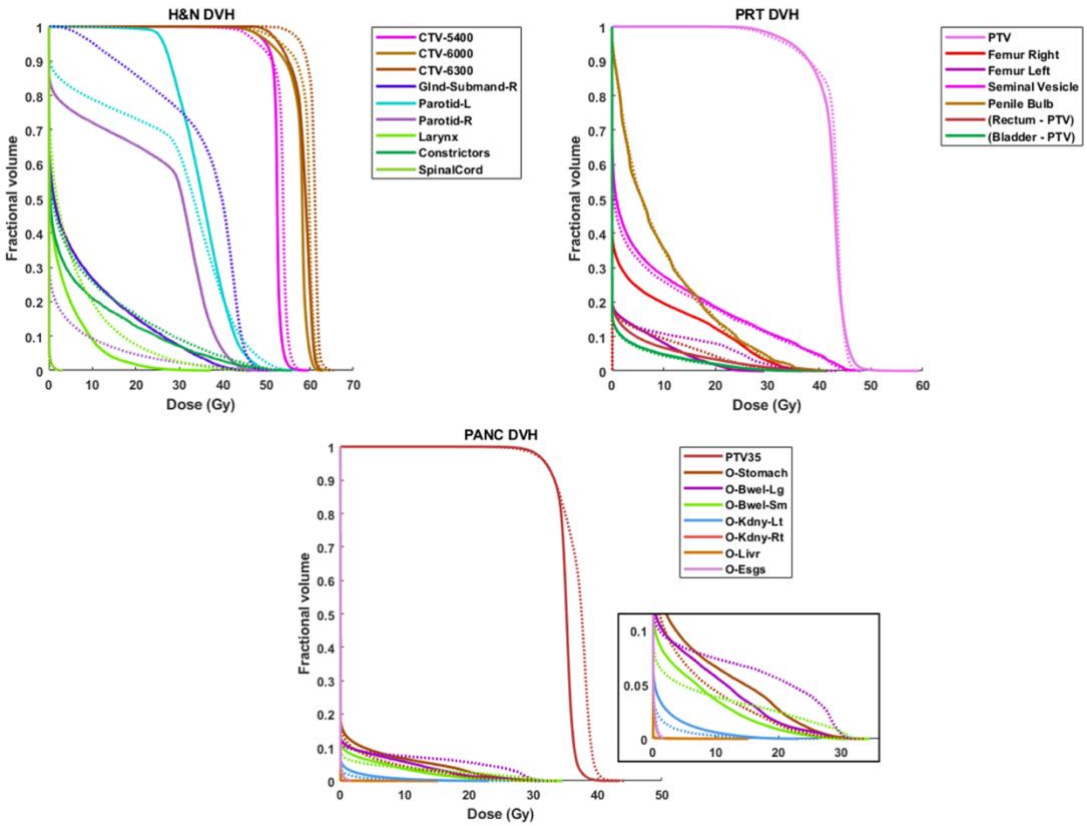

Figure 4-10. Dose volume histogram (DVH) plots for all three cases. Solid lines represent 2BM-VR plans while dotted lines represent 1BM plans.

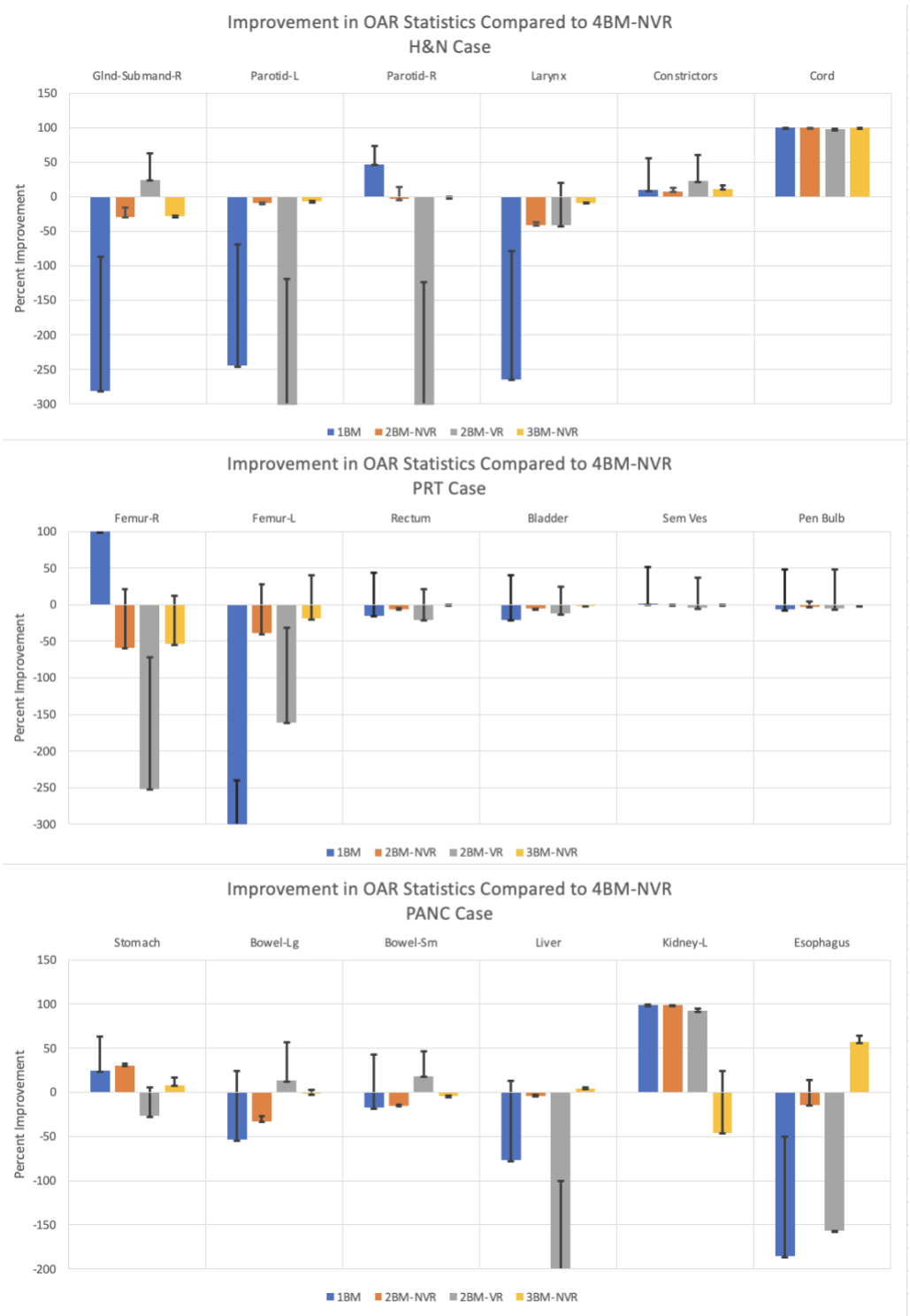

Figure 4-11. OAR cost improvement with 1BM, 2BM-NVR, 2BM-VR, and 3BM-NVR plans compared to 4BM-NVR plans for all three patient cases. Error bars display the improvement considering a 30% reduction in dose for voxels receiving FLASH dose rates.

More specifically, the mean dose in [right submandibular gland, left parotid, right parotid, larynx, constrictors] for 2BM-NVR plans generally decreased by [0.3, 0.1, 0, 0.05, 0.1] Gy with every 10% reduction in dose within voxels receiving a FLASH dose rate, while 2BM-VR plans decreased by [0.5, 3.3, 2.2, 0.2, 0.4] Gy. For the dose in [stomach (Dmax), large bowel (Dmax), small bowel (Dmax), left kidney (Dmean)], 2BM-NVR resulted in a reduction rate of essentially 0%, but with 2BM-VR, a subtle [0.1, 3.1, 0, 0.1] Gy reduction was observed. For the dose in [right femur (Dmean), left femur (Dmean), rectum (Dmax), bladder (Dmax)], the reduction was [0.3, 0.1, 0, 0] Gy for 2BM-NVR and [0.5, 0.2, 0, 0.8] Gy for 2BM-VR. Averaged over all structures showing a nonzero reduction rate for each case, for 1BM and 2BM-VR to outperform the OAR doses of [2BM-NVR, 3BM-NVR, 4BM-NVR], the FLASH dose rate would have to produce a [27.2%, 34.0%, 27.8%] and [28.7%, 29.4%, 22.5%] reduction in equivalent dose for the head-and-neck case, [11.1%, 25.2%, 16.3%] and [49.5%, 47.5%, 60.6%] reduction for the pancreas case, and [35.1%, 45.3%, 45.6%] and [37.8%, 50.3%, 44.7%] reduction for the prostate case.

4.2.3.3 Dose rate statistics

All average dose rates were calculated assuming a single fraction. For the H&N case, the percentage of the volume receiving greater than 40 Gy/s increased with the 2BM-VR compared to 2BM-NVR by 39.4% for the right submandibular gland, 69.0% for the left parotid, 63.2% for the right parotid, 8.9% in the larynx, 9.4% in the constrictors, and 2.2% in the spinal cord. For the PRT case, the percentage decreased in the right femur by 5.9%, but increased in all other structures by 1.6% in the left femur, 5.1% in the rectum, 8.6% in

the bladder, 3.1% in the seminal vesicles, and 1.1% in the penile bulb. Lastly, for the PANC case, the percentage increased in the stomach by 4.7%, 42.8% in the large bowel, 26.1% in the small bowel, 1.9% in the left kidney, 23.5% in the liver, and 0% in the esophagus.

The significance of the increase in dose rate for 2BM-VR plans is more impactful when considering the critical volumes that most benefit from a FLASH protective effect. For example, whereas with the 1BM and 2BM-VR plans, 100% and 67.2% of the bladder receiving greater than 20 Gy was covered by a dose rate higher than 40Gy/s, the 2BM-NVR plan only covered 1.3% with an ultra-high dose rate. The percentage of critical volumes receiving FLASH protection are listed in Table 4-9.

Organ	**Dose (Gy)**	**Volume Receiving Dose (%)**					**FLASH Dose Rate Coverage (%)**				
		1BM	2BM-NVR	2BM-VR	3BM-NVR	4BM-NVR	1BM	2BM-NVR	2BM-VR	3BM-NVR	4BM-NVR
R Sub Glnd	15	90.8	43.7	20.4	43.0	31.0	100	19.4	100	1.8	0.9
Parotid Left	15	76.1	20.1	100	19.1	17.6	100	4.8	100	2.0	1.1
Larynx	40	0.4	<0.1	<0.1	<0.1	<0.1	100	0	100	0	0
Constr.	50	0.6	0.5	0.3	0.4	0.3	100	6.8	100	5.1	0
Rectum	20	4.3	2.9	3.4	2.6	2.5	100	0	27.8	0	0

Bladder	20	1.8	1.6	2.0	1.4	1.4	100	1.3	67.2	0	0
Penile Bulb	20	15.0	13.0	14.8	0.1	0.1	100	11.6	98.7	0	0
Stom.	20	1.3	1.0	0.9	0.9	0.9	100	0	46.3	0	0
Small Bowel	20	2.5	2.3	0.9	1.8	1.7	100	0	61.7	0	0
Kidney Left	12	17.5	19.8	13.9	<0.1	<0.1	100	0	41.0	0	0
Liver	5	<0.1	<0.1	<0.1	1.3	0.7	100	0	71.4	97.8	80.3

Table 4-7. Percentage of critical volumes receiving FLASH dose rate coverage for all plans. Critical volumes are defined as regions of OARs receiving above the listed dose (Gy).

A representation of the dose and dose rate values is shown in Figure 4-12. For each dose bin of width 0.5 Gy, the mean of the dose rate values across voxels receiving doses within that range was plotted for each plan. The plot demonstrates that structures that receive high doses above dosimetric constraints may not be covered by the FLASH effect with the 2BM-NVR, 3BM-NVR, and 4BM-NVR plans, but are covered with the 1BM and 2BM-VR plans.

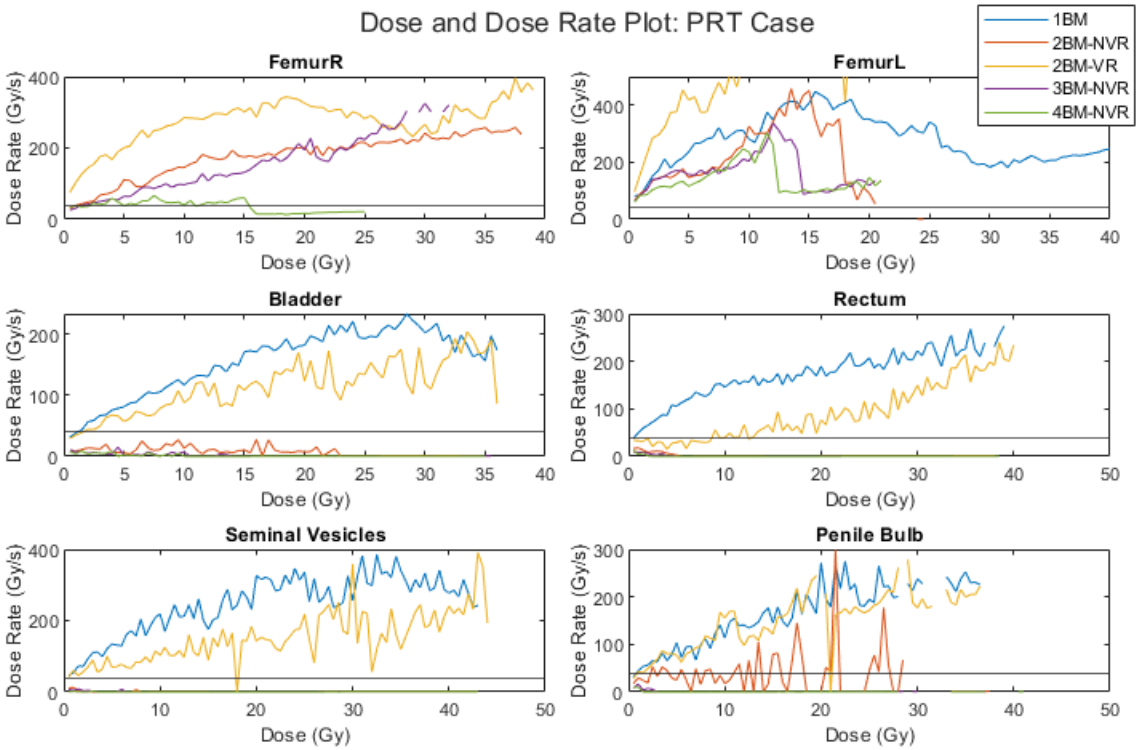

Figure 4-12. Dose (Gy) and dose rate (Gy/s) plots for OAR structures for the PRT case assuming a single fraction. A line at 40 Gy/s is shown to identify voxels receiving high dose that are not protected by the FLASH effect.

*4.2.3.4 **Robustness***

Although range and setup uncertainties were not taken into account within the optimization, a worst-case analysis was performed to determine the robustness of the final fluence maps of the 2BM-VR plans. The fluence map vector was the same during the calculations while the dose calculation matrix was altered by shifting the beam isocenter by $\pm$3 mm along the anteroposterior, superior-inferior, and mediolateral directions to simulate setup uncertainties, and by scaling the CT number by $\pm$3% to simulate range uncertainties. Compared to 2BM-NVR, the worst-case CTV [HI, D95%, Dmax] declined by [27.2%, 30.0%, -9.0%] for the H&N case, [31.1%, 24.4%, 42.0%] for the PRT case, and [12.3%, 9.6%, 32.0%]

for the PANC case with 2BM-VR. Furthermore, the worst-case OAR [Dmean, Dmax] increased by [131%, 16.0%] for the H&N case, [30.0%, 16.4%] for the PRT case, and [48.5%, -15.6%] for the PANC case with 2BM-VR. Similar to Table 4-9, Table 4-10 shows the volume of the structure receiving greater than the critical dose and the percentage of the critical volume receiving that dose in the worst-case scenario. Although the dose may increase in uncertainty scenarios, the spot weight distribution does not change, and the average dose rate generally tends to increase with the dose.

Organ	**Dose (Gy)**	**Volume Receiving Dose (%)**					**FLASH Dose Rate Coverage (%)**				
		1BM	2BM-NVR	2BM-VR	3BM-NVR	4BM-NVR	1BM	2BM-NVR	2BM-VR	3BM-NVR	4BM-NVR
R Sub Glnd	15	91.5	47.2	22.5	47.1	35.2	100	19.4	100	1.7	0.8
Parotid Left	15	76.7	21.3	99.8	20.8	18.9	100	5.3	100	2.6	0.5
Larynx	40	0.7	0	9.2	0	0	100	0	63.5	0	0
Constr.	50	0.8	1.3	11.8	1.4	2.5	100	8.6	99.0	8.6	0
Rectum	20	11.8	7.8	7.4	6.1	5.2	100	0.8	47.7	0	0
Bladder	20	1.8	1.6	2.0	1.7	1.7	100	0.7	67.2	0	0
Penile Bulb	20	15.0	14.2	15.0	13.8	13.6	100	11.0	100	0	0

Stom.	20	1.3	1.0	3.1	0.1	0.9	100	0	49.4	0	0
Small Bowel	20	2.5	6.1	2.3	1.8	1.7	100	0	72.3	0	0
Kidney Left	12	1.6	1.4	0.5	<0.1	1.8	100	6.8	42.0	0	1.3
Liver	5	<0.1	<0.1	0.1	1.3	0.7	100	0	87.1	97.8	80.3

Table 4-8. Worst-case percentage of critical volumes receiving FLASH dose rate coverage.

4.2.4 Discussion

Despite being the most promising FLASH delivery method, there are two major challenges with PBS-IMPT reaching the ultra-high dose rate without significantly sacrificing dose conformity to the degree that the physical dose loss outweighs potential FLASH biological gains. The first challenge is that the energy layer switching time is highly variable among different delivery systems, but this can be mitigated with several techniques, including using the shoot-through mode and an energy modulation device such as the ridge filter. The current study focuses on the second challenge, which is that the long gantry switching time reduces the average dose rate to under the FLASH threshold, regardless of the beam current and instantaneous dose rate. Previous multi-field optimization studies for IMPT have ignored the second challenge[145]. The study described here first minimizes the physical dose loss by introducing the spatially separated beam orientation optimization (SSBOO) algorithm, which identifies multiple dose contributions

to a voxel as the main culprit for the reduction in dose rate. SSBOO uses a voxel-repetition term, consisting of a sigmoid function, to penalize overlap in beams to voxels in which a FLASH effect is desired. The study further quantified what the minimal FLASH biological dose reduction would be to reach a net gain in the therapeutic ratio. SSBOO improved the dosimetry compared with single beam IMPT by offering greater flexibilities to spare surrounding OARs but is still inferior to the multiple field IMPT without the additional field separation constraint. As a result, the FLASH biological dose reduction must be greater than 25-40% to achieve a net gain in the therapeutic ratio. The necessary FLASH effect would have been greater, with one field IMPT showing worse physical dose conformity than SSBOO. The values may be compared to the reported FLASH biological dose reduction. Several studies have reported changes in dose resulting in the same biological outcome under conventional dose rates vs. ultra-high dose rates[29,170,171]. The resulting dose modifying factor for electrons *in vivo*, which is also termed the FLASH biological effectiveness, is around 1.36 (range: 1.13-1.80)[29], which is within the range of our reported values for therapeutic ratio gains. However, for both electrons and protons, the reported *in vitro* FLASH biological effectiveness is more modest, closer to 1.1[170]. The biological underpinning for the lower proton FLASH biological effectiveness is unclear. Still, the low values are alarming, suggesting a possibility that the *in vitro* proton FLASH effect may not materialize in the clinical settings if significantly higher *in vivo* proton FLASH effects are not observed.

It is noteworthy that the effectiveness of SSBOO depends on the anatomy. The SSBOO framework performs well for bilateral head and neck cases because of clearly defined tumor structures on the left and right sides of the patient. SSBOO selects two beams

that are more likely to be (but not required to be) opposing beams, entering through the left and right hemispheres. Elevation in OAR dose may be compensated by the significant dose rate increase. For the cases involving a single, centric tumor (i.e., the pancreas and prostate cases), SSBOO is challenged to find two beams that would cover the same tumor region without overlapping doses in the OARs. For these tumors, a single proton beam may be the ideal solution if biological experimentation proves the effectiveness of the FLASH effect to be less than 35%.

The average dose rate was chosen for the dose rate analysis in this study due to its simplified calculation and consideration of all dose contributions. However, the average dose rate is a particularly pessimistic dose rate definition. For example, both the PBS and percentile dose rate definitions use an arbitrary dose threshold, which may be a percentage of the prescription dose or a value proportional to the dose delivered to that voxel. These definitions ignore the delivery time of low dose contributions, whereas the average dose rate accounts for all cumulative dose contributions, and was found to be around 50% of the PBS and percentile dose rates[160]. Beyond the dose rate definition, there are several methods to increase the dose rate that are currently in development. Firstly, shoot-through beams pass through the target with a single energy without stopping, enabling a faster radiation delivery and removing the energy layer switching time[172]. Shoot-through beams used in combination with dynamic ridge filters[173] can attempt to mimic the spot-scanning technique. However, this requires additional labor to construct and perfect. Secondly, spot sparsity optimization methods have attempted to decrease the total number of spot

contributions to OAR voxels[174], but it is still unclear how significantly this affects the plan dosimetry and robustness for different tumor sites.

The gradient descent method here is modelled after a path-seeking algorithm called PathGD[46], which is a greedy approach that selects beams in sequence based on the calculation of a beam fitness term and performs fluence map optimization between beam additions. The fitness term for each beam is based on the potential cost improvement after a single iteration, making PathGD an efficient solver, particularly for convex problems. It has been shown to select beams that are further apart in space compared to other algorithms such as column generation, or even global solvers such as FISTA, due to its ability to build off the previously optimized fluence map.

Finally, an RBE of 1.1 was assumed for all cases. However, in proton therapy, the importance of using variable RBE-based or LET-based optimization lies in the ability to more accurately account for the biological effects of protons in different tissues and tumor types, resulting in enhanced normal tissue sparing and better tumor control. Further study may account for biological effects using the previously discussed optimization frameworks.

4.2.5 Conclusion

We have developed a beam orientation optimization algorithm that can spatially separate proton beams and penalize their overlapping dose contributions to organs at risk to ensure they receive a FLASH dose rate. The method achieves superior dosimetry to single-field proton therapy yet maintains a high dose rate for potential FLASH effects. The

study also quantifies the minimal *in vivo* proton FLASH biological effectiveness for different disease sites to achieve a net gain in the therapeutic ratio.

5 Beam Orientation Optimization for Carbon Ion Therapy

5.1 Fixed Beamline Optimization for Intensity Modulated Carbon-Ion Therapy

5.1.1 Introduction

Carbon-ion therapy has been increasingly garnering attention worldwide due to its superior physical dose distributions and high RBE. Compared to photon and electron beams, proton and carbon ion beams are more conformal to tumors because they deliver most of their dose in well-defined Bragg peaks, therefore possessing the ability to localize their deposition of energy within deep-seated tumors[24,175,176]. About 85% of cancer patients receiving particle therapy are irradiated with protons, which have physical advantages compared to photons, but a similar biological response[24]. Carbon ions, however, have a steeper lateral fall-off and smaller penumbra than proton beams, which offers a better potential for targeting tumors that are close to critical structures[81]. The RBE of carbon ion rises substantially along the beam direction and reaches its maximum near

the Bragg peak, further increasing the therapeutic ratio. Heavy ions are particularly attractive for treating radioresistant tumors, and carbon ion therapy may promote immune response and reduce angiogenesis and metastatic potential[177,178]. Through clinical studies, carbon ion beams have been able to reduce treatment time and toxicities[175], making it the desirable treatment modality in terms of efficiency and dosimetry.

However, the access to carbon-ion therapy is greatly hampered by its prohibitive cost, engineering challenges and space requirement, despite its unique potential to treat hypoxic and radioresistant tumors. Among the facilities of carbon-ion therapy, the fully rotational gantry is especially expensive, complex and space consuming due to the large magnets needed to bend the high energy carbon ion beams with high magnetic rigidity. Compared with protons, to reach the same depth, the magnetic rigidity of carbon ions is 2.5 times greater, demanding corresponding more powerful and larger magnets for beam bending and steering. As a result, the carbon gantry in the Heidelberg Ion Therapy (HIT) facility occupies 22 m long and 14 m high space and weights a total of 600 tons[179]. Equipment and building costs, in particular, are extremely high[180,181]. The gantry weight can be reduced using superconducting magnets. For example, the superconducting carbon ion gantry at the National Institute of Radiological Sciences (NIRS) in Japan weighs 300 tons[37,182] due to the use of superconducting magnets, which are costly to build and operate, and still significantly heavier than a proton gantry. Further engineering challenges include maintaining the targeting accuracy with gantry rotation. There are limited existing solutions available for equipment and treatment planning software troubleshooting by suppliers.

The current debate at many cancer treatment centers in relation to carbon ion therapy is whether the installation of a gantry is feasible. Compared with the gantry systems, fixed-beam port systems significantly simplify the system design for carbon ion therapy and are more widely employed in most carbon ion centers for treatment delivery at the moment. However, the fixed beam line design has been considered a significant compromise in flexibility and achievable dosimetry. Once built, the directions of fixed beamlines cannot be modified. The unclear magnitude of performance degradation and lack of systematic approach to mitigate the compromise could dampen the enthusiasm for carbon ion system adoption.

Carbon ion centers are employing the use of a single horizontal beam (90°), some with an additional vertical beam (0°)[183,184]. Kosaki et al. compared intensity modulated proton therapy (IMPT) plans for the treatment of skull base meningioma and found that excellent dose distributions can still be achieved with one fixed beam[184]. To determine if there is a superior fixed beamline configuration for a typical two beamline configuration, Koom et al. performed a dosimetric comparison among seven fixed beam angles (340°, 315°, 0°, 20°, 45°, 90°, 180°) in the prone position with carbon ion pencil beam scanning for pancreatic cancer[185]. CTV or GTV coverage among the 7 beams did not widely differ. Dose to the descending duodenum were high with 45° and 90°, but lower for the ascending duodenum compared to the 180° beam. 20° and 315° seemed to be better for the stomach. Some facilities add a rotating couch to up to 45° as a non-gantry solution[186]. The addition of a 45° beam to the 90° beam in our study would allow for variability in the couch rotation, while keeping the value of a vertical beam.

The current study attempts to answer a different question using a carbon ion system with 360 degrees as the reference, which is the potential to mitigate or eliminate the dosimetric disparity with optimized combination of the fixed beam and couch angles. Although the combination has a relatively limited solution space compared with a full gantry system, it still includes more than a hundred available beam directions for optimization.

To achieve the optimization goal, we exploited the couch rotation freedom with an automated IMCT BOO method.

5.1.2 Methods

5.1.2.1 Beam Geometry

The gantry-based plan starts with 1162 non-coplanar beams uniformly distributed across the 4π steradians with 6° separation between adjacent beams combining the gantry and couch rotational degrees-of-freedom. Beam screening is performed to remove beams with infeasible energies or impractical entries into the body, such as those going through the head or feet, leaving 420 beams in the candidate set. For the fixed-beamline plans, we select by hand a total of 90 beams, 30 from the 90° gantry angle, and 60 from the 45° angle. From this, we compared plans with no couch kick against plans with couch angles ranging from 0° to 360° with 6° interval. Note that the possible gantry angles for fixed beam plans, with couch rotation (FBCR) and without (FB), are not an exact subset of the angles for the gantry couch rotation (GCR) plan as shown in Figure 5-1 due to discretization and finite spacing between beams.

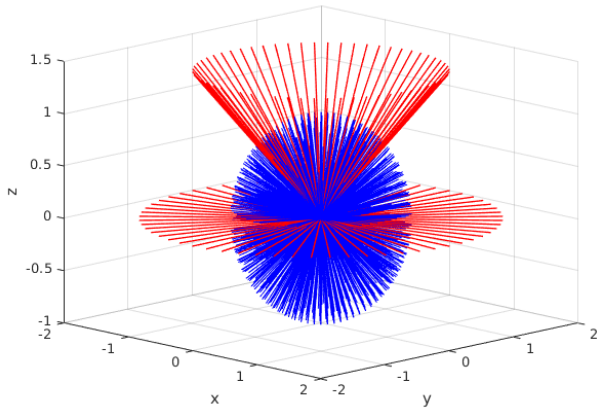

Figure 5-1. Candidate beams for gantry-based plan (blue) and fixed-beamline plan (red). The gantry-based plan includes 1162 non-coplanar beams uniformly distributed, while the fixed-based plan includes 60 couch angles each from the 45° and 90° polar angles.

For each candidate beam, carbon ion pencil beam dose calculation for the scanning spots covering the PTV and a 5mm margin was performed using matRad. The physical dose calculation matrix A, which includes all candidate beams, was generated in this calculation, with an isotropic resolution of 2.5 mm, along with α and β matrices for carbon ion, characterizing the radiosensitivity of the tissue based on the linear quadratic model for survival fraction. Our optimization was formulated to select one or two beams from the candidate beam pool.

5.1.2.2 Beam Orientation Optimization

Beam orientation optimization was performed for both GCR and FBCR plans using the physical dose in the dose fidelity, described in Equation 5-1.

$$\boldsymbol{\Gamma}(\boldsymbol{Ax}) = \sum_{\boldsymbol{i}\in\boldsymbol{\mathcal{T}}} \boldsymbol{\omega_i} \left\|\boldsymbol{A_i x} - \boldsymbol{q_i}\right\|^2 + \sum_{\boldsymbol{i}\in\boldsymbol{\mathcal{O}}} \boldsymbol{\omega_i} \left\|\boldsymbol{A_i x} - \boldsymbol{m_i}\right\|_+^2$$

Equation 5-1

Once a fluence map was obtained, the plans were weighted with RBE values calculated for each structure k from the α and β matrices, using Equations 5-2 and 5-3[187]:

$$-\ln(S) = (\beta_C D_C + \alpha_C) D_C$$

Equation 5-2

$$D_{bio} = \sqrt{-\frac{\ln(S)}{\beta_x} + \left(\frac{\alpha_x}{2\beta_x}\right)^2} - \frac{\alpha_x}{2\beta_x}$$

Equation 5-3

where D_C is fractional carbon physical dose, α_x and β_x are biological parameters of the LQ model for photon as a reference radiation and α_C and β_C are the parameters for carbon ion. For pancreatic cancer, α_x is 0.015 Gy^{-1} and β_x is 0.0016 Gy^{-2}.[188] For the gastrointestinal tract and spinal cord, respectively, α_x values are [0.087, 0.0445] Gy^{-1} and β_x values are [0.013, 0.0135] Gy^{-2}.[189]

The weighting hyperparameter for the group sparsity term was set high such that most of the candidate beams were turned off, leaving only one or two beams active. Weighting for group sparsity was turned off for further fluence map optimization.

Carbon ion BOO was performed to generate a plan with acceptable dosimetry. FISTA was used as the solver for this problem.

5.1.2.3 Patient Evaluations

We compared the GCR, FB, and the proposed FBCR method for ten pancreatic cases initially planned for photon radiotherapy. The original prescription dose was 33 Gy with selective simultaneous integrated boost (SIB) dose to 40 and 50 Gy. Since the prescription dose is not used for carbon ion and the purpose of the study was not to compare with the

photon doses, all plans were prescribed to a total dose of 52.8 GyRBE in 12 fractions[190]. The goal for the PTV dose was to cover 90% of the PTV with 95% of the prescription dose. The target volumes and average spot count per beam for each patient are shown in Table 5-1. For all plans, biological dose (GyRBE) was evaluated. Similar structure weighting was used across plans to ensure unbiased comparison. For each pancreatic case, PTV homogeneity, D95%, and mean dose to the PTV, as well as the maximum dose received by 2cc of the stomach, bowel and duodenum was evaluated. The PTV HI was defined as D95%/D5%. The mean and maximum doses for OARs were also evaluated. The upper clinical goal for all gastrointestinal tract (GI) organs was 46 GyRBE. Maximum dose to the spinal cord limit was 30 GyRBE[190].

Case	PTV Volume (cc)	Average Number of Spots per Beam
A	50.4	2044
B	128.2	4538
C	48.9	2037
D	41.0	1737
E	99.2	3475
F	268.0	7937
G	8.7	562
H	62.2	2393
I	91.3	3317
J	60.1	2309

Table 5-1. PTV volumes, and average number of spots per beam for each case.

5.1.3 Results

5.1.3.1 Runtime and Optimization of Beams

The dose calculation and optimization processes were performed on an 8-core CPU workstation. To calculate the dose and biological parameter matrices for all candidate beams for each approach, the MATLAB Parallel Computing Toolbox was used to accelerate the computation. The times spent on dose calculation and BOO are listed in Table II along with the gantry and couch angles chosen during beam selection. Since the number of candidate beams for the fixed beam approaches were significantly reduced, dose calculation time was cut down by a factor of about 5. The FBCR plans have the potential to reduce beam orientation and fluence map optimization times with the pancreatic cases. For difficult FBCR plans, optimization may require a larger regularization parameter for the group sparsity term and possibly more time than a GCR plan to force convergence from 90 beams to only one or two beams while maintaining dosimetric integrity. While the addition of more beams will reduce the effort, we require that all plans select 1-2 beams for ease of delivery and comparison. In general, total effort for GCR plans takes on average 28 more minutes than FBCR plans. FBCR only takes about 30 more seconds compared to FB to select beams.

	Dose Calculation Time, BOO Time (min)			Beams Selected (gantry, couch)		
	GCR	FBCR	FB	GCR	FBCR	FB
A	15.5 2.9	3.1 2.0	3.1 1.2	(210,39) (140,29)	(45,246) (90,222)	(45,0) (90,0)

B	55.1	12.1	12.1	(140,331)	(45,54)	(45,0)
	6.6	3.0	2.8	(35,33)	(45,174)	(90,0)
C	14.0	2.8	2.8	(205,46)	(45,276)	(45,0)
	2.3	2.5	1.1	(25,346)	(90,222)	(90,0)
D	14.5	2.9	2.9	(54,0)	(45,114)	(45,0)
	2.4	0.9	0.8	(322,340)	(45,354)	(90,0)
E	36.3	7.6	7.6	(25,314)	(45,78)	(45,0)
	5.2	3.9	2.1	(149,348)	(45,294)	(90,0)
F	117	19.0	19.0	(135,26)	(45,258)	(45,0)
	12.9	5.6	5.4	(220,331)	(90,42)	(90,0)
G	5.6	1.1	1.1	(153,332)	(45,126)	(45,0)
	0.5	0.3	0.4	(315,334)	(45,144)	(90,0)
H	29.9	6.3	6.3	(125,345)	(90,215)	(45,0)
	3.0	2.9	1.9	(198,270)	(90,330)	(90,0)
I	28.7	6.8	6.8	(330,39)	(45,198)	(45,0)
	4.9	2.8	2.1	(161,288)	(45,276)	(90,0)
J	17.3	4.0	4.0	(155,346)	(45,342)	(45,0)
	2.6	1.4	1.2	(347,333)	(90,138)	(90,0)

Table 5-2. Dose calculation and optimization times (minutes) with beam angles (degrees) selected for each plan. For GCR plans, both gantry and couch angles were determined by the BOO algorithm. For FBCR plans, couch angles were determined by BOO, and for FB plans, both beams were fixed.

5.1.3.2 Dose Comparison

The optimized FBCR delivery is compared with the GCR and FB deliveries. An isodose comparison in the transverse, coronal, and sagittal planes can be viewed in Figure 5-2. Overall, PTV coverage and OAR sparing varies between plans. A dose-volume histogram representing patient F is shown in Figure 5-3 to compare biological dose structure-by-structure.

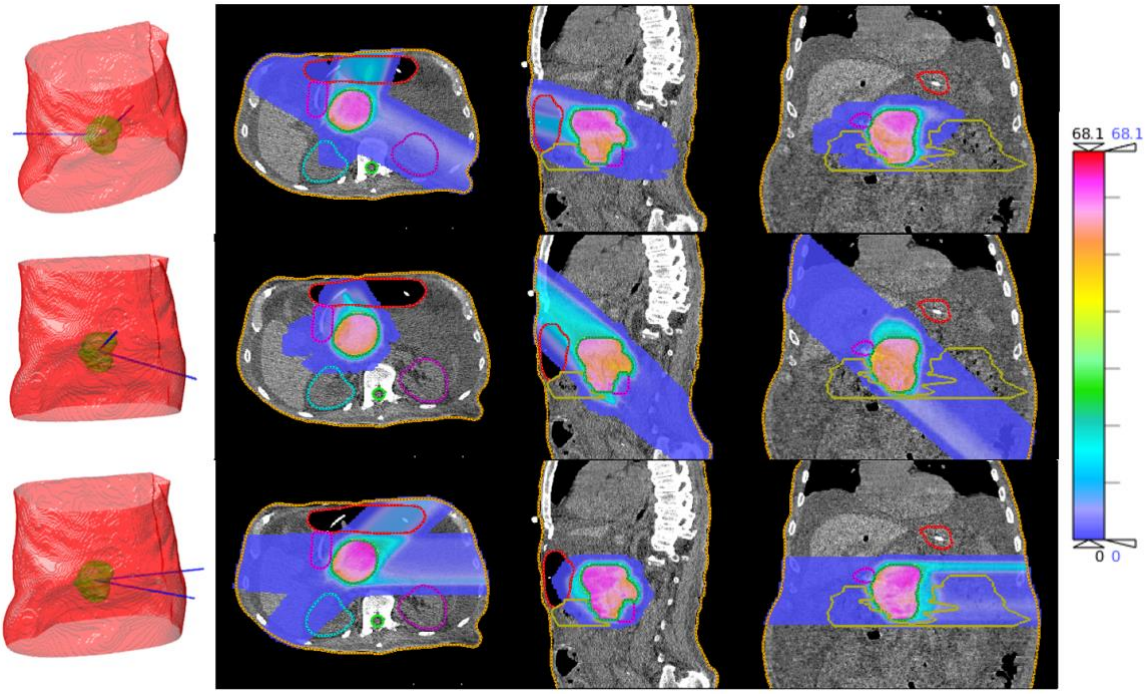

Figure 5-2. Beam orientation along with isodose comparison between GCR (top), FBCR (middle), and FB (bottom) plans for pancreas patient F.

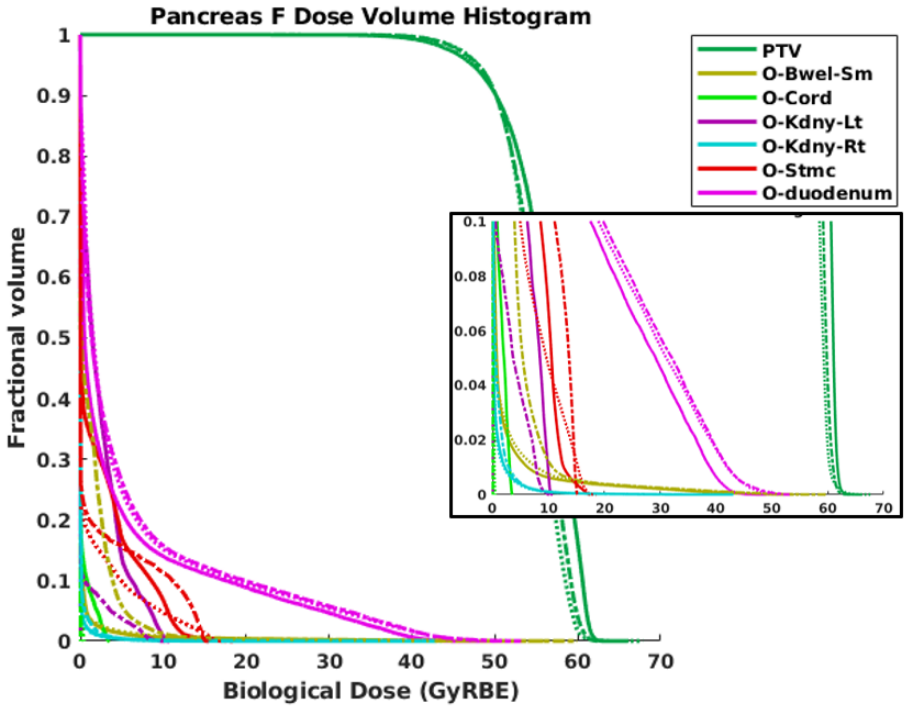

Figure 5-3. Dose-volume histogram (GyRBE) for pancreas patient F. Solid lines represent GCR, dotted lines represent FBCR, and dashed lines represent FB.

Figure 5-4 shows PTV HI, mean, and maximum biological dose to the PTV for all plans. PTV coverage was significantly better with GCR and FBCR compared to FB. Paired t-test was performed between GCR and FBCR, showing p-values of [0.19, 0.29, 0.12] for HI, mean, and maximum biological dose, respectively. The result indicates that the PTV metric differences are statistically insignificant between GCR and FBCR. On the other hand, the comparison between FBCR and FB had p-values of [0.02, 0.02, 0.35], indicating significantly higher HI and mean PTV doses with FBCR. Table 5-3 lists OAR statistics for the gastrointestinal tract and spinal cord, which are lowest, in general, with the GCR plan. In all plans in which GCR met the clinical standard of less than 46 GyRBE to the GI tract, FBCR was able to do so as well. Compared with FB plans, FBCR reduced bowel, duodenum, and stomach doses by [27%, 12%, 23%] and GCR reduces the doses by [35%, 16%, 43%]. P-values for bowel, duodenum, and stomach were [0.02, 0.16, 0.05] between GCR and FBCR and [0.07, 0.33, 0.12] between FBCR and FB, showing mostly minor improvements in dose from FB to FBCR and from FBCR to GCR. For liver and kidneys, mean dose difference between all plans is less than 1 GyRBE. All plans met the clinical limit of 30 GyRBE for the maximum dose to the spinal cord. We have shown a significant improvement of FBCR over FB plans. The OAR sparing gains by FBCR were [77%, 75%, 53%] of that by GCR for the bowel, duodenum, and stomach, respectively.

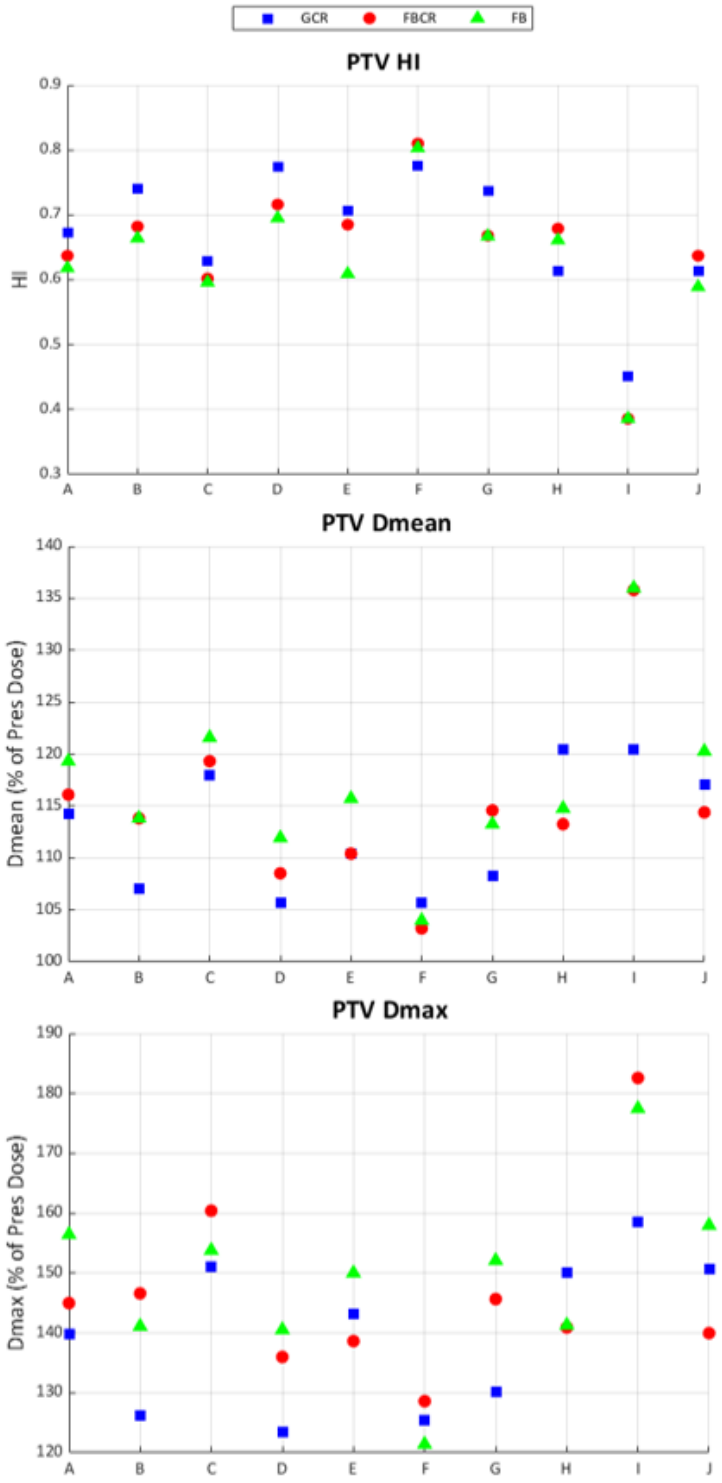

Figure 5-4. PTV statistics for all pancreatic cases. Dmax and Dmean are biological dose values represented as a percentage of the prescribed dose to the PTV volume.

	Structure	GCR	FBCR	FB
A	Bowel	**3.5**	7.1	13.7
	Duodenum	**1.0**	2.6	3.1
	Stomach	**0.2**	0.6	3.9
	Spinal Cord	5.8	0.2	**0.1**
B	Bowel	**0.1**	0.8	10.4
	Duodenum	**36.0**	40.0	37.4
	Stomach	**0.1**	**0.1**	**0.1**
	Spinal Cord	1.9	**0.1**	**0.1**
C	Bowel	**0.1**	**0.1**	**0.1**
	Duodenum	**40.8**	43.0	42.4
	Stomach	**0.3**	0.8	4.7
	Spinal Cord	9.6	**0.1**	**0.1**
D	Bowel	**0.1**	**0.1**	**0.1**
	Duodenum	5.1	**2.9**	4.9
	Stomach	0.2	**0.1**	0.3
	Spinal Cord	**0.1**	**0.1**	**0.1**
E	Bowel	**6.1**	9.3	13.7
	Duodenum	24.4	**24.0**	24.6
	Stomach	**25.0**	27.4	27.6
	Spinal Cord	14.5	**0.1**	**0.1**
F	Bowel	**31.7**	34.2	35.2
	Duodenum	**34.1**	36.5	37.2
	Stomach	15.1	16.2	**14.9**
	Spinal Cord	3.6	**0.1**	**0.1**
G	Bowel	0.4	**0.1**	4.6
	Duodenum	**7.6**	8.6	12.9
	Stomach	**0.7**	2.2	4.6
	Spinal Cord	2.1	**0.1**	**0.1**
H	Bowel	49.1	49.6	**47.8**
	Stomach	**0.3**	1.4	0.7
	Spinal Cord	5.5	**0.1**	**0.1**
I	Bowel	**25.5**	30.0	28.6
	Stomach	**6.8**	12.5	22.3
	Spinal Cord	11.7	0.3	**0.1**
J	Bowel	**28.5**	28.9	30.4
	Duodenum	**12.4**	**12.4**	13.3
	Stomach	**0.1**	**0.1**	**0.1**
	Spinal Cord	11.1	**0.1**	**0.1**

Table 5-3. OAR dose results for the pancreatic cases. Maximum biological dose received by 2cc (D2cc) of bowel, duodenum, and stomach and maximum biological dose (Dmax) to spinal cord are reported in GyRBE.

5.1.4 Discussion

We performed the study to investigate the dosimetric implications of fixed beamlines vs. gantry IMCT plans for the pancreatic cancer treatment. We adopted our previously published beam orientation optimization method to solve a new problem, which is the carbon ion beam orientation optimization with fixed beamlines. The new problem can be considered a subproblem of the full BOO problem with limited degrees of freedom. The additional degree of freedom reduced the gap in solution spaces between the gantry and fixed beamline plans. The large solution space precludes effective manual beam orientation selection. We solved the integrated BOO and scanning spot optimization problems using group sparsity regularization for both the GCR and FBCR plans. We showed that the dosimetric difference between gantry and fixed beamline IMCT may be substantially narrowed if the couch rotation can be fully exploited by solving the optimization problem.

In this study, we specifically choose 45° and 90° polar beamlines for our fixed-beam approach. While it is possible that changing the combination of beamline angles may result in tumor coverage and normal tissue sparing, this effect can dependent on patient characteristics and local anatomy configurations. In theory, 90° beam allow sampling of the most widespread of the spherical space in combination with the couch rotation. Smaller angles would reduce the radiological path lengths for oblique beams, but too small a polar angle would result in a collapsed cone and degenerated solution space. Therefore, the 45°-90° orientations seem to be a well-balanced and generalizable combination. A rigorous

conclusion for the fixed-beamline orientation selection problem needs to be drawn based on a statistical analysis of the dosimetry for many more patient types and cases.

Besides limited patient cases, another limitation is that geometrically undesired beams and beams of infeasible energies were only partially excluded from the 1162-beam candidate set. These beams with long radiological pathlength are eliminated in BOO due to undesired geometry. Simulations that model three-dimensional collisions of large gantries with the patient and couch for different treatment zones have been performed for proton[191], but to our knowledge, no studies of this kind have yet been published for carbon ion gantries. Once carbon beam log data is available, more accurate beam screening should be performed for carbon gantries to assess the impact on beam selection and resulting dosimetry.

Solutions to the problem of having limited beam angles with fixed beamlines for carbon ion include rotating the couch along the long axis[192]. Couch rotation is commonly used in clinical practice. With robotic couch, sub-millimetre movement accuracy has been demonstrated[193]. However, the couch motion may increase the probability of patient shift, which can be managed by immobilization and surface, X-ray, and tomographic imaging monitoring.

Due to the prohibitively long time required to calculate dose for 1162 candidate beams using Monte Carlo, the current study uses an analytical method, which is acceptable for dose comparison, but may have inaccuracies for further studies with biological objective functions, especially for carbon ion studies, due to its inability to account for fragmentation or secondary particles[194,195]. Either fast CPU- or GPU-based Monte Carlo for

carbon-ion radiation therapy may be better suited for that goal[196,197]. Physical dose conformality is our current optimization objective with an estimate of variable RBE applied. This is likely an oversimplification for the carbon ion beams. Because of the drastic changes in RBE along the beam path, different beams may be selected if more accurate RBE is modelled within the BOO problem. For instance, RBE-weighted dose using the local effect model (LEMIV), repair-misrepair-fixation (RMF) model, or microdosimetric kinetic model (MKM)[79,198], can be used to explore the effectiveness of a biological dose optimization framework with the fixed beamline approach.

5.1.5 Conclusions

We show that the dosimetry compromise due to the fixed beamlines vs. a full gantry for carbon-ion therapy can be largely mitigated for pancreatic cases with the beam orientation optimization exploiting the couch rotation freedom. With further investigation on other disease sites, this work indicates the potential to significantly simplify gantry design for carbon-ion therapy, thus overcoming a major hurdle in availing this technology.

6 APPENDIX

6.1 Fast Iterative Shrinkage Thresholding Algorithm (FISTA)

The FISTA algorithm is an accelerated version of the proximal gradient method (also known as the forward-backward method). It solves optimization problems of the form

$$minimize\ F(x) + G(x)$$

Equation 6-1

F is assumed to be a closed convex function that is differentiable with a Lipschitz continuous gradient. G is should have a proximal operator that can be evaluated efficiently. For function F, FISTA must calculate the gradient, which for the following functions, can be evaluated using simple calculus. Equation 6-2 covers the general set of terms used in the beam orientation optimization framework.

1. If $F(x) = \frac{1}{2}\|x\|_2^2$, then $\nabla F(x) = x$.
2. If $F(x) = \frac{1}{2}\|x_+\|_2^2$, then $\nabla F(x) = x_+ = \max(x, 0)$, where the maximum is taken component wise.
3. If $F(x) = \frac{1}{2}\|x\|_1^{(\mu)}$, called the Huber penalty, then $\nabla F(x) = \frac{1}{\mu}P_{[-\mu,\mu]}(x)$, where $P_{[-\mu,\mu]}(x)$ represents the projection of x onto the set $\{u \mid -\mu \leq u \leq \mu\}$.

The proximal operator, with step size parameter $t > 0$, is calculated efficiently using Equation 6-2.

$$prox_{tf}(x) = \underset{u}{argmin}\, f(u) + \frac{1}{2t}\|u - x\|_2^2$$

Equation 6-2

The most commonly used term for G is the L2,1/2-norm group sparsity term $\psi(x) = \|x\|_2^{1/2}$, whose proximal operator is defined in Equation 6-3. The full derivation can be found in the publications by O'Connor et al[199].

$$prox_{t\psi}(x) = \begin{cases} \frac{2}{\sqrt{3}}\sin\left(\frac{1}{3}arccos\left(\frac{3\sqrt{3}}{4}\frac{t}{\|x\|_2^{\frac{3}{2}}}\right) + \frac{\pi}{2}\right), if\ \frac{t}{\|x\|_2^{\frac{3}{2}}} \leq \frac{2\sqrt{6}}{9} \\ 0, otherwise \end{cases}$$

Equation 6-3

The FISTA algorithm with line search is found in Algorithm 6-1 below.

Algorithm 6-1 FISTA with line search

Initialize x_0 and $t_0 > 0$, set $v_0 \coloneqq x_0$, set $0 < r < 1$, and $s > 1$
for $k = 1, 2, \ldots$ **do**
  $t \coloneqq st_{k-1}$
  repeat
    $\theta \coloneqq \begin{cases} 1 & if\ k = 1 \\ positive\ root\ of\ t_{k-1}\theta^2 = t\theta_{k-1}^2(1-\theta) & if\ k > 1 \end{cases}$
    $y \coloneqq (1-\theta)x_{k-1} + \theta v_{k-1}$
    $x \coloneqq prox_{tg}\big(y - t\nabla f(y)\big)$
    break if $f(x) \leq f(y) + \langle \nabla f(y), x - y\rangle + \frac{1}{2t}\|x - y\|_2^2$
    $t \coloneqq rt$
  $t_k \coloneqq t$
  $\theta_k \coloneqq \theta$
  $x_k \coloneqq x$
  $v_k \coloneqq x_{k-1} + \frac{1}{\theta_k}(x_k - x_{k-1})$
end for

6.2 Chambolle-Pock Algorithm (CP)

The Chambolle-Pock algorithm solves optimization problems of the form

$$minimize\ F(Kx) + G(x)$$

Equation 6-4

where F and G are simple and convex functions.

The McNamara RBE-guided beam orientation optimization problem is:

$$\underset{x}{\textbf{minimize}}\ \underbrace{\vec{c}x + \|Hx\|_2^2}_{OAR\ RBE\ term} + \underbrace{\left\|RBE \cdot Ax - d_{pres}\right\|_2^2}_{Static\ RBE\ dose\ for\ CTV} + \underbrace{\sum_{b\in\beta} \alpha_b h_b \|x_b\|_2^{\frac{1}{2}}}_{group\ sparsity\ term} + \underbrace{\sum_{k\in\{u,v\}} \lambda_k s_k^T x}_{sensitivity\ term}$$
$$\textbf{subject to } x \geq 0$$

Equation 6-5

For this substitution, we keep in mind that the OAR RBE term is minimized to 0 while the CTV physical dose, assuming a static RBE optimized from a previous physical dose calculation, is optimized to the prescription dose. These two terms, along with the sensitivity term, are grouped into function F. The group sparsity term and the non-negativity constraint become members of function G. We can define

$$G(x) = w\|x\|_2^{\frac{1}{2}} + I_+(x)$$

Equation 6-6

$$K = \begin{bmatrix} c^T \\ H \\ A \\ s \end{bmatrix}$$

Equation 6-7

Using Moreau decomposition and separable sums, we can separate the F(Kx) calculation.

$$M\left(\begin{bmatrix} y_1 \\ y_2 \\ y_3 \\ y_4 \end{bmatrix}\right) = F_1(y_1) + F_2(y_2) + F_3(y_3) + F_4(y_4)$$

Equation 6-8

$$F_1(y_1) = y_1$$

$$F_2(y_2) = \|y_2\|_2^2$$

$$F_3(y_3) = \|y_3 - d\|_2^2$$

$$F_4(y_4) = \sum_k y_{4,k}$$

Equation 6-9

$$\text{prox}_{\sigma F^*}\left(\begin{bmatrix} y_1 \\ y_2 \\ y_3 \\ y_4 \end{bmatrix}\right) = \begin{bmatrix} \text{prox}_{\sigma F_1^*}(y_1) \\ \text{prox}_{\sigma F_2^*}(y_2) \\ \text{prox}_{\sigma F_3^*}(y_3) \\ \text{prox}_{\sigma F_4^*}(y_4) \end{bmatrix}$$

Equation 6-10

The proximal gradients can then be substituted into lines 2 and 7 of Algorithm 6-2.

Algorithm 6-2 Chambolle-Pock primal-dual algorithm with line search

1 Initialize $x^0 \in X,\ y^1 \in Y, t_0 > 0, \mu \in (0,1), \delta \in (0,1), and\ \beta > 0$. Set $\theta_0 = 1$.
2 **for** $k = 1, 2, \ldots$ **do**
3 Compute $x^k = prox_{t_{k-1}G}(x^{k-1} - t_{k-1}K^* y^k)$
4 Choose any $t_k \in [t_{k-1}, t_{k-1}\sqrt{1 + \theta_{k-1}}]$
5 **while 1**
6 Compute $\theta_k = \frac{t_k}{t_{k-1}}$
7 Compute $\bar{x}^k = x^k + \theta_k(x^k - x^{k-1})$
8 Compute $y^{k+1} = prox_{\beta t_k F^*}(y^k + \beta t_k K \bar{x}^k)$
9 **if** $\sqrt{\beta} t_k \|K^* y^{k+1} - K^* y^k\| \leq \delta \|y^{k+1} - y^k\|$
10 **break**
11 **else**
12 $t_k \coloneqq t_k \mu$
13 **end**
14 **end**
15 **end**

6.3 Split-Bregman Algorithm (SB)

When discussing the reformulated McNamara dose optimization in Equation 6-5, the McNamara RBE in the CTV term was calculated from a previous physical dose optimization. However, the McNamara RBE is dependent on dose, which itself is dependent on the optimization variable x. Since the previous calculation was introduced into this problem, the descent to find true RBE values may not be the same as the descent that solves Equation 2-1.

Essentially, the RBE-weighted dose optimization problem can be simplified to the following:

$$\left\| RBE(d) \cdot d - d_{pres} \right\| + f(d)$$

Equation 6-11

Here, Ax is replaced with d as simplification, and we assume for now that the only term included in f(d) is the group sparsity term (without heterogeneity weighting or sensitivity regularization). The first term covers the McNamara dose fidelity in both CTVs and OARs.

Suppose we split this problem so that the first and second terms in Equation 6-11 utilize different fluence maps (or different doses d_1 and d_2). Provided that $d_1 = d_2$, Equation 6-11 and Equation 6-12 are the same problem.

$$\underbrace{\left\| RBE(d_1) \cdot d_1 - d_{pres} \right\| + f(d_2)}_{provided\ that\ d1=d2}$$

Equation 6-12

If d_1 and d_2 are not quite equal ($d_1 \approx d_2$), a term may be added to force equality.

$$\left\|RBE(d_1)\cdot d_1 - d_{pres}\right\| + f(d_2) + \mu\|d_1 - d_2\|$$

Equation 6-13

When mu approaches infinity, d_1 and d_2 are more equal. With Equation 6-13, we have a formulation that can be solved by hybrid block descent or hybrid minimization. Using two optimization variables, one can be held constant while the other is optimized, moving in either small, controlled steps or large ones towards an optimal solution, as long as there is gradient descent. In the end, the two fluence maps will be similar to each other depending on how gamma is tuned, and either may be used for final RBE calculation and fluence map optimization steps.

Now that we have a formula that looks like $F(\begin{bmatrix} d_1 \\ d_2 \end{bmatrix})$, we separate the partial derivatives.

$$\frac{\partial F}{\partial d_1} = \frac{\partial}{\partial d_1}\left\|RBE(d_1)\cdot d_1 - d_{pres}\right\| + \frac{\partial}{\partial d_1}\gamma\|d_1 - d_2\|$$

$$\frac{\partial F}{\partial d_2} = \frac{\partial}{\partial d_2} f(d_2) + \frac{\partial}{\partial d_2}\gamma\|d_1 - d_2\|$$

Equation 6-14

In the first part (block I), $d_2$is held constant and in the second (block II), d_1 is held constant, but they are coupled. Blocks 1 and 2 can both be solved with proximal gradient algorithms like FISTA. More blocks can be added to solve any other constraints within the problem, using proximal operators, etc.

The normoxic or hypoxic RBE-weighted BOO can be solved using the split-Bregman approach that has been described, where the biological dose fidelity terms (block I, solved

by variable x) are separated from the beam-regulating group sparsity term (block II, solved by variable z). Fluence map variables x and z are pre-defined as randomized vectors and an initial RBE vector is calculated from x. Then, block I, defined as the biological dose fidelity terms plus the equality constraint loosely minimizing the difference between variable x and constant z is solved using FISTA. Optimization of block II, defined as the group sparsity term plus an equality constraint minimizing the difference between variable z and constant x, is then performed with FISTA. The cycle repeats as the two blocks are alternately solved with periodic RBE re-calculation using the normoxic McNamara model, or the hypoxia informed RBE model for dose weighting. Algorithm 6-3 shows the splitting scheme line-by-line. The relationship between optimization variables x and z are controlled by weight coefficient μ. At first, μ is small ($<10^{-4}$) to get rid of beams that do not aid the fluence map in reaching the dosimetry goals. As $\mu \to \infty$, the solutions x and z should be the same. Robustness can be simply added as a heterogeneity weighting on the group sparsity term and sensitivity regularization added as another parameter.

Algorithm 6-3 Split Bregman for Group Sparsity BOO

1 Initialize A, q, m, x^0, z^0, set $b^0 = 0$.

2 **for** $k = 1, 2, \ldots$ **do**

3 Calculate $RBE^k(x^k)$ using Equation 3-1 with normoxic or hypoxic α_p or β_p values.

4 $x^{k+1} = \underset{x}{\operatorname{argmin}} \sum_{i\in\tau} \omega_i \left\| RBE_i^k \cdot A_i x - q_i \right\|_2^2 + \sum_{i\in o} \omega_i \left\| m_i - RBE_i^k \cdot A_i x \right\|_2^2 + \mu \left\| z^k - x - b^k \right\|_2^2$

5 $z^{k+1} = \underset{z}{\operatorname{argmin}} \sum_{b\in B} c_b \|z_b\|_2^{\frac{1}{2}} + \mu \left\| z - x^{k+1} - b^k \right\|_2^2$

6 Calculate $b^{k+1} = b^k + (x^{k+1} - z^{k+1})$

7 **end for**

6.4 A path-seeking gradient descent algorithm (PathGD)

Despite BOO being a highly nonconvex problem, it was solved efficiently using the FISTA with a convergence rate of $O(1/k^2)$. Because FISTA involved simple matrix-vector operations with proximal operator calculations, the optimization runtime for selecting a known number of fields was a major attraction for a problem with large dose-calculation matrices.

An overlooked yet practically relevant factor, however, is the laborious tuning of parameter c in Equation 1-4 to achieve acceptable convergence speed, a desired beam number (for proton, 2-4 beams, and for carbon ion, only 1-2), and satisfactory plan quality. If c is too high for proton planning, the algorithm would eliminate several beams in the same iteration, prohibiting interpretation of the differences between beam numbers, particularly in the 1-10 beam range. If c is too low, the algorithm would take hundreds of extra iterations to eliminate beams down to 4 or fewer, unnecessarily adding to optimization runtime. Although not explicitly reported, this tuning step would add substantial planning time (>1 hour), and inconsistency that depends on the planner's experience.

To avoid this tuning, we developed a gradient descent method with beam fitness calculation. This is a path-seeking algorithm that pairs each set of beams (found via beam fitness calculation) with their resulting dosimetry (determined via gradient descent). We termed this method "PathGD," detailed in Algorithm 6-4. Here, we propose to remove the group sparsity term and optimize the fluence map via gradient descent for one, two, three, etc., active beams at a time, where the beams are added to be optimized if they have the

highest beam fitness. First, the loss function $f(x)$ is defined as an approximation of the dose fidelity term. Next, we calculate the gradients of $f(x)$ for the current fluence map x. The gradients represent the direction of the steepest descent towards a local minimum. For the initial fluence map, $x = 0$, the gradient calculation is solely based on the CTV prescription doses q_i and the desired doses in the OARs m_i. The first beam that is activated is chosen by defining a fitness term M_b for each inactive beam b, equal to the sum of negative gradients of all spots (proton) or beamlets (photon) in the beam. Since fluence map intensities cannot be negative and are truncated later in the algorithm, only the negative part of the gradient descent is counted toward the fitness, with $g^- = -\min(g, 0)$. Once each beam is activated, the algorithm performs gradient descent for that activated set. Here, the gradients are again calculated for the current fluence map x, and then the fluence map is iteratively updated to represent a step towards the local minimum of the loss function. The step size is controlled by s, which is one of two parameters that must be tuned in the algorithm. The other is the threshold that determines when a new beam should be added. When the loss no longer decreases by threshold $t > 0$, each element of M (M_b, the overall descent for each beam b) is calculated. In other words, if we cannot improve the fluence map given the currently activated beams, a new beam with the largest fitness is activated. For our proton and photon planning, step size $s \in [10^{-3}, 10^{-2}]$ and threshold $t \cong 0.9999$ were held constant throughout each optimization. For the FISTA algorithm with line search, four tuning parameters, including step size and group sparsity weighting, must be manually tuned.

Algorithm 6-4 PathGD

- **Inputs**: f: linearized loss function, s: step size, β: active set of beams, t: threshold, $addBeam = 0$
- **Output**: x: parameter weights for the solution

Set $x^0 = 0$ and $\Delta x = 0$.

for $k = 1, 2, \ldots$ **do**

    Calculate $g = \frac{df}{dx}|_{x=x^k}$.

    if $addBeam$ **then**

        Calculate fitness $M_b = \sum_{j \in b} g_j^-$ for $b \notin \beta$.

        Find beam with highest fitness, $b_{new} = argmax_b M$.

        $\Delta x_{j \in b_{new}} = g_{j \in b_{new}}$

        $addBeam = 0$

    else

        $\Delta x_{j \in \beta} = g_{j \in \beta}$

    end if

    Update the parameters $x^{k+1} = x^k - s\Delta x$.

    If $x_j^{k+1} < 0 : \ x_j^{k+1} = 0$.

    If $f(x^{k+1}) > tf(x^k)$: $addBeam = 1$.

end for

Algorithm 6-5 Modified PathGD with Voxel Repetition Penalization

- **Inputs**: f: loss function, s: step size, β: active set of beams, t: threshold, $addBeam = 0$
- **Output**: x: parameter weights for the solution

Set $x^0 = 0$ and $\Delta x = 0$.

for $k = 1, 2, \ldots$ **do**

  Calculate $g = \frac{df}{dx}|_{x=x^k}$.

  Calculate $g_{VR} = g + \frac{d}{dx}|_{x=x^k} \left(w_q \left\| \left(\sum_{b=1}^{B} \sigma \left(\left(A_q (x^k - sg) \right)_b \right) - 1 \right)_+ \right\|_2^2 \right)$.

  if $addBeam$ **then**

    Calculate fitness $M_b = \sum_{j \in b} g_{\overline{VR},j}$ for $b \notin \beta$.

    Find beam with highest fitness, $b_{new} = argmax_b M$.

    $\Delta x_{j \in b_{new}} = g_{VR, j \in b_{new}}$

    $addBeam = 0$

  else

    $\Delta x_{j \in \beta} = g_{VR, j \in \beta}$

  end if

  Update the parameters $x^{k+1} = x^k - s\Delta x$.

  If $x_j^{k+1} < 0 : \; x_j^{k+1} = 0$.

  If $f(x^{k+1}) > tf(x^k)$: $addBeam = 1$.

end for

7 REFERENCES

1. Liu H, Chang JY. Proton therapy in clinical practice. *Chin J Cancer*. 2011;30(5):315-326. doi:10.5732/cjc.010.10529
2. Wilson RR. Radiological use of fast protons. *Radiology*. 1946;47(5):487-491. doi:10.1148/47.5.487
3. Berman A, St. James S, Rengan R. Proton Beam Therapy for Non-Small Cell Lung Cancer: Current Clinical Evidence and Future Directions. *Cancers*. 2015;7:1178-1190. doi:10.3390/cancers7030831
4. Kanai T, Kawachi K, Kumamoto Y, et al. Spot scanning system for proton radiotherapy. *Med Phys*. 1980;7(4):365-369. doi:10.1118/1.594693
5. Lomax A. Intensity modulation methods for proton radiotherapy. *Phys Med Biol*. 1999;44(1):185-205. doi:10.1088/0031-9155/44/1/014
6. Tommasino F, Durante M. Proton radiobiology. *Cancers*. 2015;7(1):353-381. doi:10.3390/cancers7010353
7. Park JM, Kim JI, Wu HG. Technological Advances in Charged-Particle Therapy. *Cancer Res Treat*. 2021;53(3):635-640. doi:10.4143/crt.2021.706
8. Paganetti H. Relative biological effectiveness (RBE) values for proton beam therapy. Variations as a function of biological endpoint, dose, and linear energy transfer. *Phys Med Biol*. 2014;59(22):R419. doi:10.1088/0031-9155/59/22/R419

9. Alizadeh E, Orlando TM, Sanche L. Biomolecular damage induced by ionizing radiation: the direct and indirect effects of low-energy electrons on DNA. *Annu Rev Phys Chem*. 2015;66:379-398. doi:10.1146/annurev-physchem-040513-103605
10. Underwood TSA, McNamara AL, Appelt A, Haviland JS, Sørensen BS, Troost EGC. A systematic review of clinical studies on variable proton Relative Biological Effectiveness (RBE). *Radiother Oncol J Eur Soc Ther Radiol Oncol*. 2022;175:79-92. doi:10.1016/j.radonc.2022.08.014
11. Paganetti H, Blakely E, Carabe-Fernandez A, et al. Report of the AAPM TG-256 on the relative biological effectiveness of proton beams in radiation therapy. *Med Phys*. 2019;46(3):e53-e78. doi:10.1002/mp.13390
12. Sethi RV, Giantsoudi D, Raiford M, et al. Patterns of failure after proton therapy in medulloblastoma; linear energy transfer distributions and relative biological effectiveness associations for relapses. *Int J Radiat Oncol Biol Phys*. 2014;88(3):655-663. doi:10.1016/j.ijrobp.2013.11.239
13. Jones B, Wilson P, Nagano A, Fenwick J, McKenna G. Dilemmas concerning dose distribution and the influence of relative biological effect in proton beam therapy of medulloblastoma. *Br J Radiol*. 2012;85(1018):e912-e918. doi:10.1259/bjr/24498486
14. Kanemoto A, Hirayama R, Moritake T, et al. RBE and OER within the spread-out Bragg peak for proton beam therapy: in vitro study at the Proton Medical Research Center at the University of Tsukuba. *J Radiat Res (Tokyo)*. 2014;55(5):1028-1032. doi:10.1093/jrr/rru043

15. Luo WR, Chen FH, Huang RJ, Chen YP, Hsiao YY. Effects of indirect actions and oxygen on relative biological effectiveness: estimate of DSB inductions and conversions induced by therapeutic proton beams. *Int J Radiat Biol*. 2020;96(2):187-196. doi:10.1080/09553002.2020.1688883
16. Wenzl T, Wilkens JJ. Theoretical analysis of the dose dependence of the oxygen enhancement ratio and its relevance for clinical applications. *Radiat Oncol Lond Engl*. 2011;6:171. doi:10.1186/1748-717X-6-171
17. Stasica P, Nguyen H, Granja C, et al. Single proton LET characterization with the Timepix detector and artificial intelligence for advanced proton therapy treatment planning. *Phys Med Biol*. 2023;68(10):104001. doi:10.1088/1361-6560/acc9f8
18. Hirayama R, Ito A, Tomita M, et al. Contributions of direct and indirect actions in cell killing by high-LET radiations. *Radiat Res*. 2009;171(2):212-218. doi:10.1667/RR1490.1
19. Roobol SJ, van den Bent I, van Cappellen WA, et al. Comparison of High- and Low-LET Radiation-Induced DNA Double-Strand Break Processing in Living Cells. *Int J Mol Sci*. 2020;21(18):6602. doi:10.3390/ijms21186602
20. Hageman E, Che PP, Dahele M, Slotman BJ, Sminia P. Radiobiological Aspects of FLASH Radiotherapy. *Biomolecules*. 2022;12(10):1376. doi:10.3390/biom12101376
21. Liu C, Lin Q, Yun Z. Cellular and Molecular Mechanisms Underlying Oxygen-Dependent Radiosensitivity. *Radiat Res*. 2015;183(5):487-496. doi:10.1667/RR13959.1

22. Kim H, Lin Q, Glazer PM, Yun Z. The hypoxic tumor microenvironment in vivo selects the cancer stem cell fate of breast cancer cells. *Breast Cancer Res*. 2018;20(1):16. doi:10.1186/s13058-018-0944-8
23. Chan CC, Chen FH, Hsiao YY. Impact of Hypoxia on Relative Biological Effectiveness and Oxygen Enhancement Ratio for a 62-MeV Therapeutic Proton Beam. *Cancers*. 2021;13(12):2997. doi:10.3390/cancers13122997
24. Tinganelli W, Durante M. Carbon Ion Radiobiology. *Cancers*. 2020;12(10):3022. doi:10.3390/cancers12103022
25. Luo WR, Chen FH, Huang RJ, Chen YP, Hsiao YY. Effects of indirect actions and oxygen on relative biological effectiveness: estimate of DSB inductions and conversions induced by therapeutic proton beams. *Int J Radiat Biol*. 2020;96(2):187-196. doi:10.1080/09553002.2020.1688883
26. Mohamad O, Yamada S, Durante M. Clinical Indications for Carbon Ion Radiotherapy. *Clin Oncol R Coll Radiol G B*. 2018;30(5):317-329. doi:10.1016/j.clon.2018.01.006
27. Raju MR, Amols HI, Bain E, Carpenter SG, Cox RA, Robertson JB. A heavy particle comparative study. Part III: OER and RBE. *Br J Radiol*. 1978;51(609):712-719. doi:10.1259/0007-1285-51-609-712
28. Wenzl T, Wilkens JJ. Modelling of the oxygen enhancement ratio for ion beam radiation therapy. *Phys Med Biol*. 2011;56(11):3251-3268. doi:10.1088/0031-9155/56/11/006
29. Vozenin MC, Hendry JH, Limoli CL. Biological Benefits of Ultra-high Dose Rate FLASH Radiotherapy: Sleeping Beauty Awoken. *Clin Oncol R Coll Radiol G B*. 2019;31(7):407-415. doi:10.1016/j.clon.2019.04.001

30. Hughes JR, Parsons JL. FLASH Radiotherapy: Current Knowledge and Future Insights Using Proton-Beam Therapy. *Int J Mol Sci*. 2020;21(18):6492. doi:10.3390/ijms21186492
31. de Kruijff RM. FLASH radiotherapy: ultra-high dose rates to spare healthy tissue. *Int J Radiat Biol*. 2020;96(4):419-423. doi:10.1080/09553002.2020.1704912
32. Kim MM, Verginadis II, Goia D, et al. Comparison of FLASH Proton Entrance and the Spread-Out Bragg Peak Dose Regions in the Sparing of Mouse Intestinal Crypts and in a Pancreatic Tumor Model. *Cancers*. 2021;13(16):4244. doi:10.3390/cancers13164244
33. Cunningham S, McCauley S, Vairamani K, et al. FLASH Proton Pencil Beam Scanning Irradiation Minimizes Radiation-Induced Leg Contracture and Skin Toxicity in Mice. *Cancers*. 2021;13(5):1012. doi:10.3390/cancers13051012
34. Moon EJ, Petersson K, Oleina MM. The importance of hypoxia in radiotherapy for the immune response, metastatic potential and FLASH-RT. *Int J Radiat Biol*. 2022;98(3):439-451. doi:10.1080/09553002.2021.1988178
35. Lomax AJ, Böhringer T, Bolsi A, et al. Treatment planning and verification of proton therapy using spot scanning: initial experiences. *Med Phys*. 2004;31(11):3150-3157. doi:10.1118/1.1779371
36. Steneker M, Lomax A, Schneider U. Intensity modulated photon and proton therapy for the treatment of head and neck tumors. *Radiother Oncol J Eur Soc Ther Radiol Oncol*. 2006;80(2):263-267. doi:10.1016/j.radonc.2006.07.025
37. Kirkby KJ, Kirkby NF, Burnet NG, et al. Heavy charged particle beam therapy and related new radiotherapy technologies: The clinical potential, physics and technical

developments required to deliver benefit for patients with cancer. *Br J Radiol*. Published online October 6, 2020:20200247. doi:10.1259/bjr.20200247

38. Rocha H, Dias JM, Ferreira BC, Lopes MC. Pattern search methods framework for beam angle optimization in radiotherapy design. *Appl Math Comput*. 2013;219(23):10853-10865. doi:10.1016/j.amc.2013.05.006
39. Gu W, O'Connor D, Nguyen D, et al. Integrated beam orientation and scanning-spot optimization in intensity-modulated proton therapy for brain and unilateral head and neck tumors. *Med Phys*. 2018;45(4):1338-1350. doi:10.1002/mp.12788
40. Gu W, Neph R, Ruan D, Zou W, Dong L, Sheng K. Robust beam orientation optimization for intensity-modulated proton therapy. *Med Phys*. 2019;46(8):3356-3370. doi:10.1002/mp.13641
41. Cisternas E, Mairani A, Ziegenhein P, Jäkel O, Bangert M. matRad - a multi-modality open source 3D treatment planning toolkit. In: Jaffray DA, ed. *World Congress on Medical Physics and Biomedical Engineering, June 7-12, 2015, Toronto, Canada*. IFMBE Proceedings. Springer International Publishing; 2015:1608-1611. doi:10.1007/978-3-319-19387-8_391
42. Wieser HP, Cisternas E, Wahl N, et al. Development of the open-source dose calculation and optimization toolkit matRad. *Med Phys*. 2017;44(6):2556-2568. doi:10.1002/mp.12251
43. Ramesh P, Lyu Q, Gu W, Ruan D, Sheng K. Reformulated McNamara RBE-weighted beam orientation optimization for intensity modulated proton therapy. *Med Phys*. 2022;49(4):2136-2149. doi:10.1002/mp.15552

44. Ramesh P, Ruan D, Liu SJ, Seo Y, Braunstein S, Sheng K. Hypoxia-informed RBE-weighted beam orientation optimization for intensity modulated proton therapy. *Med Phys*. Published online February 12, 2024. doi:10.1002/mp.16978
45. Ramesh P, Gu W, Ruan D, Sheng K. Dose and dose rate objectives in Bragg peak and shoot-through beam orientation optimization for FLASH proton therapy. *Med Phys*. 2022;49(12):7826-7837. doi:10.1002/mp.16009
46. Ramesh P, Valdes G, O'Connor D, Sheng K. A unified path seeking algorithm for IMRT and IMPT beam orientation optimization. *Phys Med Biol*. Published online September 2, 2023. doi:10.1088/1361-6560/acf63f
47. Ramesh P, Liu H, Gu W, Sheng K. Fixed Beamline Optimization for Intensity Modulated Carbon-Ion Therapy. *IEEE Trans Radiat Plasma Med Sci*. 2022;6(3):288-293. doi:10.1109/trpms.2021.3092296
48. Wedenberg M, Lind BK, Hårdemark B. A model for the relative biological effectiveness of protons: the tissue specific parameter α/β of photons is a predictor for the sensitivity to LET changes. *Acta Oncol Stockh Swed*. 2013;52(3):580-588. doi:10.3109/0284186X.2012.705892
49. Carabe-Fernandez A, Dale RG, Jones B. The incorporation of the concept of minimum RBE (RbEmin) into the linear-quadratic model and the potential for improved radiobiological analysis of high-LET treatments. *Int J Radiat Biol*. 2007;83(1):27-39. doi:10.1080/09553000601087176
50. Wilkens JJ, Oelfke U. A phenomenological model for the relative biological effectiveness in therapeutic proton beams. *Phys Med Biol*. 2004;49(13):2811-2825. doi:10.1088/0031-9155/49/13/004

51. McNamara AL, Schuemann J, Paganetti H. A phenomenological relative biological effectiveness (RBE) model for proton therapy based on all published in vitro cell survival data. *Phys Med Biol*. 2015;60(21):8399-8416. doi:10.1088/0031-9155/60/21/8399
52. Bai X, Lim G, Grosshans D, Mohan R, Cao W. A biological effect-guided optimization approach using beam distal-edge avoidance for intensity-modulated proton therapy. *Med Phys*. 2020;47(9):3816-3825. doi:10.1002/mp.14335
53. Deng W, Yang Y, Liu C, et al. A Critical Review of LET-Based Intensity-Modulated Proton Therapy Plan Evaluation and Optimization for Head and Neck Cancer Management. *Int J Part Ther*. 2021;8(1):36-49. doi:10.14338/IJPT-20-00049.1
54. Traneus E, Ödén J. Introducing Proton Track-End Objectives in Intensity Modulated Proton Therapy Optimization to Reduce Linear Energy Transfer and Relative Biological Effectiveness in Critical Structures. *Int J Radiat Oncol Biol Phys*. 2019;103(3):747-757. doi:10.1016/j.ijrobp.2018.10.031
55. Wagenaar D, Tran LT, Meijers A, et al. Validation of linear energy transfer computed in a Monte Carlo dose engine of a commercial treatment planning system. *Phys Med Biol*. 2020;65(2):025006. doi:10.1088/1361-6560/ab5e97
56. Wilkens JJ, Oelfke U. Optimization of radiobiological effects in intensity modulated proton therapy. *Med Phys*. 2005;32(2):455-465. doi:10.1118/1.1851925
57. Gu W, Ruan D, Zou W, Dong L, Sheng K. Linear energy transfer weighted beam orientation optimization for intensity-modulated proton therapy. *Med Phys*. 2021;48(1):57-70. doi:10.1002/mp.14329

58. Giantsoudi D, Sethi RV, Yeap BY, et al. Incidence of CNS Injury for a Cohort of 111 Patients Treated With Proton Therapy for Medulloblastoma: LET and RBE Associations for Areas of Injury. *Int J Radiat Oncol*. 2016;95(1):287-296. doi:10.1016/j.ijrobp.2015.09.015
59. Gutierrez A, Rompokos V, Li K, et al. The impact of proton LET/RBE modeling and robustness analysis on base-of-skull and pediatric craniopharyngioma proton plans relative to VMAT. *Acta Oncol Stockh Swed*. 2019;58(12):1765-1774. doi:10.1080/0284186X.2019.1653496
60. Wang CC, McNamara AL, Shin J, et al. End-of-Range Radiobiological Effect on Rib Fractures in Patients Receiving Proton Therapy for Breast Cancer. *Int J Radiat Oncol Biol Phys*. 2020;107(3):449-454. doi:10.1016/j.ijrobp.2020.03.012
61. Guan F, Geng C, Ma D, et al. RBE Model-Based Biological Dose Optimization for Proton Radiobiology Studies. *Int J Part Ther*. 2018;5(1):160-171. doi:10.14338/IJPT-18-00007.1
62. Gu W, Ruan D, O'Connor D, et al. Robust optimization for intensity-modulated proton therapy with soft spot sensitivity regularization. *Med Phys*. 2019;46(3):1408-1425. doi:10.1002/mp.13344
63. Beck A, Teboulle M. A Fast Iterative Shrinkage-Thresholding Algorithm for Linear Inverse Problems. *SIAM J Imaging Sci*. 2009;2(1):183-202. doi:10.1137/080716542
64. Malitsky Y, Pock T. A first-order primal-dual algorithm with linesearch. *SIAM J Optim*. 2018;28(1):411-432. doi:10.1137/16M1092015

65. Landers A, O'Connor D, Ruan D, Sheng K. Automated 4π radiotherapy treatment planning with evolving knowledge-base. *Med Phys*. 2019;46(9):3833-3843. doi:10.1002/mp.13682
66. Nguyen D, O'Connor D, Ruan D, Sheng K. Deterministic direct aperture optimization using multiphase piecewise constant segmentation. *Med Phys*. 2017;44(11):5596-5609. doi:10.1002/mp.12529
67. Boyd S. Distributed Optimization and Statistical Learning via the Alternating Direction Method of Multipliers. *Found Trends® Mach Learn*. 2010;3(1):1-122. doi:10.1561/2200000016
68. O'Connor D, Voronenko Y, Nguyen D, Yin W, Sheng K. Fast non-coplanar beam orientation optimization based on group sparsity. *ArXiv171005308 Phys*. Published online October 15, 2017. Accessed August 11, 2021. http://arxiv.org/abs/1710.05308
69. Beck A, Teboulle M. A fast Iterative Shrinkage-Thresholding Algorithm with application to wavelet-based image deblurring. In: *2009 IEEE International Conference on Acoustics, Speech and Signal Processing*. ; 2009:693-696. doi:10.1109/ICASSP.2009.4959678
70. Chambolle A, Pock T. A First-Order Primal-Dual Algorithm for Convex Problems with Applications to Imaging. *J Math Imaging Vis*. 2011;40(1):120-145. doi:10.1007/s10851-010-0251-1
71. Hueso-González F, Wohlfahrt P, Craft D, Remillard K. An open-source platform for interactive collision prevention in photon and particle beam therapy treatment

planning. *Biomed Phys Eng Express*. 2020;6(5):055013. doi:10.1088/2057-1976/aba442

72. Huang S, Kang M, Souris K, et al. Validation and clinical implementation of an accurate Monte Carlo code for pencil beam scanning proton therapy. *J Appl Clin Med Phys*. 2018;19(5):558-572. doi:10.1002/acm2.12420
73. Grégoire V, Mackie TR. State of the art on dose prescription, reporting and recording in Intensity-Modulated Radiation Therapy (ICRU report No. 83). *Cancer Radiother J Soc Francaise Radiother Oncol*. 2011;15(6-7):555-559. doi:10.1016/j.canrad.2011.04.003
74. Trofimov A, Unkelbach J, DeLaney TF, Bortfeld T. Visualization of a variety of possible dosimetric outcomes in radiation therapy using dose-volume histogram bands. *Pract Radiat Oncol*. 2012;2(3):164-171. doi:10.1016/j.prro.2011.08.001
75. Ödén J, Eriksson K, Toma-Dasu I. Incorporation of relative biological effectiveness uncertainties into proton plan robustness evaluation. *Acta Oncol*. 2017;56(6):769-778. doi:10.1080/0284186X.2017.1290825
76. Bernal MA, Bordage MC, Brown JMC, et al. Track structure modeling in liquid water: A review of the Geant4-DNA very low energy extension of the Geant4 Monte Carlo simulation toolkit. *Phys Medica PM Int J Devoted Appl Phys Med Biol Off J Ital Assoc Biomed Phys AIFB*. 2015;31(8):861-874. doi:10.1016/j.ejmp.2015.10.087
77. Schuemann J, McNamara AL, Ramos-Méndez J, et al. TOPAS-nBio: An Extension to the TOPAS Simulation Toolkit for Cellular and Sub-cellular Radiobiology. *Radiat Res*. 2019;191(2):125-138. doi:10.1667/RR15226.1

78. Friedland W, Dingfelder M, Kundrát P, Jacob P. Track structures, DNA targets and radiation effects in the biophysical Monte Carlo simulation code PARTRAC. *Mutat Res*. 2011;711(1-2):28-40. doi:10.1016/j.mrfmmm.2011.01.003
79. Ma J, Wan Chan Tseung HS, Courneyea L, Beltran C, Herman MG, Remmes NB. Robust radiobiological optimization of ion beam therapy utilizing Monte Carlo and microdosimetric kinetic model. *Phys Med Biol*. 2020;65(15):155020. doi:10.1088/1361-6560/aba08b
80. Mairani A, Brons S, Cerutti F, et al. The FLUKA Monte Carlo code coupled with the local effect model for biological calculations in carbon ion therapy. *Phys Med Biol*. 2010;55(15):4273-4289. doi:10.1088/0031-9155/55/15/006
81. Qin N, Shen C, Tsai MY, et al. Full Monte Carlo-Based Biologic Treatment Plan Optimization System for Intensity Modulated Carbon Ion Therapy on Graphics Processing Unit. *Int J Radiat Oncol Biol Phys*. 2018;100(1):235-243. doi:10.1016/j.ijrobp.2017.09.002
82. Søvik Å, Ovrum J, Olsen DR, Malinen E. On the parameter describing the generalised equivalent uniform dose (gEUD) for tumours. *Phys Med*. 2007;23(3):100-106. doi:10.1016/j.ejmp.2007.09.001
83. Wang L, Fossati P, Paganetti H, et al. The Biological Basis for Enhanced Effects of Proton Radiation Therapy Relative to Photon Radiation Therapy for Head and Neck Squamous Cell Carcinoma. *Int J Part Ther*. 2021;8(1):3-13. doi:10.14338/IJPT-20-00070.1
84. Nill S, Bortfeld T, Oelfke U. Inverse planning of intensity modulated proton therapy. *Z Med Phys*. 2004;14(1):35-40. doi:10.1078/0939-3889-00198

85. Wilkens JJ, Oelfke U. Analytical linear energy transfer calculations for proton therapy. *Med Phys*. 2003;30(5):806-815. doi:10.1118/1.1567852

86. Cao W, Lim GJ, Li Y, Zhu XR, Zhang X. Improved Beam Angle Arrangement in Intensity Modulated Proton Therapy Treatment Planning for Localized Prostate Cancer. *Cancers*. 2015;7(2):574-584. doi:10.3390/cancers7020574

87. Taasti VT, Hong L, Shim JS, Deasy JO, Zarepisheh M. Automating proton treatment planning with beam angle selection using Bayesian optimization. *Med Phys*. 2020;47(8):3286-3296. doi:10.1002/mp.14215

88. An Y, Shan J, Patel SH, et al. Robust intensity-modulated proton therapy to reduce high linear energy transfer in organs at risk. *Med Phys*. 2017;44(12):6138-6147. doi:10.1002/mp.12610

89. Bai X, Lim G, Wieser HP, et al. Robust optimization to reduce the impact of biological effect variation from physical uncertainties in intensity-modulated proton therapy. *Phys Med Biol*. 2019;64(2):025004. doi:10.1088/1361-6560/aaf5e9

90. Giantsoudi D. Can robust optimization for range uncertainty in proton therapy act as a surrogate for biological optimization? *Int J Radiat Oncol Biol Phys*. 2017;99(2):S106-S107. doi:10.1016/j.ijrobp.2017.06.253

91. Zou J, Li H, Liu G. Split Bregman Algorithm for Structured Sparse Reconstruction. *IEEE Access*. 2018;6:21560-21569. doi:10.1109/ACCESS.2018.2825323

92. Xu Y, Huang TZ, Liu J, Lv XG. Split Bregman Iteration Algorithm for Image Deblurring Using Fourth-Order Total Bounded Variation Regularization Model. *J Appl Math*. 2013;2013:e238561. doi:10.1155/2013/238561

93. Stewart RD, Streitmatter SW, Argento DC, et al. Rapid MCNP simulation of DNA double strand break (DSB) relative biological effectiveness (RBE) for photons, neutrons, and light ions. *Phys Med Biol*. 2015;60(21):8249-8274. doi:10.1088/0031-9155/60/21/8249

94. Dahle TJ, Rusten E, Stokkevåg CH, et al. The FLUKA Monte Carlo code coupled with an OER model for biologically weighted dose calculations in proton therapy of hypoxic tumors. *Phys Medica PM Int J Devoted Appl Phys Med Biol Off J Ital Assoc Biomed Phys AIFB*. 2020;76:166-172. doi:10.1016/j.ejmp.2020.07.003

95. Henjum H, Dahle TJ, Mairani A, et al. Combined RBE and OER optimization in proton therapy with FLUKA based on EF5-PET. *J Appl Clin Med Phys*. Published online May 10, 2023:e14014. doi:10.1002/acm2.14014

96. Lai Y, Chi Y, Jia X. Mechanistic modelling of oxygen enhancement ratio of radiation via Monte Carlo simulation-based DNA damage calculation. *Phys Med Biol*. 2022;67(17). doi:10.1088/1361-6560/ac8853

97. Garrido-Hernandez G, Henjum H, Høiskar MK, Dahle TJ, Redalen KR, Ytre-Hauge KS. Hypoxia adapted relative biological effectiveness models for proton therapy: a simulation study. *Biomed Phys Eng Express*. 2022;8(6). doi:10.1088/2057-1976/ac9b5d

98. Brender JR, Saida Y, Devasahayam N, Krishna MC, Kishimoto S. Hypoxia Imaging As a Guide for Hypoxia-Modulated and Hypoxia-Activated Therapy. *Antioxid Redox Signal*. 2022;36(1-3):144-159. doi:10.1089/ars.2021.0176

99. Evans SM, Du KL, Chalian AA, et al. Patterns and levels of hypoxia in head and neck squamous cell carcinomas and their relationship to patient outcome. *Int J Radiat Oncol Biol Phys*. 2007;69(4):1024-1031. doi:10.1016/j.ijrobp.2007.04.067

100. Gaertner FC, Souvatzoglou M, Brix G, Beer AJ. Imaging of hypoxia using PET and MRI. *Curr Pharm Biotechnol*. 2012;13(4):552-570. doi:10.2174/138920112799436267

101. O'Connor JPB, Robinson SP, Waterton JC. Imaging tumour hypoxia with oxygen-enhanced MRI and BOLD MRI. *Br J Radiol*. 2019;92(1095):20180642. doi:10.1259/bjr.20180642

102. Wright P, Arnesen MR, Lønne PI, et al. Repeatability of hypoxia dose painting by numbers based on EF5-PET in head and neck cancer. *Acta Oncol Stockh Swed*. 2021;60(11):1386-1391. doi:10.1080/0284186X.2021.1944663

103. Silvoniemi A, Suilamo S, Laitinen T, et al. Repeatability of tumour hypoxia imaging using [18F]EF5 PET/CT in head and neck cancer. *Eur J Nucl Med Mol Imaging*. 2018;45(2):161-169. doi:10.1007/s00259-017-3857-3

104. Mapelli P, Picchio M. 18F-FAZA PET imaging in tumor hypoxia: A focus on high-grade glioma. *Int J Biol Markers*. 2020;35(1_suppl):42-46. doi:10.1177/1724600820905715

105. Shirvani SM, Huntzinger CJ, Melcher T, et al. Biology-guided radiotherapy: redefining the role of radiotherapy in metastatic cancer. *Br J Radiol*. 2021;94(1117):20200873. doi:10.1259/bjr.20200873

106. Rørvik E, Fjæra LF, Dahle TJ, et al. Exploration and application of phenomenological RBE models for proton therapy. *Phys Med Biol*. 2018;63(18):185013. doi:10.1088/1361-6560/aad9db

107. Zhang W, Li W, Lin Y, Wang F, Chen RC, Gao H. TVL1-IMPT: Optimization of Peak-to-Valley Dose Ratio Via Joint Total-Variation and L1 Dose Regularization for Spatially Fractionated Pencil-Beam-Scanning Proton Therapy. *Int J Radiat Oncol*. 2023;115(3):768-778. doi:10.1016/j.ijrobp.2022.09.064

108. Wilkens JJ, Oelfke U. Fast multifield optimization of the biological effect in ion therapy. *Phys Med Biol*. 2006;51(12):3127-3140. doi:10.1088/0031-9155/51/12/009

109. Rasey JS, Koh WJ, Evans ML, et al. Quantifying regional hypoxia in human tumors with positron emission tomography of [18F]fluoromisonidazole: a pretherapy study of 37 patients. *Int J Radiat Oncol Biol Phys*. 1996;36(2):417-428. doi:10.1016/s0360-3016(96)00325-2

110. Carreau A, Hafny-Rahbi BE, Matejuk A, Grillon C, Kieda C. Why is the partial oxygen pressure of human tissues a crucial parameter? Small molecules and hypoxia. *J Cell Mol Med*. 2011;15(6):1239-1253. doi:10.1111/j.1582-4934.2011.01258.x

111. Lazzeroni M, Toma-Dasu I, Ureba A, et al. Quantification of Tumor Oxygenation Based on FMISO PET: Influence of Location and Oxygen Level of the Well-Oxygenated Reference Region. In: Ryu PD, LaManna JC, Harrison DK, Lee SS, eds. *Oxygen Transport to Tissue XLI*. Advances in Experimental Medicine and Biology. Springer International Publishing; 2020:177-182. doi:10.1007/978-3-030-34461-0_22

112. Niyazi M, Andratschke N, Bendszus M, et al. ESTRO-EANO guideline on target delineation and radiotherapy details for glioblastoma. *Radiother Oncol*. 2023;184. doi:10.1016/j.radonc.2023.109663

113. Pang Y, Kosmin M, Li Z, et al. Isotoxic dose escalated radiotherapy for glioblastoma based on diffusion-weighted MRI and tumor control probability—an in-silico study. *Br J Radiol*. 2023;96(1146):20220384. doi:10.1259/bjr.20220384

114. Zindler JD, Schiffelers J, Lambin P, Hoffmann AL. Improved effectiveness of stereotactic radiosurgery in large brain metastases by individualized isotoxic dose prescription: an in silico study. *Strahlenther Onkol*. 2018;194(6):560-569. doi:10.1007/s00066-018-1262-x

115. Zindler JD, Thomas CR Jr, Hahn SM, Hoffmann AL, Troost EGC, Lambin P. Increasing the Therapeutic Ratio of Stereotactic Ablative Radiotherapy by Individualized Isotoxic Dose Prescription. *JNCI J Natl Cancer Inst*. 2016;108(2):djv305. doi:10.1093/jnci/djv305

116. Battestini M, Schwarz M, Krämer M, Scifoni E. Including Volume Effects in Biological Treatment Plan Optimization for Carbon Ion Therapy: Generalized Equivalent Uniform Dose-Based Objective in TRiP98. *Front Oncol*. 2022;12. Accessed November 27, 2023. https://www.frontiersin.org/articles/10.3389/fonc.2022.826414

117. Coleman CN. Hypoxic cell radiosensitizers: expectations and progress in drug development. *Int J Radiat Oncol Biol Phys*. 1985;11(2):323-329. doi:10.1016/0360-3016(85)90154-3

118. Overgaard J, Horsman MR. Modification of Hypoxia-Induced Radioresistance in Tumors by the Use of Oxygen and Sensitizers. *Semin Radiat Oncol*. 1996;6(1):10-21. doi:10.1053/SRAO0060010

119. Nordsmark M, Overgaard M, Overgaard J. Pretreatment oxygenation predicts radiation response in advanced squamous cell carcinoma of the head and neck.

Radiother Oncol J Eur Soc Ther Radiol Oncol. 1996;41(1):31-39. doi:10.1016/s0167-8140(96)91811-3

120. Sundfør K, Trope C, Suo Z, Bergsjø P. Normobaric oxygen treatment during radiotherapy for carcinoma of the uterine cervix. Results from a prospective controlled randomized trial. *Radiother Oncol J Eur Soc Ther Radiol Oncol*. 1999;50(2):157-165. doi:10.1016/s0167-8140(98)00142-x
121. Helbig L, Koi L, Brüchner K, et al. Hypoxia-inducible factor pathway inhibition resolves tumor hypoxia and improves local tumor control after single-dose irradiation. *Int J Radiat Oncol Biol Phys*. 2014;88(1):159-166. doi:10.1016/j.ijrobp.2013.09.047
122. Chvetsov AV, Hanin LG, Stewart RD, Zeng J, Rengan R, Lo SS. Tumor control probability in hypofractionated radiotherapy as a function of total and hypoxic tumor volumes. *Phys Med Biol*. 2021;66(12). doi:10.1088/1361-6560/ac047e
123. Chao KS, Bosch WR, Mutic S, et al. A novel approach to overcome hypoxic tumor resistance: Cu-ATSM-guided intensity-modulated radiation therapy. *Int J Radiat Oncol Biol Phys*. 2001;49(4):1171-1182. doi:10.1016/s0360-3016(00)01433-4
124. Beck R, Röper B, Carlsen JM, et al. Pretreatment 18F-FAZA PET Predicts Success of Hypoxia-Directed Radiochemotherapy Using Tirapazamine. *J Nucl Med*. 2007;48(6):973-980. doi:10.2967/jnumed.106.038570
125. Grimes DR, Warren DR, Warren S. Hypoxia imaging and radiotherapy: bridging the resolution gap. *Br J Radiol*. 90(1076):20160939. doi:10.1259/bjr.20160939

126. Hirata K, Yamaguchi S, Shiga T, Kuge Y, Tamaki N. The Roles of Hypoxia Imaging Using 18F-Fluoromisonidazole Positron Emission Tomography in Glioma Treatment. *J Clin Med*. 2019;8(8):1088. doi:10.3390/jcm8081088

127. Busk M, Overgaard J, Horsman MR. Imaging of Tumor Hypoxia for Radiotherapy: Current Status and Future Directions. *Semin Nucl Med*. 2020;50(6):562-583. doi:10.1053/j.semnuclmed.2020.05.003

128. Toffoli S, Michiels C. Intermittent hypoxia is a key regulator of cancer cell and endothelial cell interplay in tumours. *FEBS J*. 2008;275(12):2991-3002. doi:10.1111/j.1742-4658.2008.06454.x

129. Nehmeh SA, Lee NY, Schröder H, et al. Reproducibility of intratumor distribution of (18)F-fluoromisonidazole in head and neck cancer. *Int J Radiat Oncol Biol Phys*. 2008;70(1):235-242. doi:10.1016/j.ijrobp.2007.08.036

130. Vu C, Chai Y, Coloigner J, et al. Quantitative perfusion mapping with induced transient hypoxia using BOLD MRI. *Magn Reson Med*. 2021;85(1):168-181. doi:10.1002/mrm.28422

131. Hughes JR, Parsons JL. FLASH Radiotherapy: Current Knowledge and Future Insights Using Proton-Beam Therapy. *Int J Mol Sci*. 2020;21(18):6492. doi:10.3390/ijms21186492

132. Maxim PG, Tantawi SG, Loo BW. PHASER: A platform for clinical translation of FLASH cancer radiotherapy. *Radiother Oncol J Eur Soc Ther Radiol Oncol*. 2019;139:28-33. doi:10.1016/j.radonc.2019.05.005

133. Lyu Q, Neph R, O'Connor D, Ruan D, Boucher S, Sheng K. ROAD: ROtational direct Aperture optimization with a Decoupled ring-collimator for FLASH radiotherapy. *Phys Med Biol*. 2021;66(3):035020. doi:10.1088/1361-6560/abcbd0

134. Nesteruk KP, Togno M, Grossmann M, et al. Commissioning of a clinical pencil beam scanning proton therapy unit for ultra-high dose rates (FLASH). *Med Phys*. 2021;48(7):4017-4026. doi:10.1002/mp.14933

135. Farr J, Grilj V, Malka V, Sudharsan S, Schippers M. Ultra-high dose rate radiation production and delivery systems intended for FLASH. *Med Phys*. 2022;49(7):4875-4911. doi:10.1002/mp.15659

136. Schwarz M, Traneus E, Safai S, Kolano A, van de Water S. Treatment planning for Flash radiotherapy: General aspects and applications to proton beams. *Med Phys*. 2022;49(4):2861-2874. doi:10.1002/mp.15579

137. Esplen N, Mendonca MS, Bazalova-Carter M. Physics and biology of ultrahigh dose-rate (FLASH) radiotherapy: a topical review. *Phys Med Biol*. 2020;65(23):23TR03. doi:10.1088/1361-6560/abaa28

138. Nahum AE. The radiobiology of hypofractionation. *Clin Oncol R Coll Radiol G B*. 2015;27(5):260-269. doi:10.1016/j.clon.2015.02.001

139. Buonanno M, Grilj V, Brenner DJ. Biological Effects in Normal Cells Exposed to FLASH Dose Rate Protons. *Radiother Oncol J Eur Soc Ther Radiol Oncol*. 2019;139:51-55. doi:10.1016/j.radonc.2019.02.009

140. Gao H, Lin B, Lin Y, et al. Simultaneous dose and dose rate optimization (SDDRO) for FLASH proton therapy. *Med Phys*. 2020;47(12):6388-6395. doi:10.1002/mp.14531

141. Montay-Gruel P, Acharya MM, Gonçalves Jorge P, et al. Hypofractionated FLASH-RT as an Effective Treatment against Glioblastoma that Reduces Neurocognitive Side Effects in Mice. *Clin Cancer Res Off J Am Assoc Cancer Res*. 2021;27(3):775-784. doi:10.1158/1078-0432.CCR-20-0894

142. MacKay R, Burnet N, Lowe M, et al. FLASH radiotherapy: Considerations for multibeam and hypofractionation dose delivery. *Radiother Oncol J Eur Soc Ther Radiol Oncol*. 2021;164:122-127. doi:10.1016/j.radonc.2021.09.011

143. van Marlen P, Verbakel WFAR, Slotman BJ, Dahele M. Single-fraction 34 Gy Lung Stereotactic Body Radiation Therapy Using Proton Transmission Beams: FLASH-dose Calculations and the Influence of Different Dose-rate Methods and Dose/Dose-rate Thresholds. *Adv Radiat Oncol*. 2022;7(4):100954. doi:10.1016/j.adro.2022.100954

144. Diffenderfer ES, Sørensen BS, Mazal A, Carlson DJ. The current status of preclinical proton FLASH radiation and future directions. *Med Phys*. 2022;49(3):2039-2054. doi:10.1002/mp.15276

145. Wei S, Lin H, Choi JI, et al. FLASH Radiotherapy Using Single-Energy Proton PBS Transmission Beams for Hypofractionation Liver Cancer: Dose and Dose Rate Quantification. *Front Oncol*. 2021;11:813063. doi:10.3389/fonc.2021.813063

146. van Marlen P, Dahele M, Folkerts M, Abel E, Slotman BJ, Verbakel WFAR. Bringing FLASH to the Clinic: Treatment Planning Considerations for Ultrahigh Dose-Rate Proton Beams. *Int J Radiat Oncol Biol Phys*. 2020;106(3):621-629. doi:10.1016/j.ijrobp.2019.11.011

147. Poulsen P, Kanouta E, Sitarz M, et al. MO-0720 Proton FLASH: Impact of dose rate on biological response in an acute damage mouse model. *Radiother Oncol*. 2023;182:S589-S590. doi:10.1016/S0167-8140(23)08445-1

148. Kang M, Wei S, Choi JI, Lin H, Simone CB. A Universal Range Shifter and Range Compensator Can Enable Proton Pencil Beam Scanning Single-Energy Bragg Peak FLASH-RT Treatment Using Current Commercially Available Proton Systems. *Int J Radiat Oncol Biol Phys*. 2022;113(1):203-213. doi:10.1016/j.ijrobp.2022.01.009

149. Lin Y, Lin B, Fu S, et al. SDDRO-joint: simultaneous dose and dose rate optimization with the joint use of transmission beams and Bragg peaks for FLASH proton therapy. *Phys Med Biol*. 2021;66(12). doi:10.1088/1361-6560/ac02d8

150. Wei S, Lin H, Choi JI, Simone CB, Kang M. A Novel Proton Pencil Beam Scanning FLASH RT Delivery Method Enables Optimal OAR Sparing and Ultra-High Dose Rate Delivery: A Comprehensive Dosimetry Study for Lung Tumors. *Cancers*. 2021;13(22):5790. doi:10.3390/cancers13225790

151. van de Water S, Safai S, Schippers JM, Weber DC, Lomax AJ. Towards FLASH proton therapy: the impact of treatment planning and machine characteristics on achievable dose rates. *Acta Oncol Stockh Swed*. 2019;58(10):1463-1469. doi:10.1080/0284186X.2019.1627416

152. Folkerts MM, Abel E, Busold S, Perez JR, Krishnamurthi V, Ling CC. A framework for defining FLASH dose rate for pencil beam scanning. *Med Phys*. 2020;47(12):6396-6404. doi:10.1002/mp.14456

153. Durante M, Bräuer-Krisch E, Hill M. Faster and safer? FLASH ultra-high dose rate in radiotherapy. *Br J Radiol*. 2018;91(1082):20170628. doi:10.1259/bjr.20170628

154. Spitz DR, Buettner GR, Petronek MS, et al. An integrated physico-chemical approach for explaining the differential impact of FLASH versus conventional dose rate irradiation on cancer and normal tissue responses. *Radiother Oncol J Eur Soc Ther Radiol Oncol*. 2019;139:23-27. doi:10.1016/j.radonc.2019.03.028

155. Moreno AC, Frank SJ, Garden AS, et al. Intensity modulated proton therapy (IMPT) - The future of IMRT for head and neck cancer. *Oral Oncol*. 2019;88:66-74. doi:10.1016/j.oraloncology.2018.11.015

156. Giovannelli AC, Maradia V, Meer D, et al. Beam properties within the momentum acceptance of a clinical gantry beamline for proton therapy. *Med Phys*. 2022;49(3):1417-1431. doi:10.1002/mp.15449

157. Jansen J, Knoll J, Beyreuther E, et al. Does FLASH deplete oxygen? Experimental evaluation for photons, protons, and carbon ions. *Med Phys*. 2021;48(7):3982-3990. doi:10.1002/mp.14917

158. Jolly S, Owen H, Schippers M, Welsch C. Technical challenges for FLASH proton therapy. *Phys Medica PM Int J Devoted Appl Phys Med Biol Off J Ital Assoc Biomed Phys AIFB*. 2020;78:71-82. doi:10.1016/j.ejmp.2020.08.005

159. Gu W, Ruan D, Lyu Q, Zou W, Dong L, Sheng K. A novel energy layer optimization framework for spot-scanning proton arc therapy. *Med Phys*. 2020;47(5):2072-2084. doi:10.1002/mp.14083

160. Deffet S, Hamaide V, Sterpin E. Definition of dose rate for FLASH pencil-beam scanning proton therapy: A comparative study. *Med Phys*. 2023;50(9):5784-5792. doi:10.1002/mp.16607

161. Ma C, Zhou J, Chang CW, et al. Streamlined pin-ridge-filter design for single-energy proton FLASH planning. *Med Phys*. Published online January 12, 2024. doi:10.1002/mp.16939

162. Habraken S, Breedveld S, Groen J, Nuyttens J, Hoogeman M. Trade-off in healthy tissue sparing of FLASH and fractionation in stereotactic proton therapy of lung lesions with transmission beams. *Radiother Oncol J Eur Soc Ther Radiol Oncol*. 2022;175:231-237. doi:10.1016/j.radonc.2022.08.015

163. Ding X, Li X, Zhang JM, Kabolizadeh P, Stevens C, Yan D. Spot-Scanning Proton Arc (SPArc) Therapy: The First Robust and Delivery-Efficient Spot-Scanning Proton Arc Therapy. *Int J Radiat Oncol Biol Phys*. 2016;96(5):1107-1116. doi:10.1016/j.ijrobp.2016.08.049

164. Zhang G, Long Y, Lin Y, Chen RC, Gao H. A treatment plan optimization method with direct minimization of number of energy jumps for proton arc therapy. *Phys Med Biol*. 2023;68(8). doi:10.1088/1361-6560/acc4a7

165. Deasy JO, Moiseenko V, Marks L, Chao KSC, Nam J, Eilsbruch A. Radiotherapy Dose-Volume Effects on Salivary Gland Function. *Int J Radiat Oncol Biol Phys*. 2010;76(3 0):S58-S63. doi:10.1016/j.ijrobp.2009.06.090

166. Anderson NJ, Wada M, Schneider-Kolsky M, Rolfo M, Joon DL, Khoo V. Dose-volume response in acute dysphagia toxicity: Validating QUANTEC recommendations into clinical practice for head and neck radiotherapy. *Acta Oncol*. 2014;53(10):1305-1311. doi:10.3109/0284186X.2014.933874

167. Mazzola R, Ricchetti F, Fiorentino A, et al. Dose–volume-related dysphagia after constrictor muscles definition in head and neck cancer intensity-modulated radiation treatment. *Br J Radiol*. 2014;87(1044):20140543. doi:10.1259/bjr.20140543

168. Li G, Li Y, Wang J, et al. Guidelines for radiotherapy of prostate cancer (2020 edition). *Precis Radiat Oncol*. 2021;5(3):160-182. doi:10.1002/pro6.1129

169. Rhee DJ, Beddar S, Jaoude JA, et al. Dose Escalation for Pancreas SBRT: Potential and Limitations of using Daily Online Adaptive Radiation Therapy and an Iterative Isotoxicity Automated Planning Approach. *Adv Radiat Oncol*. 2023;8(4). doi:10.1016/j.adro.2022.101164

170. Friedl AA, Prise KM, Butterworth KT, Montay-Gruel P, Favaudon V. Radiobiology of the FLASH effect. *Med Phys*. 2022;49(3):1993-2013. doi:10.1002/mp.15184

171. Adrian G, Konradsson E, Beyer S, et al. Cancer Cells Can Exhibit a Sparing FLASH Effect at Low Doses Under Normoxic In Vitro-Conditions. *Front Oncol*. 2021;11:686142. doi:10.3389/fonc.2021.686142

172. Verhaegen F, Wanders RG, Wolfs C, Eekers D. Considerations for shoot-through FLASH proton therapy. *Phys Med Biol*. 2021;66(6):06NT01. doi:10.1088/1361-6560/abe55a

173. Hyer DE, Bennett LC, Geoghegan TJ, Bues M, Smith BR. Innovations and the Use of Collimators in the Delivery of Pencil Beam Scanning Proton Therapy. *Int J Part Ther*. 2021;8(1):73-83. doi:10.14338/IJPT-20-00039.1

174. van de Water S, Belosi MF, Albertini F, Winterhalter C, Weber DC, Lomax AJ. Shortening delivery times for intensity-modulated proton therapy by reducing the

number of proton spots: an experimental verification. *Phys Med Biol*. 2020;65(9):095008. doi:10.1088/1361-6560/ab7e7c

175. Tsujii H, Kamada T. A review of update clinical results of carbon ion radiotherapy. *Jpn J Clin Oncol*. 2012;42(8):670-685. doi:10.1093/jjco/hys104

176. Ohno T. Particle radiotherapy with carbon ion beams. *EPMA J*. 2013;4(1):9. doi:10.1186/1878-5085-4-9

177. Ogata T, Teshima T, Kagawa K, et al. Particle irradiation suppresses metastatic potential of cancer cells. *Cancer Res*. 2005;65(1):113-120.

178. Takahashi Y, Teshima T, Kawaguchi N, et al. Heavy ion irradiation inhibits in vitro angiogenesis even at sublethal dose. *Cancer Res*. 2003;63(14):4253-4257.

179. Haberer T h, Debus J, Eickhoff H, Jäkel O, Schulz-Ertner D, Weber U. The Heidelberg Ion Therapy Center. *Radiother Oncol J Eur Soc Ther Radiol Oncol*. 2004;73 Suppl 2:S186-190. doi:10.1016/s0167-8140(04)80046-x

180. Durante M, Flanz J. Charged particle beams to cure cancer: Strengths and challenges. *Semin Oncol*. 2019;46(3):219-225. doi:10.1053/j.seminoncol.2019.07.007

181. Kamada T. Overview of the Heavy-Ion Medical Accelerator in Chiba (HIMAC) Practices. In: Tsujii H, Kamada T, Shirai T, Noda K, Tsuji H, Karasawa K, eds. *Carbon-Ion Radiotherapy: Principles, Practices, and Treatment Planning*. Springer Japan; 2014:17-22. doi:10.1007/978-4-431-54457-9_3

182. Bhattacharyya T, Koto M, Ikawa H, et al. First prospective feasibility study of carbon-ion radiotherapy using compact superconducting rotating gantry. *Br J Radiol*. 2019;92(1103):20190370. doi:10.1259/bjr.20190370

183. Sheng Y, Sun J, Wang W, et al. Performance of a 6D Treatment Chair for Patient Positioning in an Upright Posture for Fixed Ion Beam Lines. *Front Oncol*. 2020;10:122. doi:10.3389/fonc.2020.00122

184. Kosaki K, Ecker S, Habermehl D, et al. Comparison of intensity modulated radiotherapy (IMRT) with intensity modulated particle therapy (IMPT) using fixed beams or an ion gantry for the treatment of patients with skull base meningiomas. *Radiat Oncol Lond Engl*. 2012;7:44. doi:10.1186/1748-717X-7-44

185. Koom WS, Mori S, Furuich W, Yamada S. Beam direction arrangement using a superconducting rotating gantry in carbon ion treatment for pancreatic cancer. *Br J Radiol*. 2019;92(1098):20190101. doi:10.1259/bjr.20190101

186. Zhang X, Hsi WC, Yang F, et al. Development of an isocentric rotating chair positioner to treat patients of head and neck cancer at upright seated position with multiple nonplanar fields in a fixed carbon-ion beamline. *Med Phys*. 2020;47(6):2450-2460. doi:10.1002/mp.14115

187. Krämer M, Scholz M. Rapid calculation of biological effects in ion radiotherapy. *Phys Med Biol*. 2006;51(8):1959-1970. doi:10.1088/0031-9155/51/8/001

188. Prior P, Chen X, Hall W, Erickson B, Li A. Estimation of the Alpha-beta Ratio for Chemoradiation of Locally Advanced Pancreatic Cancer. In: Vol 102. ; 2018:S97. doi:10.1016/j.ijrobp.2018.06.250

189. Kehwar TS. Analytical approach to estimate normal tissue complication probability using best fit of normal tissue tolerance doses into the NTCP equation of the linear quadratic model. *J Cancer Res Ther*. 2005;1(3):168-179. doi:10.4103/0973-1482.19597

190. Kawashiro S, Yamada S, Okamoto M, et al. Multi-institutional Study of Carbon-ion Radiotherapy for Locally Advanced Pancreatic Cancer: Japan Carbon-ion Radiation Oncology Study Group (J-CROS) Study 1403 Pancreas. *Int J Radiat Oncol Biol Phys*. 2018;101(5):1212-1221. doi:10.1016/j.ijrobp.2018.04.057

191. Jung H, Kum O, Han Y, Park HC, Kim JS, Choi DH. A virtual simulator designed for collision prevention in proton therapy. *Med Phys*. 2015;42(10):6021-6027. doi:10.1118/1.4931411

192. Kumagai M, Mori S, Yamamoto N. Impact of treatment planning with deformable image registration on dose distribution for carbon-ion beam lung treatment using a fixed irradiation port and rotating couch. *Br J Radiol*. 2015;88(1050):20140734. doi:10.1259/bjr.20140734

193. Chan MF, Lim SB, Li X, Tang X, Zhang P, Shi C. Commissioning and Evaluation of a Third-Party 6 Degrees-of-Freedom Couch Used in Radiotherapy. *Technol Cancer Res Treat*. 2019;18:1533033819870778. doi:10.1177/1533033819870778

194. Kamp F, Cabal G, Mairani A, Parodi K, Wilkens JJ, Carlson DJ. Fast Biological Modeling for Voxel-based Heavy Ion Treatment Planning Using the Mechanistic Repair-Misrepair-Fixation Model and Nuclear Fragment Spectra. *Int J Radiat Oncol Biol Phys*. 2015;93(3):557-568. doi:10.1016/j.ijrobp.2015.07.2264

195. Grimes DR, Warren DR, Partridge M. An approximate analytical solution of the Bethe equation for charged particles in the radiotherapeutic energy range. *Sci Rep*. 2017;7(1):9781. doi:10.1038/s41598-017-10554-0

196. Qin N, Pinto M, Tian Z, et al. Initial development of goCMC: a GPU-oriented fast cross-platform Monte Carlo engine for carbon ion therapy. *Phys Med Biol*. 2017;62(9):3682-3699. doi:10.1088/1361-6560/aa5d43

197. Grevillot L, Boersma DJ, Fuchs H, et al. Technical Note: GATE-RTion: a GATE/Geant4 release for clinical applications in scanned ion beam therapy. *Med Phys*. 2020;47(8):3675-3681. doi:10.1002/mp.14242

198. Wang W, Huang Z, Sheng Y, et al. RBE-weighted dose conversions for carbon ionradiotherapy between microdosimetric kinetic model and local effect model for the targets and organs at risk in prostate carcinoma. *Radiother Oncol J Eur Soc Ther Radiol Oncol*. 2020;144:30-36. doi:10.1016/j.radonc.2019.10.005

199. O'Connor D, Yu V, Nguyen D, Ruan D, Sheng K. Fraction-variant beam orientation optimization for non-coplanar IMRT. *Phys Med Biol*. 2018;63(4):045015. doi:10.1088/1361-6560/aaa94f